Doctoral Thesis

Investigation of Atomic-Scale Defects in Two-Dimensional Materials

Gyeong Hee Ryu

Department of Materials Science and Engineering

Graduate School of UNIST

2018

Investigation of Atomic-Scale Defects in Two-Dimensional Materials

Gyeong Hee Ryu

Department of Materials Science and Engineering

Graduate School of UNIST

Investigation of Atomic-Scale Defects in Two-Dimensional Materials

A thesis/dissertation
submitted to the Graduate School of UNIST
in partial fulfillment of the
requirements for the degree of
Doctor of Philosophy

Gyeong Hee Ryu

12.11.2017
Approved by

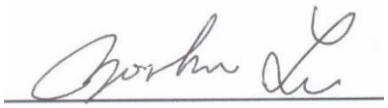

Advisor
Zonghoon Lee

Investigation of Atomic-Scale Defects in Two-Dimensional Materials

Gyeong Hee Ryu

This certifies that the thesis/dissertation of Gyeong Hee Ryu is approved.

12.11.2017

signature

Advisor: Zonghoon Lee

signature

Soon-Yong Kwon

signature

Hyung-Joon Shin

signature

Hyeon Suk Shin

signature

Gun-Do Lee

This dissertation is dedicated to my lovely husband, family and ASEMers.

Abstract

Defects are a very important aspect of materials science as they can influence the intrinsic properties of materials. In particular, structural defects can greatly impact two-dimensional (2D) materials because these defects are all located on the surface. To understand the relationship between defects and properties of 2D materials, the basic crystal structure of the materials and the formation mechanism of their defects must be precisely understood.

Graphene, which consists of single carbon atoms, has been comprehensively studied in regards to its structural defects, owing to its many interesting mechanical and chemical properties. Nevertheless, the behavior of graphene defects is not well understood at the atomic scale. Hexagonal boron nitride (hBN) has a hexagonal lattice similar to that of graphene, but consists of two elements (boron and nitrogen) instead of one. Molybdenum disulfide (MoS_2) is a representative transition metal chalcogenide (TMD), which consists of two sulfur layers and a molybdenum layer. The defects of hBN and MoS_2 have also been studied, but these studies are not well-developed compared to those of graphene, as hBN and MoS_2 have more complex structures.

As theoretical studies of defects in three-dimensional (3D) materials are already well-established, the study of defects in 2D materials must also be developed as the two are not entirely relatable. In this thesis, the atomic structures and dynamics of defects on 2D materials are systemically studied using aberration-corrected transmission electron microscopy. To investigate the underlying mechanism of these defects, an accelerating voltage of 80 kV was used, selected in consideration of the knock-on thresholds of graphene, hBN and MoS_2 when forming and analyzing atomic defects under electron beam irradiation. The effects of oxygen and oxygen atoms on defects in monolayer graphene sheet were also studied using density functional theory calculations and free standing 2D silicon dioxide sheets. Finally, the dynamics of atomic defects such as dopants, vacancies, edge states, and stacking in 2D materials were investigated, showing excellent visualization of atomic defect structures.

Contents

List of Figures

List of Table

Chapter 1: Introduction

C–O bonds[1-10] have numerous applications in electronics, sensors, and catalytic reactions. Among the many known oxidation treatment methods, ultraviolet–ozone (UV/Ozone) and oxygen plasma treatments have several advantages: neither treatment uses severe chemicals, and both treatments can oxidize materials at specific sites through sacrificial-layer masking.[11] UVO treatment removes organic molecules from a material's surface and can also be used for surface modification.[12-14] In this process, ozone, which absorbs UV rays at a wavelength of 184.9 nm, is generated from oxygen in the atmosphere. The ozone decomposes into oxygen and active oxygen to absorb UV rays with a wavelength of 253.7 nm. The active oxygen is highly unstable and induces the oxidative decomposition of organic molecules, water, and carbon dioxide. However, plasma treatment can impact a surface with enough energy to break the molecular bonds on most material surfaces. This bond breakage creates very reactive free radicals on the surface, which can react rapidly to form various chemical functional groups in the presence of oxygen.[15-21] Even small amounts of reactive chemical functional groups incorporated into materials can dramatically improve their surface functionality. Therefore, both of these dry oxidation treatments[11] are comprehensively used to treat various materials, such as on graphene where their effects are similar to surface oxidation. Defects formed by dry oxidation treatments result from the attachment of chemical functional groups and the removal of carbon atoms from their original sites to accommodate the functional groups; the resultant defect structures are commonly characterized by Raman spectroscopy[12-13, 19-20], X-ray photoelectron spectroscopy (XPS)[17-18, 22-25] and electron energy loss spectroscopy (EELS)[26-31]. However, the UV/Ozone and plasma treatments are fundamentally different processes. The UV/Ozone treatment process is based on a chemical reaction, whereas the oxygen plasma treatment process involves both a physical and a chemical reaction. Consequently, the resultant defects formed via partial surface oxidations by UV/Ozone and oxygen plasma treatments differ based on the method used.

Interest in point defects in monolayer graphene has emerged on many research fronts.[32] Except for the case of native defect investigations, defect studies were first motivated by a desire to understand the aspects of radiation damage occurring on graphene sheets.[33-34] The characterization of point defects is also an important research topic because graphene has a variety of such defects, e.g., dopants, monovacancies, and multivacancies.[4-5, 35-42] Furthermore, the emergence of these defects reflects many useful behaviors of carbon atoms in graphene sheets, including defect structures and energetics.[43] Vacancies[32, 36, 44-50] are formed as a result of knock-on carbon atom displacements, which are explained using various calculations and experimental results.[37-38, 42, 51-53] The study of vacancies is an essential and fundamental contribution to understanding both basic and complicated defect processes in graphene sheets. Oxidized graphene surfaces have been extensively studied and more recently have been the subject of considerable interest because of their implications in the surface chemistry of graphene.[21, 54-

[63] Both graphene oxide (GO) and reduced GO have large quantities of oxygen-containing functional groups. However, specific observation of these is limited in transmission electron microscopy (TEM) because there are few defect-free regions for analyzing the behavior of these groups. Although point defects originating from oxygen-containing functional groups in graphene sheets have been studied using calculation-focused research, the specific atomic behaviors of these oxygen and carbon atoms have not been investigated under electron beam irradiation.

Defects are known to influence the intrinsic electronic and mechanical properties of materials. In graphene, vacancies, dislocations, grain boundaries and other topological defects have been shown to alter the chemical and physical properties of graphene, and as such they have been extensively investigated.[41, 64] The defect structures in hBN are even more varied and complex because, unlike graphene,[65-66] its hexagonal 2D lattice consists of two elements, boron and nitrogen. At present, it is well-known that the edges of holes in hBN sheets commonly adopt a zigzag type under electron beam irradiation.[67-68] Moreover, the zigzag configuration contains two different types of terminated edges due to the heterogeneity of hBN, factors that have been shown to affect the material's intrinsic electrical properties.[69] The growth mechanisms of holes formed in hBN are also not well established.

MoS_2, a two-dimensional (2D) transition metal dichalcogenide (TMD), has received a great deal of attention since its isolation as atomically thin layers from bulk 2D materials and films synthesized by deposition.[70-75] Since MoS_2 is tri-layered with a Mo atom bonded to six S atoms in layers above and belos, MoS_2 shows unique line defects under electron beam irradiation. While other 2D materials such as graphene and hBN[65-66, 76-78] are composed of single layer hexagonal 2D lattice, these generally have defects such as vacancies and holes, but not line defects.[79] When an electron beam irradiates the MoS_2 sheet, S vacancies are firstly formed depending on the knock-on threshold of S atoms. After that, S vacancies increase the vacancy concentration[80], and then line defects appear instead of forming holes through prolonged exposure to the electron beam.[79] If holes are formed in the monolayer MoS_2 sheet, Mo atoms are aggregated around the edges of holes, while S atoms are easily knocked out due to the higher displacement threshold of Mo compared to S.[80-81]

Thus, I will discuss the effects of these two dry oxidation treatments on monolayer graphene sheets using atomic-resolution imaging and electron energy loss spectroscopy (EELS) in TEM. These two treatments induce the attachment of oxygen atoms onto the graphene surface, but only the oxygen plasma treatment consistently forms topological defects. Moreover, the defects generated by oxygen plasma treatment more effectively oxidize the graphene surface than those generated by UVO treatment. The formation of the defects induced by these two dry oxidation treatments are studied comparatively using real atomic images. In addition, I will directly observe OH molecules driven in the formation of point defects in monolayer graphene sheets from monovacancies to divacancies. The point defects are the major outcome of combining UVO treatment and electron beam irradiation. Each point defect has different intermediate states. In particular, if OH molecules on the pristine graphene sheet are

dissociated to oxygen and hydrogen atoms and the hydrogen atoms are subsequently incorporated into the graphene lattice, new configurations of paired 13-5 rings will appear. I explain the dynamics of oxygen and hydrogen atoms on graphene surface to form point defects using atomic resolution TEM (ARTEM) imaging together with density functional theory (DFT) to interpret the atomic structure and intermediate states of the formed point defects. I will also study the growth of triangular holes in monolayer hBN sheets from the nucleation of a B vacancy to areas over exceed 50 nm^2 in size using ARTEM. As part of these studies, the growth dynamics of single triangular holes as well as the processes by which they merge with other holes were explored. The experimental observations were then compared with DFT calculations and molecular dynamics (MD) simulations, which provided additional insight into the mechanisms of hole growth. Lastly, I will study the hole formation mediated by line defects in monolayer MoS_2 sheet using ARTEM. The defect formation with Mo clustering is investigated under electron beam irradiation. The dynamic ARTEM observations revealed a process of transformation from binary 2D MoS_2 to a metallic 2D material of Mo around holes of MoS_2.

Chapter 2. Research Background

2.1. Advanced Transmission Electron Microscopy

2.1.1. Aberration corrected transmission electron microscopy

Observing the atomic structure of materials is a long-standing dream that has now become a burning issue with the advent of nanoscience and nanotechnology, for which atomic-scale synthesis requires atomic-resolution characterization of the results.[82-83] In recent decades, substantial progress has been made in electron microscopy (EM) to achieve this objective, and in a limited number of favorable cases, it has been possible to perform structure investigations at atomic-scale resolutions.[84] However, only the successful construction of aberration-corrected electron lenses in the 1990s[85-86] set ARTEM on its path to becoming a more generally applied technique in advanced condensed-matter physics and materials science.[87-89] Beyond the high-precision mapping of atomic positions, aberration-corrected TEM (ACTEM) enables the occupancies of atom sites to be determined and allows atomic scale imaging of chemical composition and bonding by combining high resolution in energy and space with the use of spatially-resolved EELS to map electron states localized at or between atoms.

In principle, two types of aberrations are always involved: geometrical aberrations, such as spherical aberrations, and chromatic aberrations, which arise from the electron-energy dependence of the refraction properties of magnetic fields. Current lens designs can only correct for the former. An ideal converging lens would image a point in the object to a corresponding point in the image. Because of aberrations, the image is broadened into a point-spread disk. This is illustrated schematically in Figure 1a for the case of a spherical aberration. The point spread arises from the refraction power of a real lens increasing with the angle that the beams entering the lens make with its optical axis. As a result, the electrons that scatter in the specimen at high angles come into a focus some distance in front of the Gaussian image plane that is defined by the low-angle beams. The focal length of an electromagnetic lens can be easily varied by adjusting the current through the lens coils. Such defocusing also induces point spread and is treated as an aberration. Although these two represent the most substantial aberrations, there are many more that contribute not only to a broadening but also to an angular distortion of the point-spread disk.[88, 90-91] In particular, the spherical aberration of a converging lens is corrected by adding a diverging lens that compensates for the too-high refraction power of high angle scattered beams (Figure. 1b). This is achieved by a double-hexapole system[92-93] in conventional TEM and in scanning TEM (STEM).

Many advances in the field of EM have enabled atomic scale imaging about structure and defects in low dimensional materials. The aberration-correction electro-optic hardware can significantly reduce the influence of the inherent spherical aberration of the electron lens, and a chromatic aberration corrector or monochromator can minimize the energy spreading the electron beam illumination for the

sub Angstrom imaging.[94] The most important factor is the development of imaging with low acceleration voltages (60 and 80 kV, which significantly minimizes the damaging effect of the illumination electrons on the specimen.[64, 95] Furthermore, the electron-ion scattering cross sectional area increases as the voltage decreases and produces more contrast for a given dose. Finally, the electronic scintillator camera has a lower point spread function at a lower operating voltage, resulting in a sharper image.

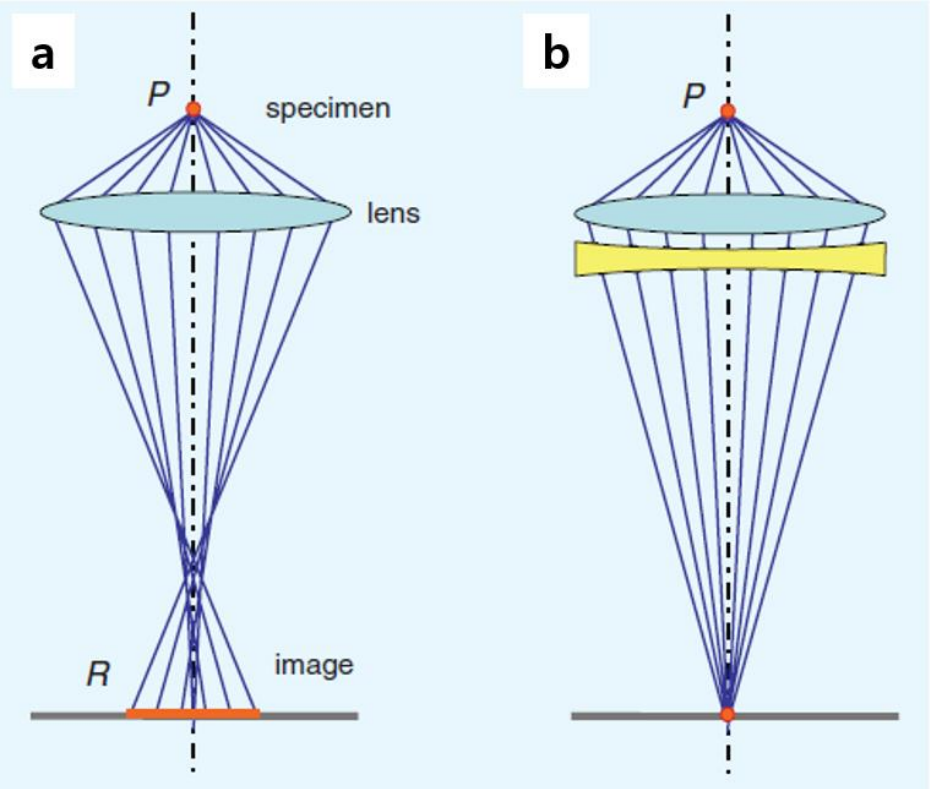

Figure 1. (a) Schematic illustration of the spherical aberration of a converging lens. (B) Spherical aberration is compensated by combining the converging lens with a suitable diverging lens.[83]

2.1.2. Theory of high resolution imaging

In EM, electrons are focused using highly-concentrated magnetic fields formed between soft-iron pole pieces and generated by currents flowing through annular coils. In a basic TEM imaging array, the electron beam from the electron gun typically illuminates the specimen through the lens's illumination system. Radiation interacts with the sample and is scattered. The scattered radiation is focused by the objective lens, and the additional magnifier produces a convenient sized image. There are two important factors that determine the essential geometry of an imaging system. First, the wavelength of the electrons determines the range of scattering angles from the specimen. Second, the aberrations of the electron lens limit the angular range of scattered radiation that can make useful contributions to the image. Relative to other radiation of comparable wavelength or energy, electrons interact very strongly with matter.

Elastic scattering is of prime importance for high-resolution imaging[96]. To avoid serious complications, one must use a specimen thickness of the same order of magnitude as the mean free path for elastic scattering. For electrons, the scattering angles are small, so in traversing a thin specimen, the electron wave does not suffer a sideways displacement dependent on the potential distribution along a straight-line path through the object. Thus, if the potential distribution in the object is represented by a function (xyz), a plane wave transmitted through the object in the z-direction suffers a phase change that is a function of the x,y-coordinates, proportional to the projection of the potential in the z-direction:

$$\phi(xy) = \int \phi(xyz)dz$$

The phase change of the electron wave, relative to a wave transmitted through a vacuum (ϕ=0), is given by the product of ϕ(xy) and an interaction constant $\boldsymbol{\sigma}$, which defines the strength of the interaction of electron waves with matter. Mathematically, the effect on an incident wave of the phase change is given by multiplying the incident-wave amplitude by a transmission function

$$q(xy) = exp[-i\boldsymbol{\sigma}\phi(xy)]$$

This equation is called the phase-object the phase-object approximation (POA).

Special preparation techniques are needed to produce specimens the required ~100 Å thickness, and the thickness limitation depends on the experimental conditions. For an ideally perfect lens, the image wave function likewise has a phase modulation but no amplitude modulation, so the image-intensity distribution is a constant where the image contrast is zero. To derive some information from the image concerning the object structure, we must use an imperfect lens (which means losing resolution), or resorting to the use of analogs of one of the phase-contrast-imaging schemes used for light optics[97]

2.1.3. Electron energy loss spectroscopy

EELS relates to energy measurements applied to thin specimens through incident electron beams. There are several ways in which incident electrons can interact with a specimen to generate various characteristics in the energy loss spectrum. One of the most important energy loss processes that can be performed is atomic ionization, in which electrons are emitted from the inside or core of the specimen's shell. This process requires energies equal to or greater than the critical ionization energy, *Ec*, defined specifically for the core electrons as a function of specific atoms and specific electron shells. That is, at the energy loss level corresponding to *Ec*, a characteristic signal such as an ionization edge appears in the spectrum to confirm the presence of a specific element in the specimen. The edge intensity can be directly and quantitatively related to the amount of the element present. In addition to containing quantitative elemental information, the ionization edge has a small intensity variation just above the edge onset, called the energy-loss near-edge structure (ELNES).[98] ELNES depends on the details of the local nuclear environment, such as coordination and combination types. Understanding the relationship between these microstructural measurements, the electronic structure, and the ultimate properties of materials can provide solutions to many important problems that could not be solved previously. This is especially true if the change in bond length occurs over a small range of lengths.

In the ionization process, the inner shell electrons are given enough energy to overcome the nuclear attraction and are excited by the unfilled energy level if the sample does not fully escape. These unfilled energy levels are a function of the overall electron distribution because of the manner in which atoms and their neighbors (that is, ionized atoms) are bonded to adjacent atoms. Thus, during the ionization, the atoms themselves are converted from the base state of the core shell into the excited state of the core shell with an empty state or hole and excited core electrons at the previously empty energy level. The possible energies that can be applied to the emitted electrons are controlled by the distribution of these unfilled states. Thus, the variations in intensity of the ELNES, which is the ionization edges, are directly related to the distribution of the unfilled electron state and can be interpreted as the bonding state of the ionized atoms.

Besides determining the basic ionization edge type, matrix terms have other important consequences. Generally, there is a possibility that the transition matrix element is not zero and only certain combinations of the initial state and final state are switched. Firstly, the matrix term is not zero; this is called the dipole selection rule, which means that ELNES is a subset of the entire DOS that is part of the appropriate angular momentum symmetry. Secondly, the integral equation involves the multiplication of the initial state and the final state, and this wave function is of significant size only if it is spatially redundant. The initial state is an atom of a state and the final state must have localized components at the same atomic site. For these reasons, the ELNES measures the site and is called a symmetrically planned DOS.[98]

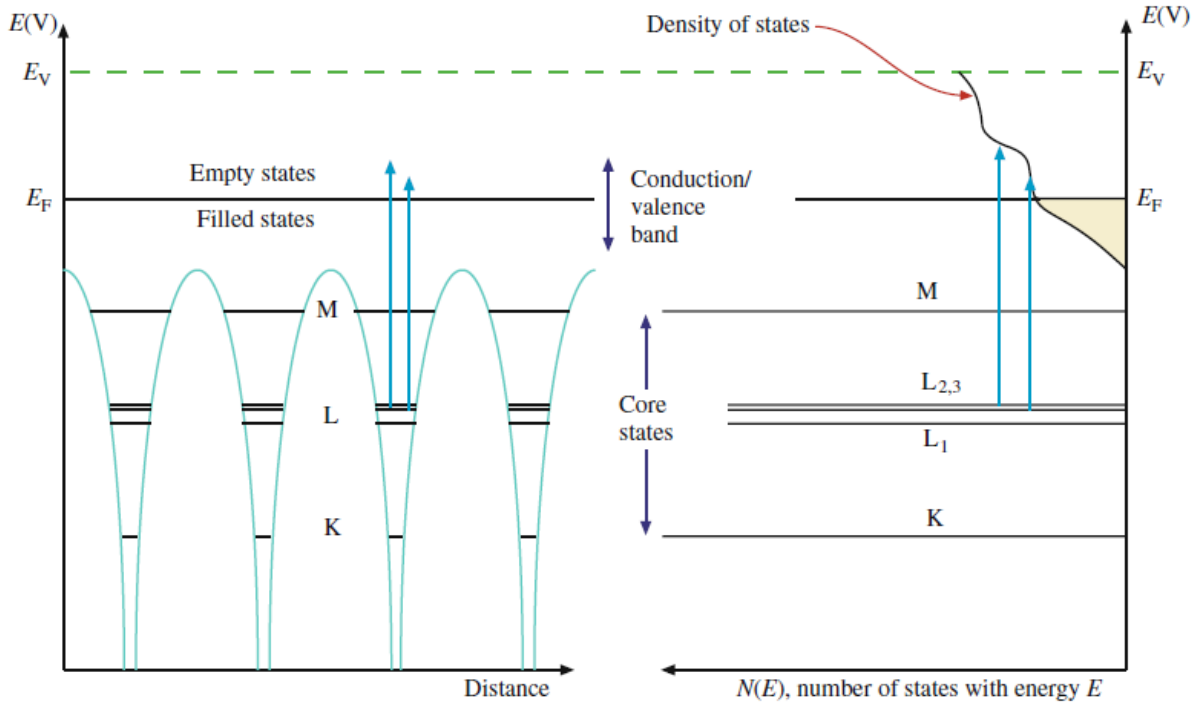

Figure 2. The relationship between the classic energy diagram of a metal atom (left) and the density of the filled and empty states in the conduction/valence band (right).[175]

2.2. Two-Dimensional Materials and Atomic Defects

2.2.1. Crystal structures and knock-on thresholds of graphene, hBN and MoS_2

Graphene is the name given to a flat monolayer of carbon atoms tightly packed in a 2D honeycomb lattice. Graphene has been studied theoretically[99-101] and is widely used to describe the properties of various carbon-based materials. A single atomic plane is a 2D crystal, but 100 layers of graphene is considered a thin film of a 3D material. In graphene, the electronic structures evolve rapidly as the number of layers approaches the 3D limit of graphite at 10 layers.[102] Also, with only a good approximation to graphene, the bilayers have a simple electronic spectrum: they are all gap-free semiconductors. For three or more layers, the spectrum becomes increasingly complex. This allows us to distinguish graphene from mono-, di- and multi- (3 to <10) layers into three types of 2D crystals. The thick structure should be regarded as a graphite thin film for all purposes

Several similar studies have been performed in hBN and MoS_2. These studies focus on information about edge composition and chemical stability that can significantly impact performance testing and performance. Although these three lattices are each hexagonal, graphene is composed of a single element of carbon, hBN has alternating planar elements of boron (B) and nitrogen (N), and each molybdenum (Mo) and sulfur (S) in MoS_2 has a ratio of 1:2 in triangular prism unit cell sandwiched between sulfur layers (Figure 3). Each material has its own composition and thus shows all the other features such as the formation process of hole defects in graphene, hBN and MoS_2 as described below in terms of the edge structure, stability and resultant properties. When an electron beam is irradiated on a 2D specimen with a high electron energy, the atomic bond in the material is released from the lattice leaving a hole in the material, which is called the knock-on voltage. The atom displacements, knock-on thresholds and other structural information of graphene[103], hBN[104] and MoS_2[105] are summarized in Table 1.[106]

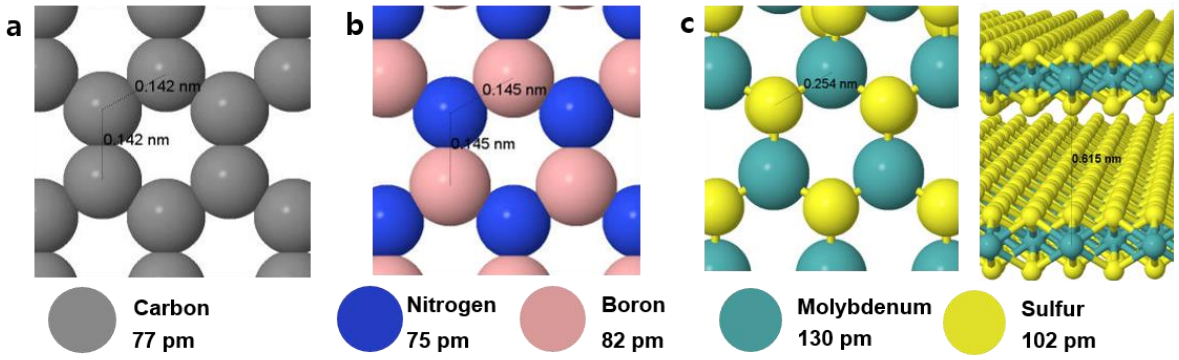

Figure 3. Crystal structures of (a) graphene, (b) hBN and (c) MoS_2.[106]

Table 1. Structural data of monolayer graphene, hBN and MoS_2.[106]

Reference	Material	Atomic number	Lattice system	Lattice parameter (Å)	Displacement threshold (eV)	Knock-on threshold (kV)
Smith & Luzzi (2001)	Graphene	C: 6	Hexagonal	2.46	17	86
Kotakoski et al. (2010)	hBN	B: 5	Hexagonal	2.51	B: 19	79.5
		N: 7			N: 23	118.6
Komsa et al. (2012)	MoS_2 (2H)	S: 16	Hexagonal	3.2	S: 6.9	80
		Mo: 42			Mo: 20	560

2.2.2. Atomic defects on 2D materials

Characterization of the atomic defects is critical to a fundamental understanding of material properties. The nature of atomic bond structures provides direct information on bulk electronic and mechanical properties. Aberration-corrected high-resolution TEM (AC-HRTEM) can provide insights into the bond structure of atoms as well as local characteristics such as electronic structure information.[90, 107-110] For 2D materials such as graphene, hBN and TMDs[70, 111-112], TEM is an ideal characterization tool because it can image materials with high spatial and temporal resolution without a substrate support.[64]

ACTEM gives insight into the dynamic behavior of the defect structure of graphene. During imaging, the electron beam can be used to create defect structures while at the same time providing the energy required to induce atomic motion in the specimen. In this way, the dynamics of carbon atoms were observed at the edge of an electron beam-induced hole, giving insight into the relative stability of the zigzag edge and the armchair edge.[64] Figure 4a shows an electron beam-generating hole with the armchair edge highlighted. As the armchair edges are eroded, the hole shows a more faceted structure with visible zigzag edges (Figure 4b). The observed stability can be explained by a simple model that takes into account the adjustment of active edge sites. A pair of dislocations consisting of an adjacent pentagon and heptagon are created using an electron beam and then used to image the process by inducing a displacement of the potential in the lattice and very clearly identifying all the atoms in the lattice. The captured dynamics of the two processes and corresponding atomic models are shown in Figure 4d–i.[94]

One of the inherent characteristics of a graphene grating is its ability to form a non-hexagonal loop and reconstruct it. The simplest example is the Stone-Wales (SW) defect[113] that does not contain removed or added atoms. The four hexagons are converted into two pentagons and two heptagons by rotating one of the C-C bonds through 90° as shown in Figure 4j [SW (55-77) defect].[114] The simplest defect is the missing atom in lattices Monovacancy (MV) in graphene has been experimentally studied by TEM[114-115] and STM.[116] As shown in Figure 4k, the MV undergoes a Jahn-Teller distortion and induces two saturations of three suspended bonds towards the missing atom. For geometric reasons, there is always a one-time bond. This leads to the formation of a five-membered and a nine-membered ring [5-9 defect]. Divacancy (DV) can be generated by merging two MVs or by removing two adjacent atoms. As shown in Figure 4l, there is no dangling bond in a fully reconstructed DV, so two pentagons and one octagon [5-8-5 defect] appear instead of four hexagons as in complete graphene. The atomic network maintains consistency with small perturbations in the bond length around the defect.

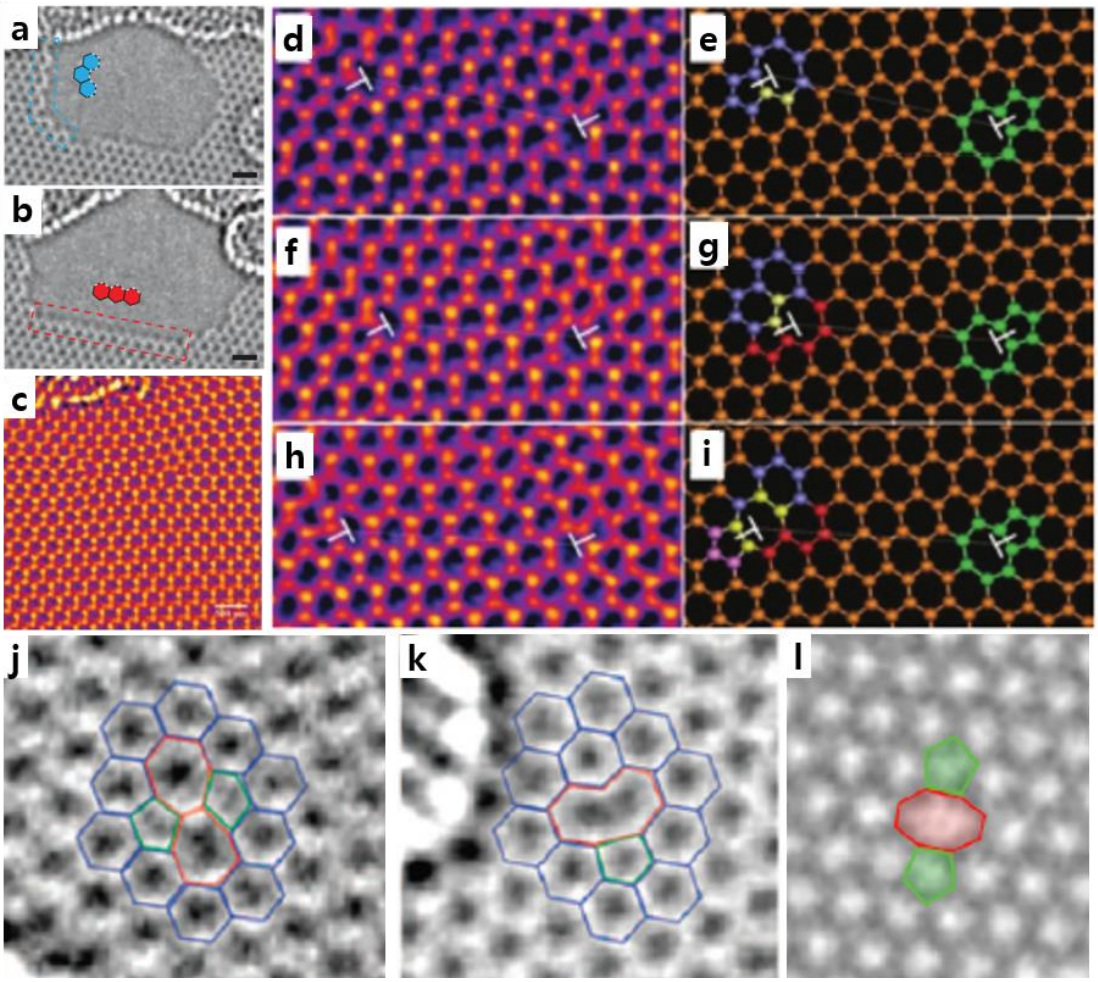

Figure 4. Atomic defects in monolayer graphene. (a) Edge configuration of an electron beam created hole in highlighting the armchair edge. (b) Growth of the hole showing an extended zigzag edge.[64] (c) Pentagon and heptagon dislocation pair. (d)-(i) ACTEM images and atomic structures of the dislocation pair movement with the carbon lattice.[94] (j) Stone-Wales (SW) defect. (k) Monovacancy (MV). (l) Atomic structure of reconstructed divacancy (DV) defects.[114]

hBN is a 2D material having structural characteristics like graphite with a similar crystal lattice and layer spacing. Unlike semi-metallic graphene, which has a high in-plane conductivity, hBN is an insulating material with a large bandgap across the stacked layers. Each individual sheet consists of boron and nitrogen atoms arranged in a partial ionic bond with a honeycomb lattice. The bulk material consists of these individual sheets stacked with alternating layers of boron and nitrogen atoms beneath the column (Figure 5a). This AA'A stacking is in contrast to the ABA stacking commonly found in graphite (known as the Bernal structure).[67] When all the atoms are identified, we find that boron atoms are mainly released from the lattice due to electron beam damage. As the hole grows, a triangular-shaped hole is formed and ends up with nitrogen atoms. An ACTEM image of a boron monovacancy and extended triangular hole is shown in Figure 5b–d. When defects and vacancies are produced in bilayer hBN, the material undergoes considerable interlayer bonding as opposed to bilayer graphene, in which interlayer bonding leaves vacancies and holes independently between layers.[67, 117] An experimental image and a schematic model of this defect site are shown in Figure 5e. The ability to accurately determine the layer thickness and identify atomic species in hBN samples opens up the possibility to study grain boundary defect structures in polycrystalline samples.[118-119] Like graphene, hBN can be synthesized on a macroscopic length scale on a suitably grown substrate such as copper or nickel with boron- and nitrogen-containing precursors. Individual non-nucleated islands grown on a metal substrate are extended and fused onto the surface in various crystallographic directions to form a continuous 2D sheet. The grain boundaries between two single crystal regions were connected through pentagon and heptagon (5|7) defects rather than square and octagon (4|8) defects (Figure 5f and g), which are predicted to be more stable since they avoid homonuclear bonding at the defect sites.[119] Both structures are energetically stable, but local deformation of the sheet can affect which defect is preferred. In the experimental setup, noticeable deformation is present as evidenced by dynamic observations of lattice relaxation and potential motion during imaging, which may favor 5|7 dislocations.

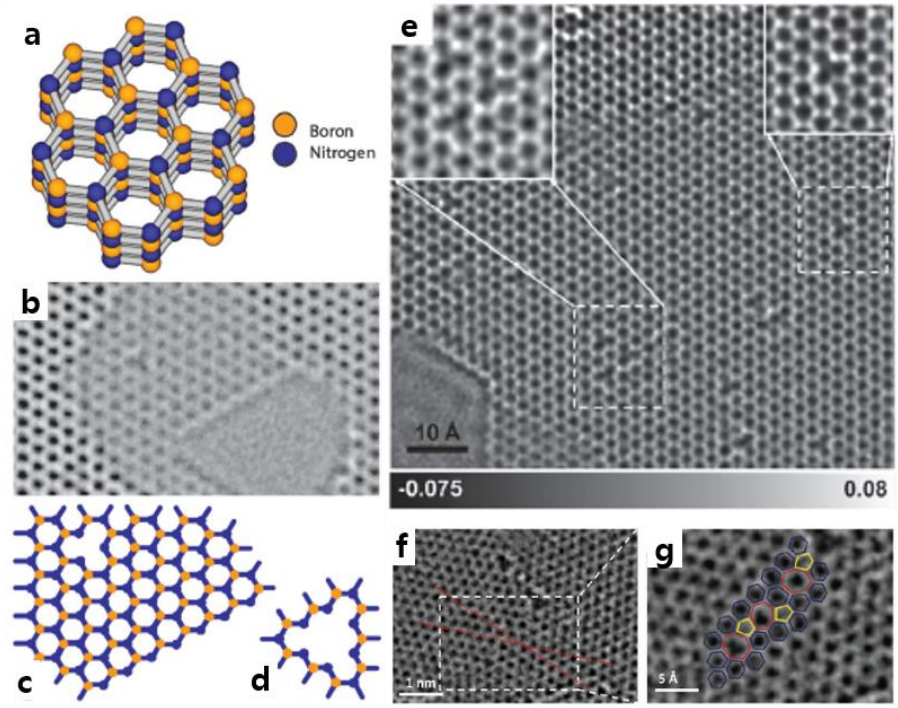

Figure 5. Atomic defects in hBN. (a) Atomic model of stacking structure. (b) ACTEM image showing a boron vacancy and nitrogen terminated edge. (c) Atomic model of vacancy. (d) Atomic model of triangular hole with nitrogen-terminated edge.[67] (e) Large area image of hBN sheet showing many boron vacancies. (f) Tilt grain boundary in polycrystalline material with a 21° relative angle. (g) Magnified region from (f) highlighting the pentagons (yellow), heptagons (red), and hexagons (blue) at the boundary.[119]

A TMD is a type of stratified material that has received much attention in the scientific community in recent years. Of particular note are the disulfides and diselenides of molybdenum and tungsten, which have interesting optical and electronic properties that depend heavily on the number of layers present. This material consists of a layer of transition metal atoms (molybdenum or tungsten) located between two layers of chalcogen atoms (sulfur or selenium). In the original crystal structure, each metal atom is 6-fold coordinated while the chalcogen atoms are 3-fold coordinated. With these three atomic layers for each isolated monolayer, the structure is more complicated when compared to mono-atomic graphene or two-atom hBN. Like graphene, the grown film is polycrystalline and can be transferred to a variety of materials through appropriate processing. High-resolution electron microscopic characterization was also performed to understand atomic scale defects including single wall, multiple atomic defects and grain boundary structures.[120] The tilt and mirror grain boundaries often appear with unique optical and electronic properties. By using AC-STEM imaging, the atomic structures of various defects and boundary structures provide the information required to understand the measured bulk properties. One unique feature of TMDs compared to graphene or hBN is the presence of a half-site defect structure in which the metal atom can occupy the position of a chalcogen atom pair or the chalcogen atom pair can occupy a metal atom site. Antisite defects of MoS_2 show that the hexagonal network collapses when the molybdenum atom replaces the sulfur pair in the lattice, whereas the sulfur pair replaces the molybdenum atom while maintaining the crystal lattice symmetry (Figure 6a–d). The complex bonding capability of the atomic components of TMDs allows for an interesting boundary structure. In tilt boundaries, new 4|6 and 6|8 dislocations are observed along with conventional 5|7 dislocations, which are believed to be the result of variations in the local concentrations of reactant species during growth. A collection of dislocation structures observed in MoS_2 tilt boundaries is shown in Figure 6e–i. In mirror boundaries, 4|4 and 4|8 line defects exist between neighboring crystalline domains and contain kink sites that have 4-fold over coordinated metal atoms junctions. The AC-STEM images and atomic structures are shown in Figure 6j–n. In addition, the phase boundary and its dynamic behavior can be observed in these materials, where a metallic (1T) and semiconductor (2H) phase are present at the same time in a monolayer.[121]

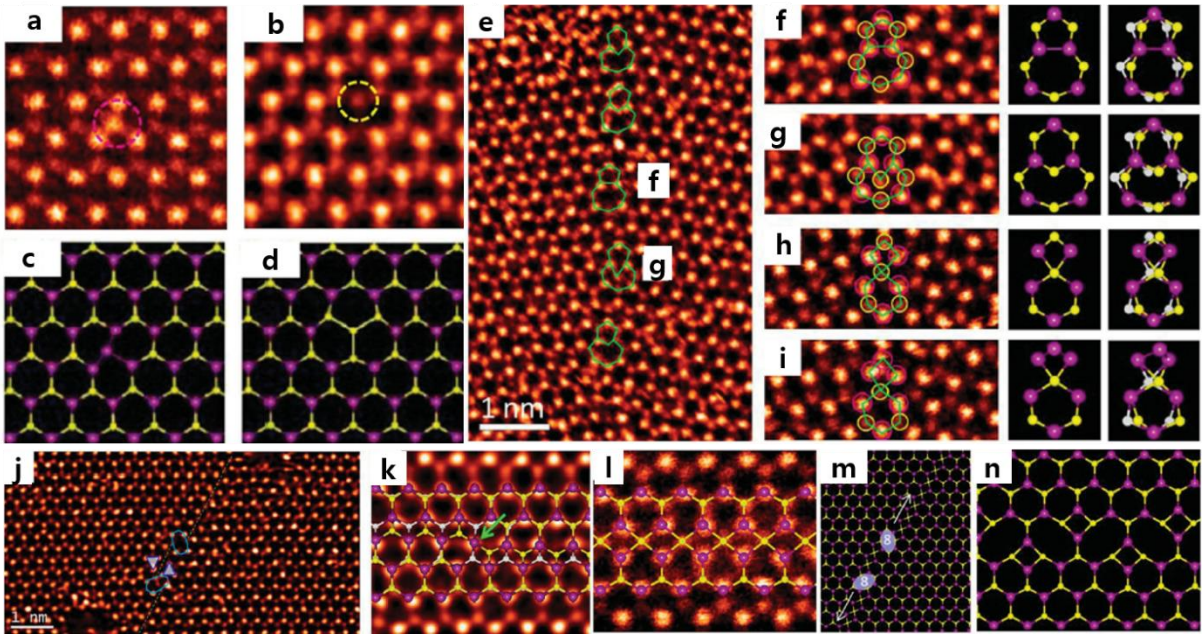

Figure 6. Atomic defects of MoS_2. (a) and (b) Antisite defects with molybdenum or two-atom sulfur replacements, respectively. (c) and (d) Atomic models of (a) and (b) with molybdenum atoms shown in magenta and sulfur atoms shown in yellow. (e) Tilt boundary in MoS_2 with a 18.5° angle. (f) and (g) 5|7 and 6|8 dislocations taken from (e). (h) and (i) Pristine and molybdenum substituted 4|6 dislocations observed in tilt boundaries, respectively. 2D and 3D models are presented along with AC-STEM images in (f) to (i). (j) Image of a mirror boundary in MoS_2. (k) Kink in an MoS_2 mirror boundary with 4-fold coordinated molybdenum atom. (l) 4|4 mirror boundary AC-STEM image. (m) Atomic model of boundary in (j). (n) 4|8 mirror boundary structure, representing the highest possible kink density.[120]

Chapter 3. Objective and Ideas

3.1. Structural Understanding of Atomic Defects Formed by Dry Oxidation Treatments in Monolayer Graphene Sheet

Among a lot of known oxidation treatment methods, ultraviolet–ozone (UV/Ozone) and oxygen plasma treatments have various benefits: both treatment do not use severe chemicals and can oxidize materials at specific sites through sacrificial-layer masking.[11] Both treatments are widely used to modify the surface of materials because these processes are facile and accessible. However, UV/Ozone and plasma treatments fundamentally different processes, they are presumed to induce similar oxidation effects. A UV/Ozone treatment removes organic molecules from a material's surface and can also be used for surface modification.[12-14] However, plasma treatment is able to impact a surface with energy sufficient to break the molecular bonds on the surface of the materials. These dry oxidation treatments are also commonly applied to graphene to modify the surface or remove contaminants. However, these treatments may be revealed to induce the formation of different types of defects on the surface of graphene because the UVO treatment causes a chemical reaction, whereas the oxygen plasma treatment causes both physical and chemical reactions at atomic scale. So, it is necessary to prove effects of both treatments on monolayer graphene sheet at atomic scale since, structural defects in 2D materials are very important part since these can control the properties of materials. Therefore, precise understanding about induced defects is essentially required, and then additional applications and studies should be considered.

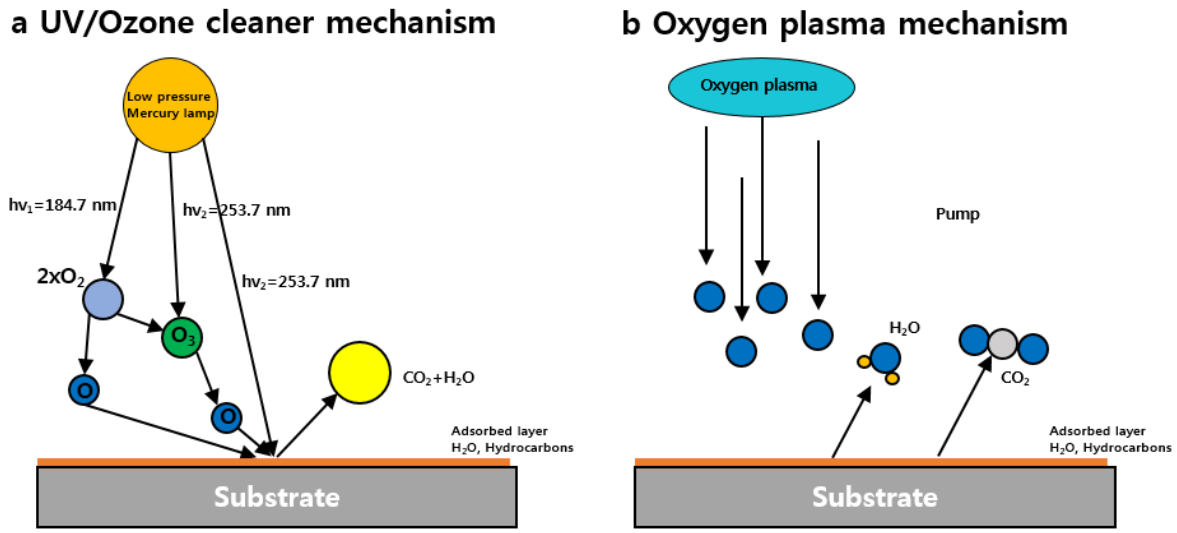

Figure 7. Schematics of mechanism of (a) UV/Ozone and (b) oxygen plasma treatments.

3.2. Dynamics of Oxygen and Hydrogen Atom-Driven in Monolayer Graphene to Form Point Defects under Electron Beam Irradiation

The interests in point defects in mono- or multilayer graphene sheets originates in a lot of related researches. Except just academic investigation, defects studies in graphene sheets were first motivated by aspects of radiation damage. Characterization of atomic scale defects is important, since the emerging field of carbon nanoscience draws much useful information from the basic graphene system and for the large part shares behavior in common including defect structure and energetics. Graphene has a wide range of atomic defects. Among them, vacancies arise during growth or as part of the thermal equilibrium concentration. In addition, these induced by the electron beam irradiated during the analysis of graphene, or formed by the influence of dopants attached to the surface. Studies on the vacancy formed in oxidized graphene are accompanied by computational methods, but they are limited to being expressed experimentally. Atomic-scale graphene surfaces with partial surface oxidation can be manufactured by many known methods of oxidation[122-126] and dry oxidation treatments, such as UV/Ozone and oxygen plasma treatments of them can effectively induce[127] adsorption of oxygen atom on graphene lattice[30, 128] on clean graphene surface for short times. These functional group have diverse behavior under electron beam irradiation and can induce point defects.[4] In particular, UV/Ozone treatment is an appropriate oxidation method for TEM observation because UV/Ozone-treated graphene sheets have many oxygen adsorption and clean regions to sufficiently analyze the bonding behavior without topological defects.[127] Therefore, the work here aims to develop a more detailed understanding of vacancy formation mechanism involved oxygen-containing functional groups.

3.3. Triangular Hole Growth from Monovacancy to Extended Large Hole in Monolayer Hexagonal Boron Nitride Sheet

The defect structures in hBN are even more varied and complex because, unlike graphene,[65-66] its hexagonal 2D lattice is occupied by two elements. Indeed, most reports have focused on defect formation and characterization[67, 117, 129-130] in localized regions of exfoliated hBN. At present, it is known that the edges of holes in hBN layers usually adopt zigzag and armchair-type configurations, with the former being more common.[67-68] Moreover, the zigzag configuration contains two different types of terminated edges due to the heterogeneity of hBN, factors that have been shown to affect the material's intrinsic electrical properties.[69] The growth mechanisms of extended holes in hBN are also not well established. For example, unlike graphene, where single chains of carbon atoms and related defects are well characterized,[131-136] single chains made deliberately in hBN sheets via in situ production techniques (i.e., inside a transmission electron microscope) have been observed at 650 °C.[137] Studies on the holes formed in the single-layer hBN are very numerous, but it is difficult to explain the step-by-step process from the hole to the extended hole. Therefore, it is necessary to establish the hole formation process by using the acceleration voltage considering the hBN knock on threshold.

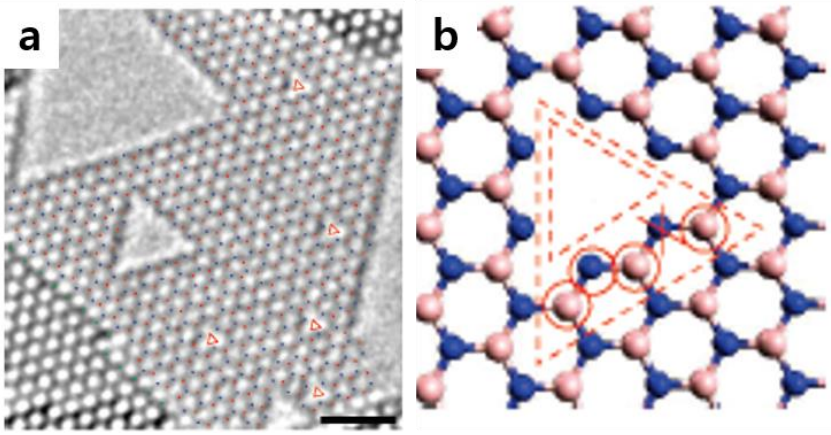

Figure 8. Nitrogen terminated edge of hole in hBN under electron beam irradiation.[130]

3.4. Line-Defect Mediated Formation of Hole and Mo clusters in Monolayer Molybdenum Disulfide Sheet

In the case of in situ experiments of 2D materials using TEM, a hole is induced with a variety of processes by prolonged electron beam irradiation due to the unique displacement threshold of the materials under electron beam. In graphene and hBN, once vacancies are formed in the sheet[35, 105, 138], these are enlarged and become holes.[64, 130] But, in the case of MoS_2, S vacancies are firstly formed due to displacement threshold of S atoms, which is accurately estimated including the effects of lattice vibrations on the energy transferred from electron to a target atom.[105, 139] And S vacancies increase vacancies concentration[80], and then line defects well described by a row of S vacancies appear instead of forming holes during prolonged exposure to electron beam.[79] In the event that holes are formed in the monolayer MoS_2 sheet, Mo atoms are aggregated around the edges of holes, while S atoms are simply knocked off due to the higher displacement threshold of Mo compared to S.[80-81] In the formation process of holes in MoS_2 sheet, line defects are inevitable, but line defect mediated hole formation mechanism has not been reported. The hole formation mediated by line defects in monolayer MoS_2 sheet is found using ARTEM. The defects formations as well as aggregated Mo clustering from monolayer MoS_2 sheet were investigated under electron beam irradiation with an imaging aberration corrector.

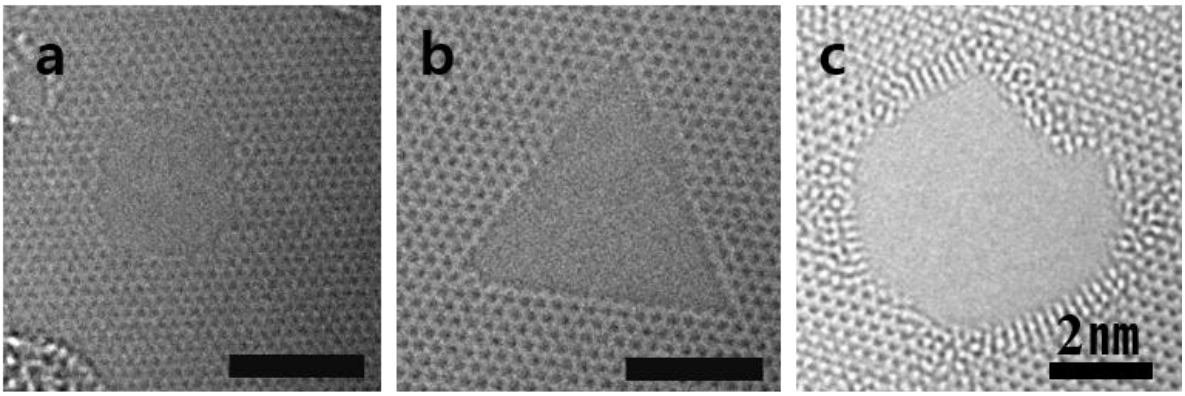

Figure 9. Hole formation under electron beam irradiation in monolayer (a) graphene, (b) hBN and (c) MoS_2.[106]

Chapter 4. Experimental Procedure

4.1. Graphene

4.1.1. Synthesis of monolayer graphene sheet using CVD

Graphene sheet was synthesized by CVD onto a 25-μm-thick copper foil (99.8% Alfa Aesar, 13382). First, 25-μm-thick copper foils (99.8% Alfa Aesar, 13382) were washed with HCl/H_2O (1:10), rinsed with acetone and alcohol, and then dried under ambient air. The dried copper foil was inserted into a quartz tube and heated to 1000°C under H_2 flowing at 2 sccm at 10 mTorr. After the sample was annealed for 1 h, a gas mixture of CH_4 (10 sccm) and H_2 (2 sccm) at 100 mTorr was introduced for 25 min to synthesize graphene. Finally, the sample was rapidly cooled to room temperature under a flowing mixture of CH_4 (10 sccm) and H_2 (2 sccm). The synthesized sheet was subsequently transferred onto TEM grids via direct transfer [140].

4.1.2. UV/Ozone and oxygen plasma treatments

UV/Ozone treatments were performed using a UVC-30UV ozone cleaner (Jaesung Engineering Co.). The TEM grid transferred synthesized graphene sheet was positioned in the center of the chamber and then UV/Ozone is treated for 60 s, 120 s, 180 s, 240s and 300 s.

Oxygen plasma treatments were carried out using a PDC-32G plasma cleaner (HARRICK PLASMA). The synthesized graphene sheet transferred onto a TEM grid positioned ~10 cm from the entrance of the chamber. These treatments were carried out at a power of 18 W and at a chamber pressure of 140 mTorr.

4.1.3. Observation of defects using ARTEM

Monolayer graphene sheets which are treated UV/Ozone and oxygen plasma treatments were analyzed using an aberration-corrected FEI Titan Cubed transmission electron microscope (FEI Titan^3 G2 60-300), which was operated at an acceleration voltage of 80 kV and with a monochromator. The microscope provides sub-angstrom resolution at 80 kV and −13 ± 0.5 μm of spherical aberration (Cs). Typical electron beam densities were adjusted to approximately 6×10^5 e^- nm^{-2}. The atomic images were collected using a white atom contrast to obtain actual atom positions under properly focused conditions, which were needed for direct image interpretation.

4.1.4. Characterization using Raman spectroscopy and XPS

Raman spectra were recorded using an Alpha 300s micro-Raman spectrometer (WITec) equipped with a 532-nm laser. Chemical structures of the treated graphene sheets were identified by XPS using an ESCALAB 250Xi (Thermo Scientific) equipped with Al Kα X-ray source.

4.2. Hexagonal Boron Nitride

4.2.1. Synthesis of monolayer hBN sheet using CVD

The hBN sheets were synthesized using chemical vapor deposition.[141] Ammonia borane (NH_3−BH_3) was used as the precursor. Borazine is moisture sensitive and can be hydrolyzed to boric acid, ammonia, and hydrogen. To grow monolayer hBN sheet on platinum foil, the temperature within the low-pressure CVD system was set to 1100 °C, and the precursor, ammonia borane, was heated to 130 °C, since it decomposes into hydrogen, polyiminoborane (BHNH; solid), and borazine ($(HBNH)_3$; gas) at this temperature. The produced borazine gas was made to diffuse from the source bottle into the furnace, where it was adsorbed onto the platinum foil. Monolayer hBN sheet was thus formed from borazine via thermal decomposition as shown in Figure 10.

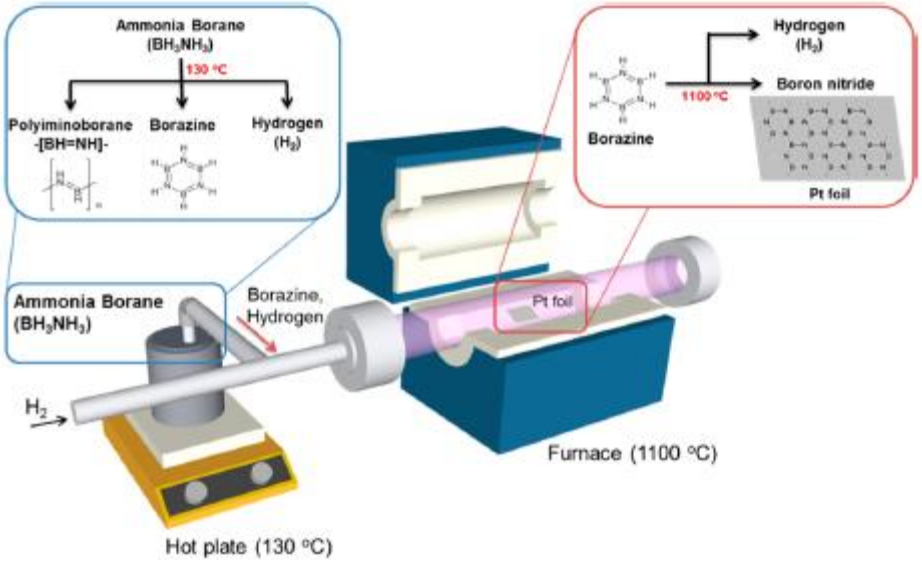

Figure 10. Schematic diagrams of the LPCVD system used for monolayer hBN sheet growth.[141]

4.2.2. Observation of defects using ARTEM

Conventional TEMs do not have adequate resolution for imaging single atoms of hBN and are often operated at high voltages, which lead to immediate irradiation damage in the specimens before reliable observations can be made. Furthermore, if experiments are performed at a low voltage such as 60 kV, knock-on damage as well as ionization damage should be considered. To avoid these problems, specimens were analyzed using an aberration-corrected FEI Titan Cube TEM (FEI Titan3 G2 60-300), which was operated at 80 kV acceleration voltage since 80 kV is an intermediate value of the knock-on threshold values of B (74 kV) and N (84 kV).[142] Therefore, our experiments mainly consider the knock-on damage. The microscope provides sub-Angstrom resolution at 80 kV and -21±0.5 μm of spherical aberration (Cs) with a monochromator and thus is capable of imaging individual atoms within the hBN lattice. Typical electron beam densities were adjusted to around 5x105 e^{-} nm^{-2}. We analyzed the atomic images using a white atom contrast (as opposed to a black atom contrast[130]) in order to obtain actual atom positions under properly focused conditions needed for direct image interpretation. After acquiring a series of images using the Gatan Digital Micrograph (DM) Script, structural changes in the observed area were analyzed frame-by-frame. Each of these images was taken with an exposure time of 0.5 sec and an interval time of 1.7 sec. To facilitate the identification of the holes generated by electron beam irradiation, clean areas that were free of adsorbates and other impurities were examined.

4.2.3. DFT calculations and MD simulations

Density functional theory calculations were performed using the Vienna ab initio simulation package (VASP).[143-144] A single k-point (Γ point) for a 15 x 15 supercell with a cutoff kinetic energy of 400 eV was used. The ions were represented by projector-augmented wave (PAW) potentials,[145-146] and van der Waals (vdW) interactions[147] as used in Grimme's theory were implemented into the VASP. A generalized gradient approximation was used to describe the exchange-correlation functional.[148-149] The atomic positions of all structures were relaxed until the Hellmann-Feynman forces were lower than 0.01 eV/Å.

To explore hole growth in layers of hBN, molecular dynamics (MD) simulations were performed using the large-scale atomic/molecular massively parallel simulator (LAMMPS) code with reactive force field (ReaxFF) potentials.[150-152] The MD time step was set to 0.25 fs, which was determined from a stability test using a microcanonical ensemble (NVE). To properly account for the electron beam irradiation, heating was controlled during simulation by increasing the temperature from 1000 K to 4000 K for 1000 ps using a canonical ensemble (NVT) and the Nose-Hoover chain thermostat.

4.3. Molybdenum Disulfide

4.3.1. Synthesis of monolayer MoS_2 sheet using CVD

The MoS_2 sheets were synthesized using CVD [153]. The synthesis of MoS_2 begins with the deposition of Mo metal on SiO_2/Si or a quartz wafer by electron beam evaporation. The thickness of the molybdenum metal layer was varied from 0.5 to 3 nm using a deposition rate below ~0.1 °A s^{-1} under high vacuum conditions. The sample was positioned in the tubular quartz chamber under a rough vacuum (3.4×10^{-3} Torr) and heated up to 750 ℃ within a few seconds under the flow of Ar at a rate of 50 standard cubic centimeters per minute (sccm). In a pre-deposited sample, the surface of the molybdenum metal usually becomes oxidized under the atmospheric conditions. Such surfaces could be reduced by instantaneous reaction with hydrogen gas after reaching a temperature of 750 ℃. After the pre-annealing process, the H_2S/H_2/Ar (1 : 5 : 50) reaction gas mixture was injected to synthesize monolayer MoS_2 over 15 min. The chamber pressure was maintained at 3.1×10^{-1} Torr during the synthesis step. Instantaneous annealing at 1000 ℃ was found to enhance the crystallinity of MoS_2 sheets synthesized under a H_2S/Ar (1 : 50) gas mixture flow. The sample was rapidly cooled down to room temperature by moving of the furnace from the reaction position under an Ar flow rate of 50 sccm.

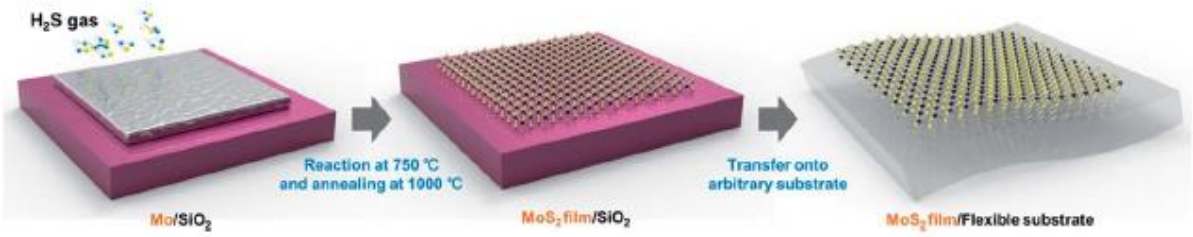

Figure 11. Schematic illustration of the growth and transfer process system used to prepare monolayer MoS_2 sheet.[153]

4.3.2. Observation of defects using ARTEM

Monolayer MoS_2 sheets were analyzed using an aberration-corrected FEI Titan Cubed TEM (FEI Titan3 G2 60-300), which was operated at 80 kV acceleration voltage with a monochromator. The microscope provides sub-Angstrom resolution at 80 kV and -13 ± 0.5 μm of spherical aberration (Cs). Typical electron beam densities were adjusted to around 8 x105 $e^- nm^{-2}$. The atomic images were taken using a white atom contrast in order to obtain actual atom positions under properly focused conditions needed for direct image interpretation. After acquiring a series of images using Gatan Digital Micrograph (DM) scripts, changes of structure in MoS_2 were analyzed frame-by-frame. Each of these images was taken with an exposure time of 0.5 sec and an interval time of 1.7 sec. To facilitate the identification of the defects generated by electron beam irradiation, clean areas that were free of adsorbates and other impurities were observed.

Chapter 5. Results and Discussion

5.1. Graphene

5.1.1. Effects of dry oxidation treatments on monolayer graphene sheet

To clarity the effects of UV/Ozone and oxygen plasma treatments systemically, I analyzed the monolayer graphene sheets treated using the two aforementioned dry oxidation treatments at atomic scale. Figure 1 shows atomic resolution images of UV/Ozone-treated graphene sheets at a variety of UV/Ozone treatment times. Figure 12a shows the pristine graphene which is non-treated monolayer graphene and exhibits little contamination but no dopants or topological defects. Figure 12b shows the graphene sheet after UV/Ozone treatment for 60 s. Unlike pristine graphene, the treated graphene sheets show several attachments of oxygen atoms; these oxygen atoms are components of oxygen containing functional groups (blue squares and yellow squares) on the graphene surface (detailed in supporting information). With increasing treatment time, additional oxygen atoms (Figure 1c) and more contamination are observed, as shown in Figure 12b–d. After UV/Ozone treatment for 300 s, a moiré pattern appears; this pattern is attributed to the monolayer graphene sheet being completely torn and folded by the prolonged treatment.

Figure 13 shows ARTEM images of monolayer graphene sheets subjected to an oxygen plasma treatment for various treatment times. In the case of monolayer graphene treated by oxygen plasma for 5 s (Figure 13b), lattices partially distorted by, for example, topological defects (Figure 13d and e) and attachments of oxygen atoms onto the graphene lattice (yellow squares), are observed. In addition, the number of topological defects increases with increasing treatment time (Figure 13c and f). In the case of treatments longer than 15 s, only small patch-like defect-free regions are observed; other regions are defective and covered with contaminants (Figure 13g–h). The image obtained after 30 s of oxygen plasma treatment is similar to that in the case of the 300 s UV/Ozone treatment. That is, both treatments increase the attachment of oxygen atoms and the total surface area of contaminated regions. However, only the oxygen plasma treatment induces a distorted lattice of topological defects on the graphene.

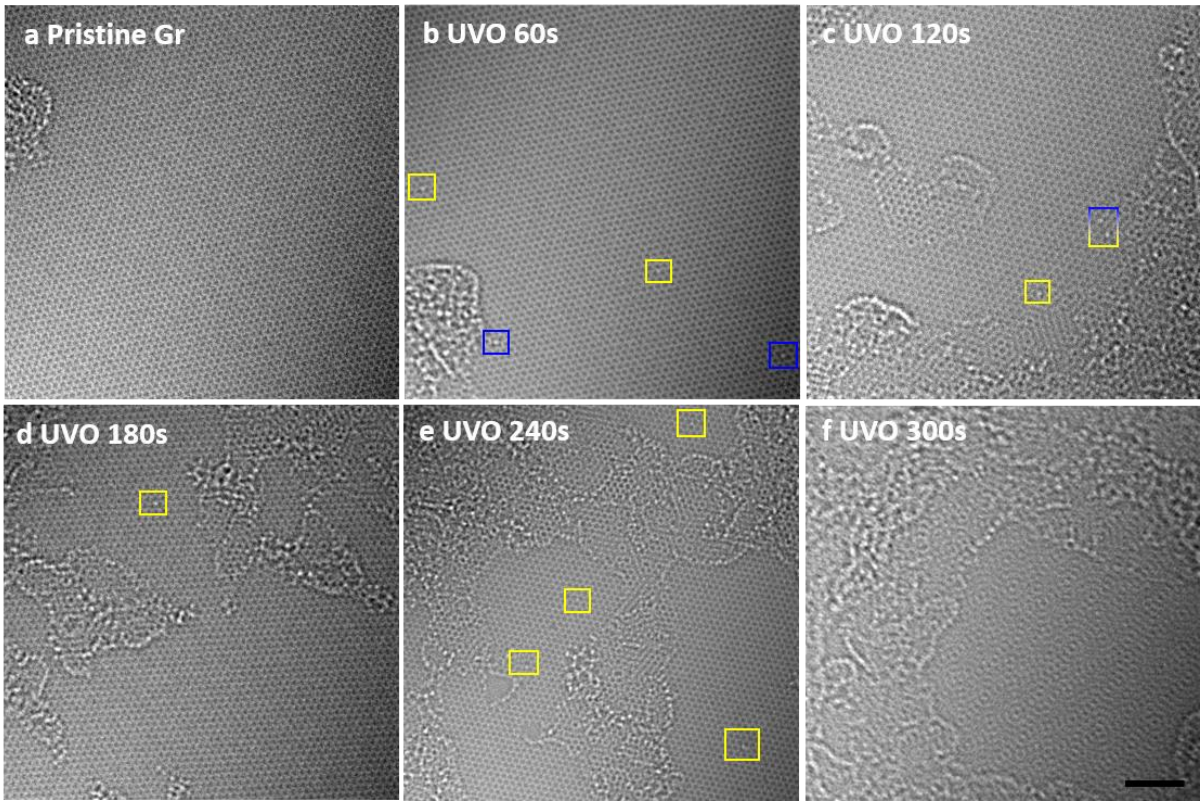

Figure 12. ARTEM images of UV/Ozone-treated monolayer graphene sheets: (a) pristine graphene and (b)–(f) surfaces of graphene partially oxidized for various UV/Ozone treatment times. Yellow and blue squares indicate oxygen containing functional groups. The scale bar is 2 nm.

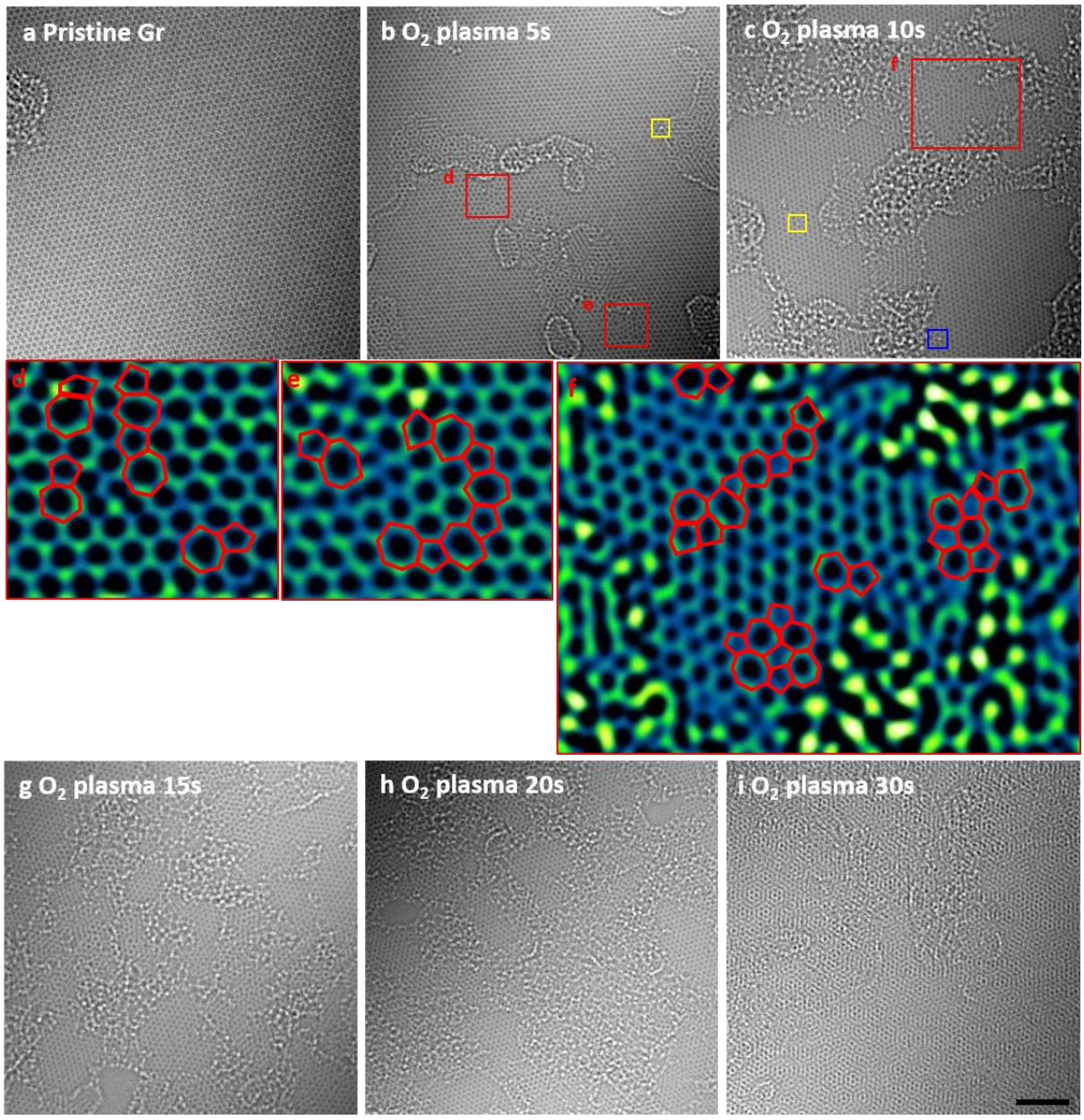

Figure 13. Oxygen plasma-treated monolayer graphene sheets: (a) pristine graphene and (b)–(i) surfaces of graphene partially oxidized for various oxygen plasma treatment times. (d)–(f) Enlarged images of the red squares in images (b) and (c). These enlarged images show topological defects. Yellow and blue boxes indicate oxygen-containing functional groups. The scale bar is 2 nm.

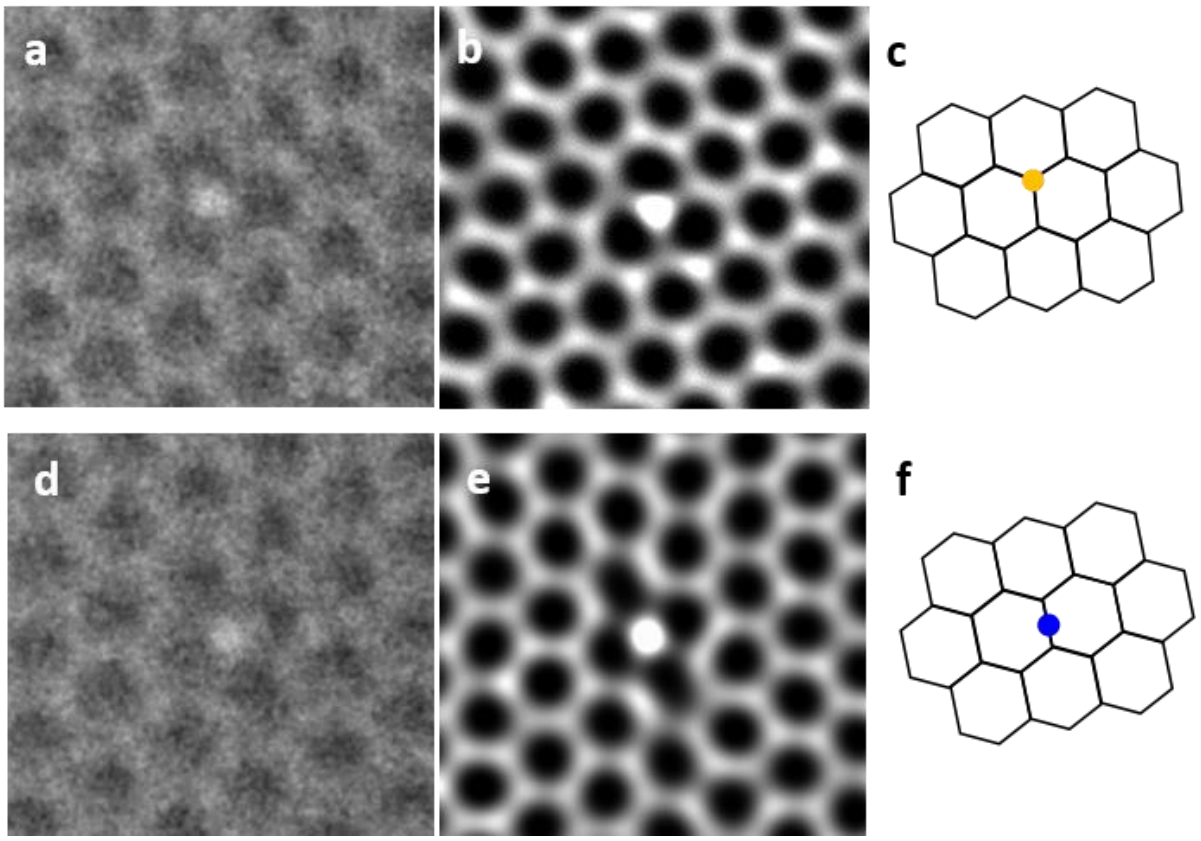

Figure 14. Oxygen containing functional groups induced by dry oxidation treatments. (a, b, c) The raw image, IFFT image, and schematic of an attached oxygen atom at a three-fold symmetry in graphene, respectively. (d, e, f) The raw image, IFFT image, and schematic of an attached oxygen atom on bridge site of C–C bonds of the graphene, respectively.

I prepared the schematics in Figure 15 to be better explain the graphene oxidized by these two dry oxidation treatments. Figure 15a shows UV/Ozone-treated graphene with oxygen atoms attached to its surface (yellow dots and blue dots). By contrast, the oxygen plasma-treated graphene contains topological defects introduced along with oxygen atoms, as shown in Figure 15b. As Figure 15d–f illustrates with overlays, the oxygen plasma-treated sheets have dominantly pairs of 5- and 7-membered-ring defects, which means that the oxygen plasma treatment induced lattice distortions without the loss of C atoms from the graphene lattice while retaining sp^2 bonds. The excited ions in the oxygen plasma may break the graphene lattice. The oxygen plasma is capable of physical and chemical reactions through an ablative effect[154] involving the kinetic transfer of energy from ions to the graphene surface. Although the ablative effect mainly affects the layer of contaminants and the outermost molecular layer of the substrate, oxygen plasma treatment can induce topological defects on the clean atomically thin monolayer graphene regardless of the substrate effect and plasma power.[21] These defects are considered to be formed randomly during the oxygen plasma treatment.

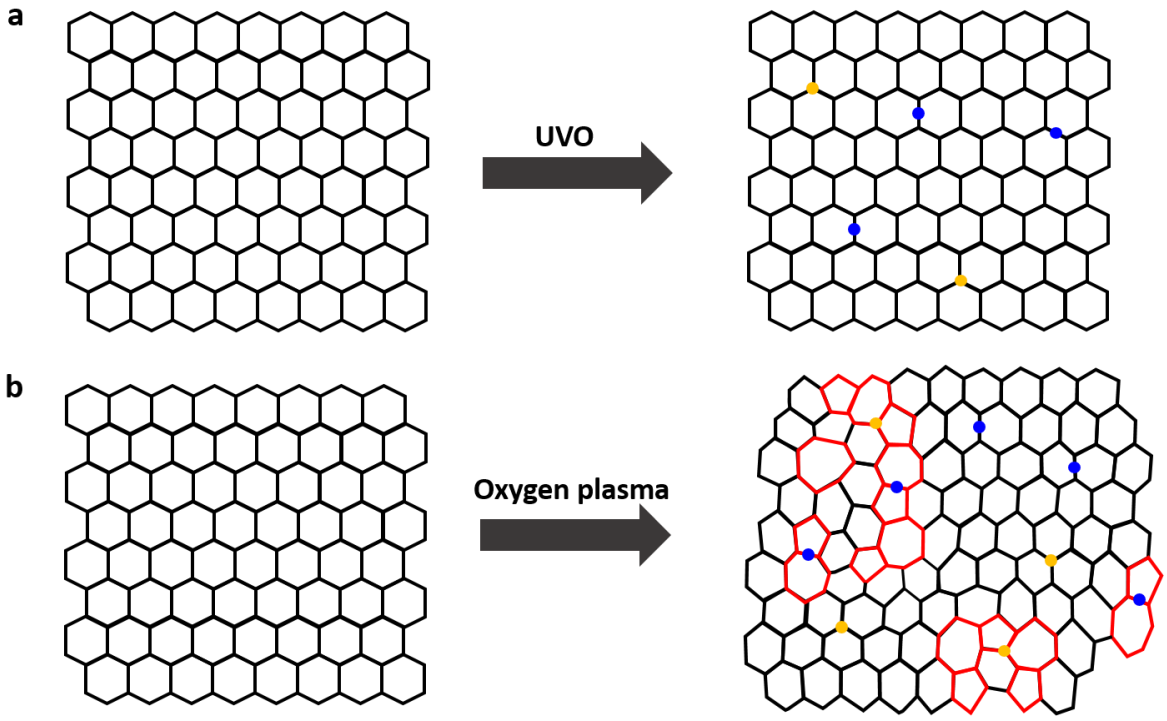

Figure 15. Schematics of oxidized graphene sheets. (a, b) Results of UV/Ozone and oxygen plasma treatments, respectively, on graphene sheets. Yellow dots indicate attached oxygen atoms on 3-fold symmetries; blue dots indicate attached oxygen atoms on bridge site of C–C bonds of the graphene lattice; red lattices indicate topological defects.

Because the contaminants bind preferentially to the defects, the portion of the distorted lattices somewhat underestimated. To achieve a more accurate structural analysis, we carefully removed the contaminants by showering the samples with a low-dose electron beam for 10 min to uncover the defective regions, which were subsequently analyzed. In this process, although oxygen atoms can possibly be detached from the graphene lattice, additional topological defects are not generated in the graphene sheet.[33] In the case of the UV/Ozone-treated sheet, numerous holes are formed but hexagonal lattice symmetry is retained. The six-fold pattern in the diffractogram in the inset of Figure 16a is consistent with a hexagonal lattice. This simple hexagonal pattern of sharp spots is similar to the pattern of pristine graphene and that there are no topological defects. Figure 16c shows an inverse fast Fourier transformation (IFFT) image of Figure 16a from unmasked area of the diffractogram. Since UV/Ozone treated graphene don't have distorted lattices, there is no lattice of graphene without a few contaminations. However, in the case of oxygen plasma-treated sheet, a significant number of topological defects is observed, as shown in Figure 16b. The diffractogram in Figure 16b shows a disordered nanocrystalline pattern compared to that in the inset of Figure 16a. Also, the presence of some disorder is obvious from the broadening of the spots. This broadening results from distorted lattices, i.e., topological defects. Figure 16d shows the IFFT image from the unmasked area of the diffractogram in Figure 16b; this image indicates that distorted lattices vitally exist in the oxygen plasma-treated graphene sheets. Such defects are not observed in pristine graphene sheets. Indeed, the UVO-treated and oxygen plasma-treated graphene sheets were prepared from the same synthesized batch of graphene. We therefore conclude that the high density of topological defects was generated mainly by the oxygen plasma treatment. These topological defects can induce strain to sp^2 carbon bonds because of the curvature in the distorted lattice of graphene, which increases chemical reactivity and structural instability compared to the defect-free regions of graphene.[155] This observation suggests that, because topological defects are formed by the oxygen plasma treatment, oxygen atoms easily attach to the defective regions; as a result, the oxygen plasma treatment results in more effective functionalization than the UV/Ozone treatment.

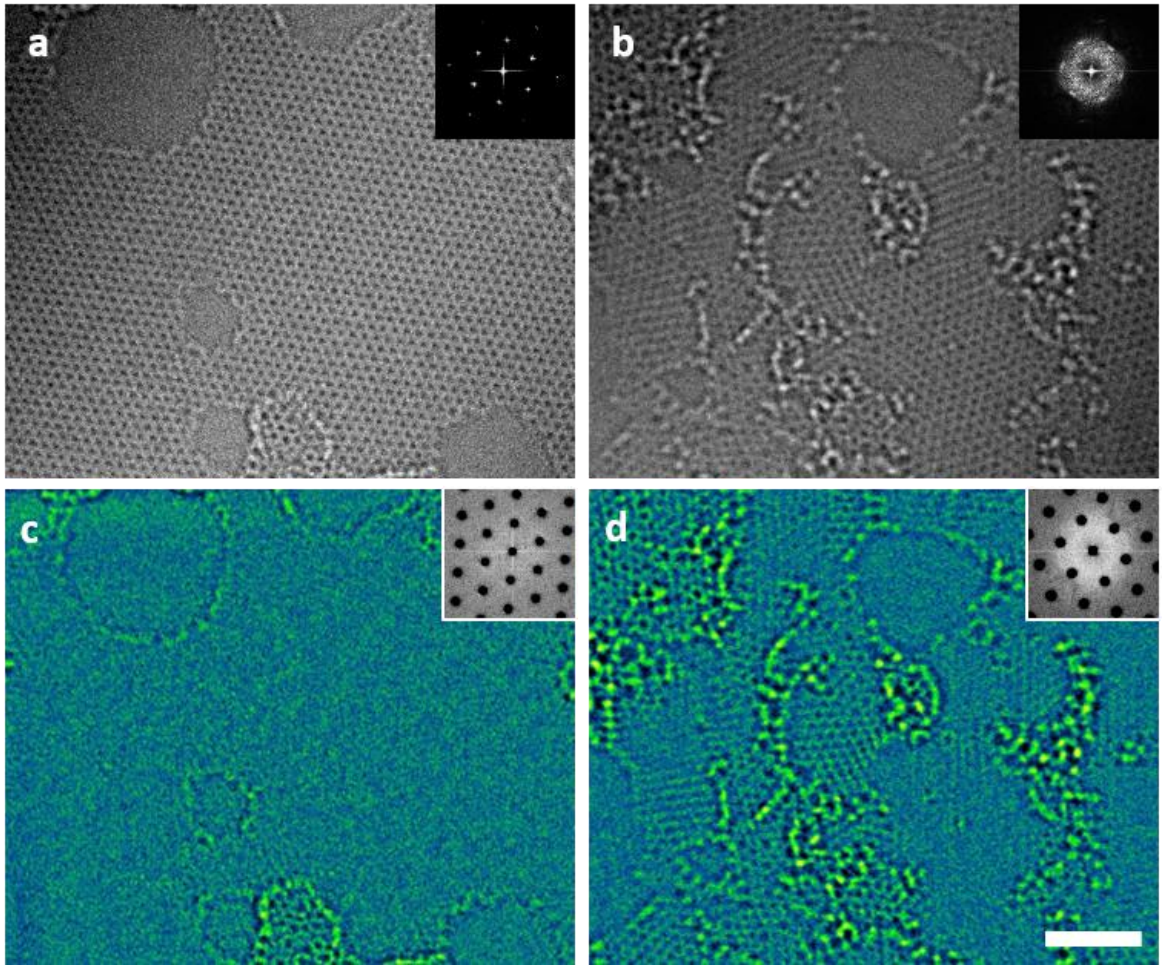

Figure 16. Prolonged electron beam irradiation of graphene sheets subjected to dry oxidation treatments. (a, b) Real images of a UV/Ozone-treated sheet and an oxygen plasma-treated she et, respectively. (c, d) IFFT images from unmasked areas of the diffractograms in (a) and (b), respectively. The scale bar is 2 nm.

Figure 17 shows the EELS of C and O K edge, which represents the specific near-edge structures from graphene treated by two different dry oxidation methods. Since the near-edge structures are extremely sensitive to changes in the bonding, these results can accurately show the oxidation states in graphene sheets. EELS results Figure 17a and b show the C K edge obtained from UV/Ozone and oxygen plasma treated graphene sheet, respectively. These fine structures of the C K edge in oxygen plasma-treated sheets differ considerably from those in UV/Ozone-treated sheets.

As shown in Figure 17a, the **π*** peak is almost sustained and the ***σ**** peak is slightly broadened with increasing treatment time. After more than 60 s of the UV/Ozone treatment, an additional peak appears at approximately 286 eV (red arrows); this peak is assigned to hydroxyl and epoxide groups [23-24, 156-160]. By contrast, the **π*** peak and the ***σ**** peak in the spectra of the oxygen plasma-treated sheets rapidly decrease and are broadened, as shown in Figure 17b. The decrease of the **π*** peak intensity reflects distortion of the local lattices in graphene, and broadening of the ***σ**** peak reflects the attachment of functional groups to the surface. When oxygen plasma is used to treat graphene for 5 s and 10 s, an additional shoulder peak appears at approximately 286 eV, as indicated by the yellow arrows in Figure 17b. After 15 s of oxygen plasma treatment, an additional well-distinguished peak is observed. In addition, another peak appears at approximately 287 eV (black arrow) which is assigned to carbonyl group [123, 161-162] after 20 s of oxygen plasma treatment. Figure 17c and d shows the fine structure of the O K edge from UV/Ozone and the oxygen plasma-treated graphene sheet, respectively. Peaks at approximately 540 eV are observed in Figure 17c. In the spectrum of the monolayer subjected to the UV/Ozone treatment for 60 s, the peak near 540 eV is not clear. However, after a further increase of the treatment time, the 540 eV peak [24, 163-164], which originates from epoxide and hydroxyl groups attached to the graphene surface, becomes distinguishable. The peak at ~540 eV clearly arises after only 5 s of oxygen plasma treatment (Figure 17b) compared to after 60 s in the case of the UV/Ozone treatment (Figure 17c).

The aforementioned results suggest that the core loss regions of the C K and O K edges are very sensitive to the presence of functional groups and to the local distortions in the graphene lattice. These findings reveal that the generation of obvious peaks is related to the treatment methods and conditions of the graphene sheets. According to the EELS results, oxygen atoms are more effectively attached to the surface when graphene is treated with oxygen plasma than with UV/Ozone because topological defects generated by oxygen plasma effectively induce the attachment of oxygen atoms to the graphene surface.

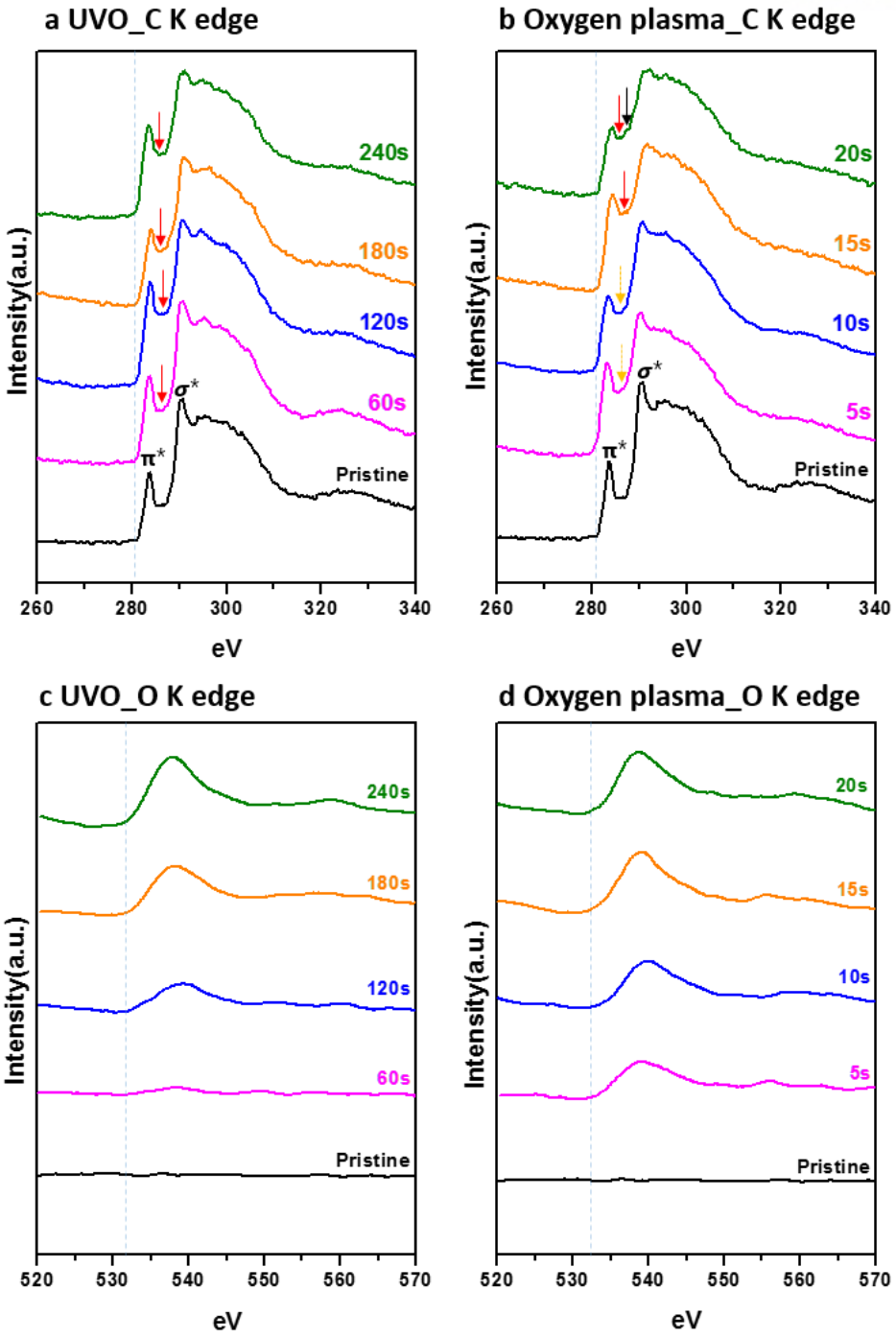

Figure 17. Core-loss EELS of UV/Ozone-treated graphene and oxygen plasma-treated graphene: (a, c) C and O K edges, respectively, of the UV/Ozone-treated sheets; (b, d) C and O K edges, respectively, of the oxygen plasma-treated sheets.

Distinguishing between reduced graphene oxide (rGO) and oxygen plasma-treated graphene sheets using TEM imaging in Figure 18a–b is difficult. However, in the C K edge of EELS, the **π*** edge from rGO is slightly different from the **π*** edge from the oxygen plasma-treated graphene sheet. The former is sharper than the latter, which includes additional peaks of oxygen containing functional groups, as shown in Figure 18c. In Raman spectra, different configurations are observed from the several sheets in Figure 18d.

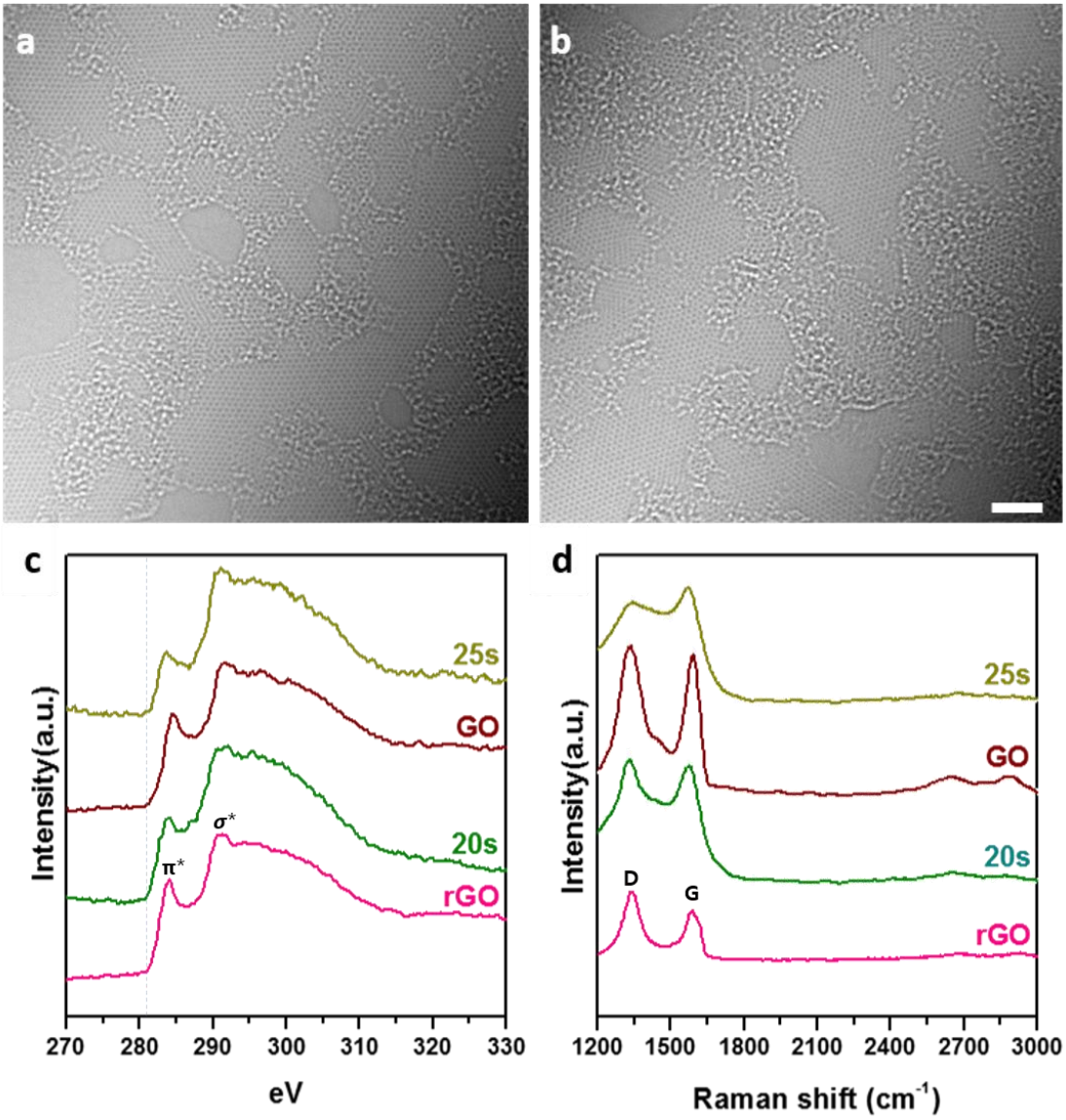

Figure 18. TEM images of (a) rGO and (b) oxygen plasma-treated graphene sheet. (c, d) EELS of the C K edge and the Raman spectra, respectively, of rGO, graphene oxide (GO), and graphene sheets treated by oxygen plasma for 20 s and 25 s. The scale bar is 2 nm.

Raman spectra of UV/Ozone-treated and oxygen plasma-treated graphene are shown in Figure 19. The Raman spectra of the pristine graphene have no D peak associated with lattice disorder. The visible Raman spectra are known to only confirm sp^2 sites by excitation of **π** states, whereas amorphous carbon with sp^3 bonding is known to generate weak spectra. The intensity of the D peak in the spectra of the UVO-treated graphene increases and that of the G peak decreases with increasing treatment time, as shown in Figure 19a. The sheet subjected to UVO treatment for 300 s has no peak because the sheet is almost torn; the same result is observed for the sheet subjected to oxygen plasma treatment for 30 s. In contrast to the UV/Ozone-treated sheets, the peaks from the oxygen plasma-treated sheets show a considerable amount of disorder, as shown in Figure 19.

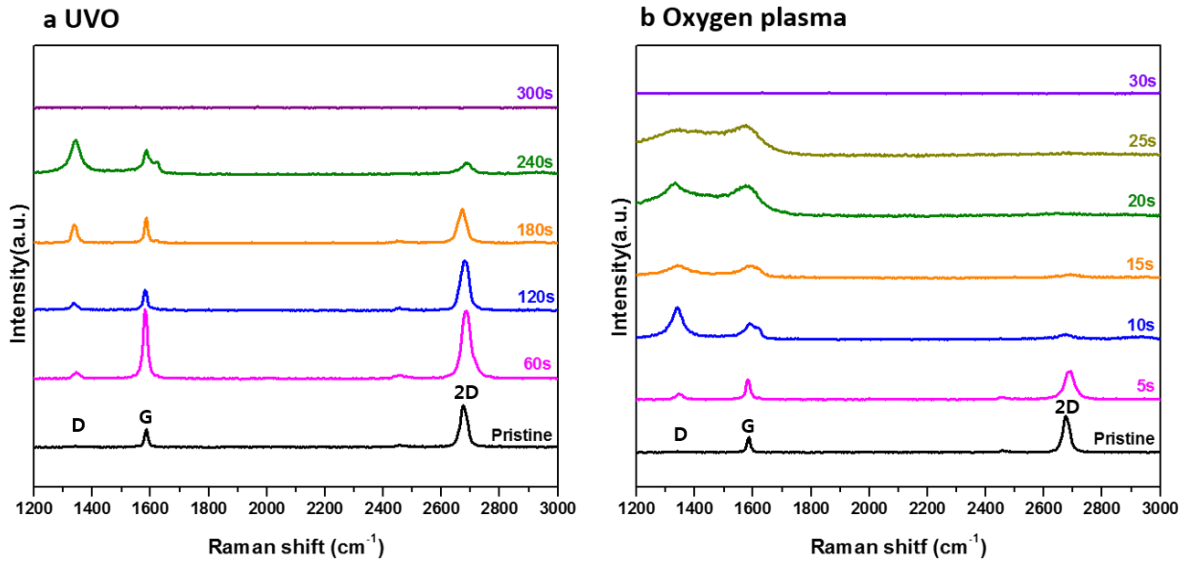

Figure 19. Raman spectra of (a) UV/O-treated and (b) oxygen plasma-treated graphene sheets.

X-ray photoelectron spectroscopy (XPS) was used to evaluate the bonding energies between the oxygen containing functional groups and the graphene surface. The XPS spectra clearly show that the chemical composition of the UV/Ozone-treated and oxygen plasma-treated graphene sheets change with treatment time. In Figure 20a–c, the XPS peak locations differ from those in the spectrum of the pristine graphene sheet. These two cases represent increasing concentrations of oxygen containing functional groups. The deconvoluted area ratio of sp^3 C–C and C–OH to sp^2 C–C from UV/Ozone-treated graphene sheets increases slightly as the treatment time is increased to 120 s, whereas the ratio decreases when the UV/Ozone treatment time exceeds 120 s. However, in the case of the oxygen plasma-treated graphene sheets, the ratio increases with increasing treatment time, as shown in Figure 20d.

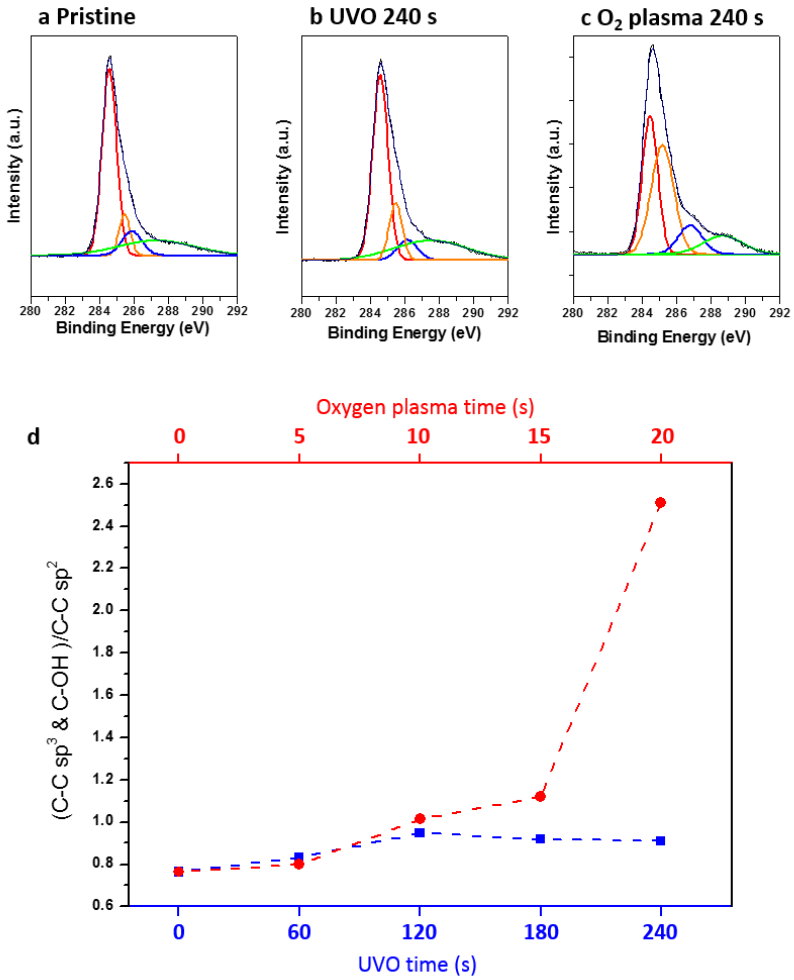

Figure 20. Deconvoluted XPS C1s spectra of (a) a pristine graphene sheet and graphene sheets subjected to (b) UV/Ozone treatment for 240 s and (c) oxygen plasma treatment for 20 s. (d) Deconvoluted area ratio between sp^3 C–C and C–OH and sp^2 C–C from the spectra of UV/Ozone-treated (blue line) and oxygen plasma-treated (red line) graphene sheets, respectively.

5.1.2. Oxygen and hydrogen atom-driven formation of point defects in monolayer graphene sheet

I present results for the three types of point defect mentioned above. The first type is the normal monovacancy as shown from Figure 21 to Figure 31. Generally, atom ejection occurs at random positions, and vacancies initially appear randomly in the area exposed to the electron beam. However, in our conditions, the positions on carbon atoms with three-fold symmetry and the bridging of the C–C bonds in the graphene lattice were these origins. The MV was the most frequently observed defect in our TEM images. With the random transfer of kinetic energy from the ejected electrons to carbon atoms during the experiment, it was natural that the stable structures were found frequently. Therefore, the abundant appearance of MVs in the experiment was consistent with the fact that MVs are the most stable structures among the point defects formed by the electron beam irradiation of OH molecules adsorbed onto a monolayer graphene lattice.

An oxygen atom with a hydrogen atom preferentially adsorbs onto a carbon atom and the bridging of C–C bonds, as described in previous related studies.[165] However, the migration of an individually adsorbed oxygen atom at these positions[166-167] does not have an energy barrier. Therefore, in our conditions, we considered the role of the hydrogen atom in these processes.

Figure 21 1 shows the formation of an MV that originated from hydroxyl in a graphene sheet, from aberration-corrected TEM images. Figure 21a shows a hydroxyl group with a magnified image inset (red box). The brightly contrasted atoms indicate the hydroxyl group, which was adsorbed during the oxidation treatment. The intermediate state observed under electron beam irradiation is shown in Figure 21c. This process is frequently found during observation as shown in Figure 22. Figure 23 show DFT calculations which is in excellent agreement with the experimental images. For intermediate states in Figure 23, we choose the atomic positions based on the real TEM images by assigning carbon atoms to the bright point of the images in Figure 1.

I clarify the structural changes during the formation process of an MV originating from hydroxyl group in TEM images (Figure 21). The MV presented in Figure 21c with the position of the hydroxyl group switched to that of MV. Therefore, it appears that the MV experiences an intermediate state during taking the three images (Figure 21a-c). Hence, the atomic structure captured in Figure 21b should record the intermediate state of this process. However, since the atomic structure recorded in Figure 21b is not observed to previous reports, it is considered to be atomic structures of several metastable intermediate states.

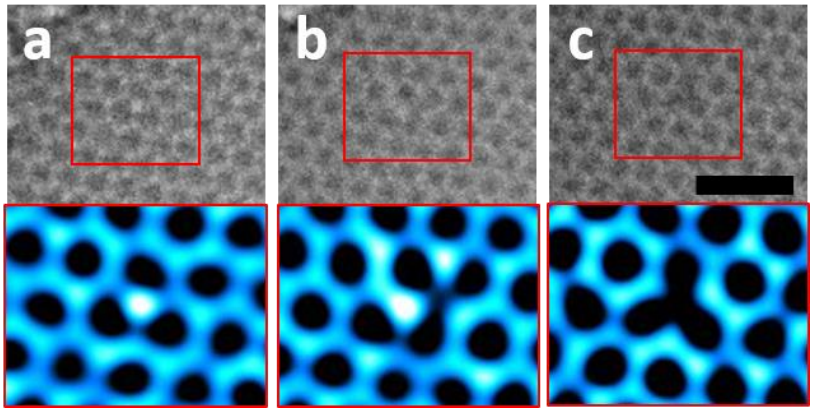

Figure 21. Aberration-corrected TEM images of an MV in the monolayer graphene sheet. (a) and (b) show the OH and an intermediate state of this process with the magnified images in the red rectangular regions. (c) The hydroxyl is ended up transforming MV and the lower. The scale bar is 1 nm.

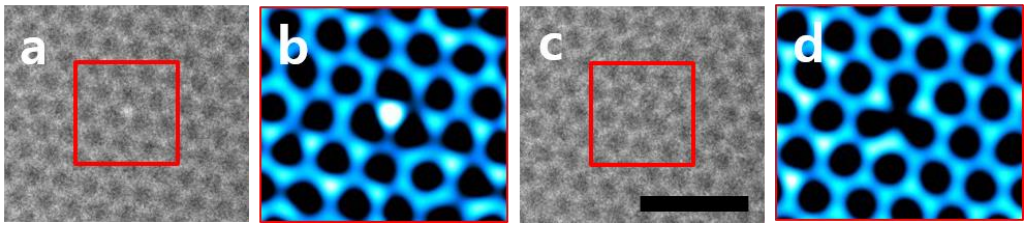

Figure 22. Aberration-corrected TEM images of an MV originated in the monolayer graphene sheet. (a) and (b) show the hydroxyl and MV. The scale bar is 1 nm.

I propose a pathway for the formation of an MV originating from a hydroxyl group. Figure 23 shows a hydroxyl group that is in the same position as in Figure 23a. An OH molecule in the hydroxyl group can be moved to the bridging C–C bonds in the graphene lattice with an energy barrier of 0.72 eV (Figure 23b). In Figure 23c, the OH molecule can be moved again onto an adjacent carbon atom along a zigzag path. In Figure 23d, the OH molecule is able to dissociate into oxygen and hydrogen atoms with an energy barrier of 3.26 eV, and the hydrogen atom binds to another neighboring carbon atom. Given that the evaporation barriers of the C–OH molecules are more than 10 eV, this dissociation process is favorable to the overall process. The hexagonal lattice containing the oxygen and hydrogen atoms can be transformed to an MV by breaking the C–C bonds in the graphene lattice (indicated by the two yellow dashed lines in Figure 23d) while desorbing the C–O atoms (indicated by the yellow "X" in Figure 23e). The energy barrier for breaking the two C–C bonds in Figure 23d was found to be 5.19 eV, and that for simultaneously desorbing the C–O atoms onto carbon atoms in the graphene lattice (indicated by the yellow "X" in Figure 23e) was found to be 6.03 eV. Furthermore, the migration barrier of the carbon atoms (indicated by the yellow arrow in Figure 23f) was found to be 0.69 eV. These energy barriers were too high to be overcame by thermal activation at room temperature; thus, the activation energy for the transition had to be provided by the electron beam of the TEM. After the desorption of the C–O atoms and the migration of the carbon atom, the MV was ultimately formed in the graphene sheet (Figure 23g).

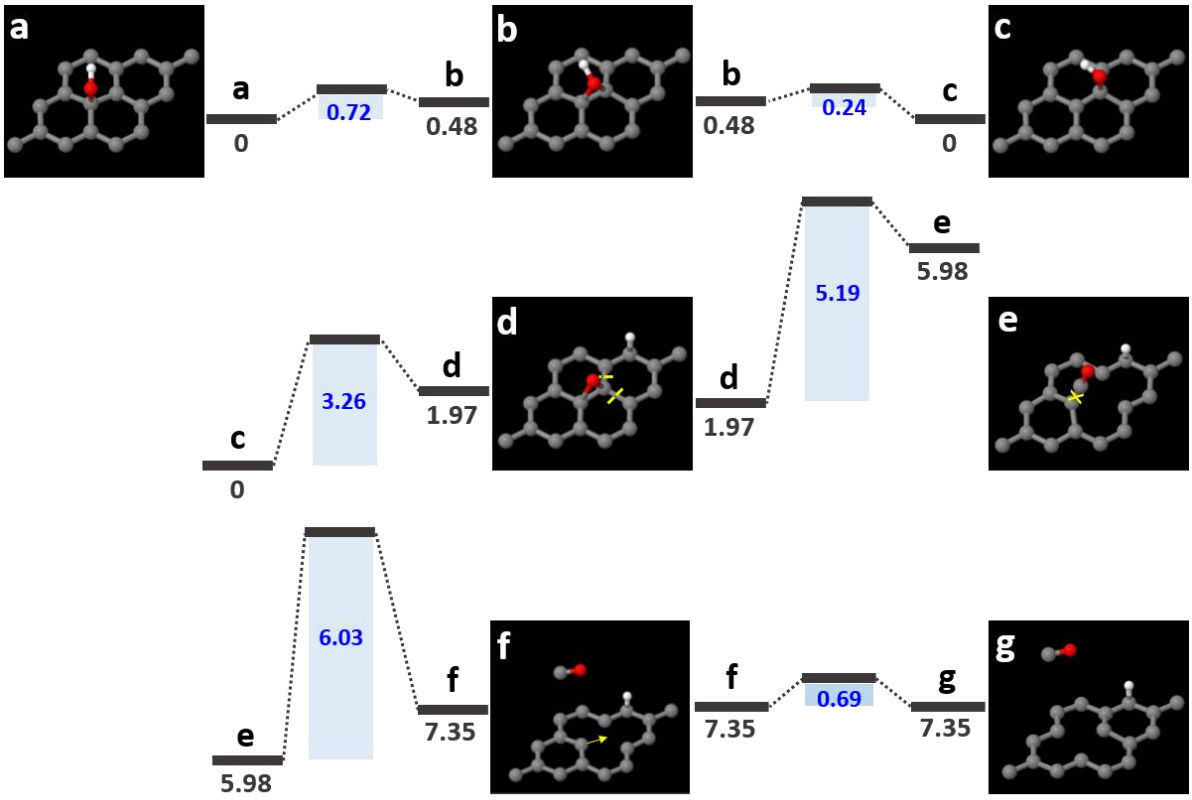

Figure 23. Atomic structures of MV formation originating from a hydroxyl group, along with energy barriers and formation energies for this process: (a) graphene monolayer with a hydroxyl group; (b)–(f) intermediate states of this process; (g) the final state. The red and white balls indicate oxygen and hydrogen atom, respectively. This process can be obtained by breaking the O–H bonding while desorbing C–O atoms from the graphene sheet. The values in blue represent energy barriers, whereas those in dark gray represent formation energies.

If there was no hydrogen involved in the MV formation process, the migration barrier of the oxygen atom in Figure 24b was −0.83 eV. The energy barrier for breaking the C–C bonds in Figure 24b was found to be 5.19 eV, and the energy barrier for simultaneously desorbing the C–O atoms onto carbon atoms in the graphene lattice (indicated by the yellow "X" in Figure 24c) was found to be 6.03 eV. Meanwhile, the migration barrier of the carbon atom (indicated by the yellow arrow in Figure 24d) was found to be 0.69 eV. After the desorption of the C–O atoms and migration of the carbon atom, an MV ultimately formed in the graphene sheet (Figure 24g). Without hydrogen, this pathway is not logical. This is because the energy barrier is negative because the hydroxyl structure cannot be stably maintained (Figure 24a and 24b).

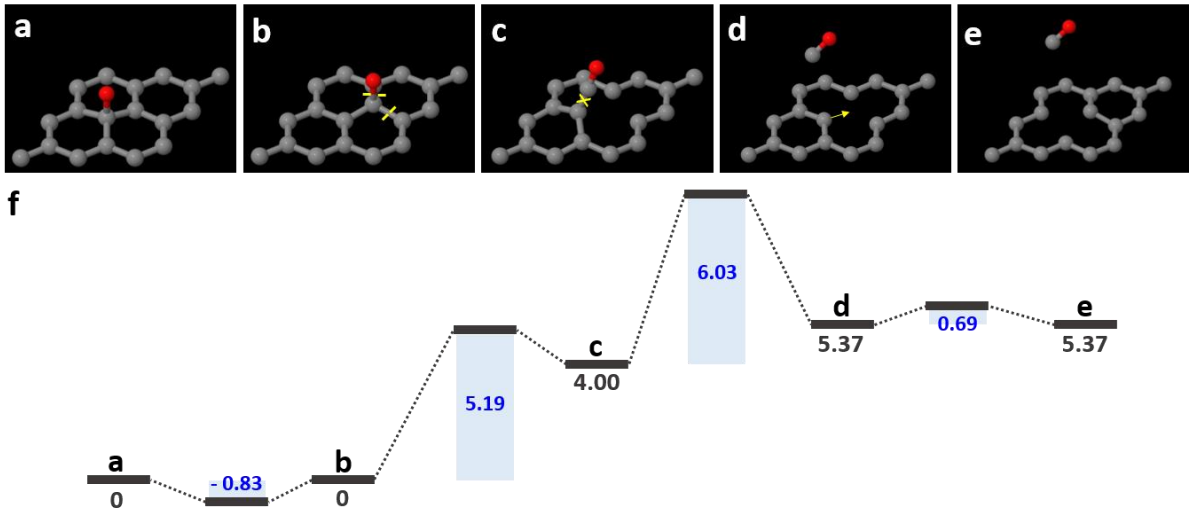

Figure 24. Atomic structures of MV formation originated from a O atom absorbing on top of carbon atom in monolayer graphene sheet and energy barriers for this process and formation energies. (a) shows the oxygen atom absorbing on the sheet. (b)-(d) show the intermediate states of this process. (e) shows formation of MV. (f) Energy barriers and formation energies of this process. This process can be obtained by desorbing C-O atoms from the graphene sheet. Blue energies indicate energy barriers and dark grey energies indicate formation energies.

Figure 25 shows the formation processes of two MVs originating from OH molecules on the bridging of C–C bonds, the state of which is epoxy group with one co-adsorbed hydrogen atom. The two OH molecules are shown in Figure 25a–c. In Figure 25d–e, the upper OH molecule is constructed to form an MV (Figure 25f), and a reconstructed MV (r-MV) is present at the lower OH molecule position. Indeed, an MV can exhibit a Jahn–Teller distortion, thus causing an initial MV to reconstruct into a (5-9) defect. Therefore, an r-MV is easily observed in an MV position. Through electron beam irradiation, the upper molecule is ultimately removed, and an MV forms in the same position; by contrast, the r-MV is healed (Figure 25f). Figure 26 shows our DFT calculations, which are in excellent agreement with the experimental images. For the unstable structures in Figure 26, we chose the atomic positions from the real TEM images by assigning carbon atoms to the bright points in the images of Figure 25.

Here, we clarify the structural changes in the upper molecule position in Figure 25 through continuous electron beam irradiation. The OH molecules presented in Figure 25a–c are transformed to an r-MV and the perfect hexagonal lattice in Figure 25f. The atomic structures in Figure 25d and e show the formation process of the MV. However, because the recorded atomic structures do not match any known form of MV, they are considered a superposition of several metastable intermediate structures.

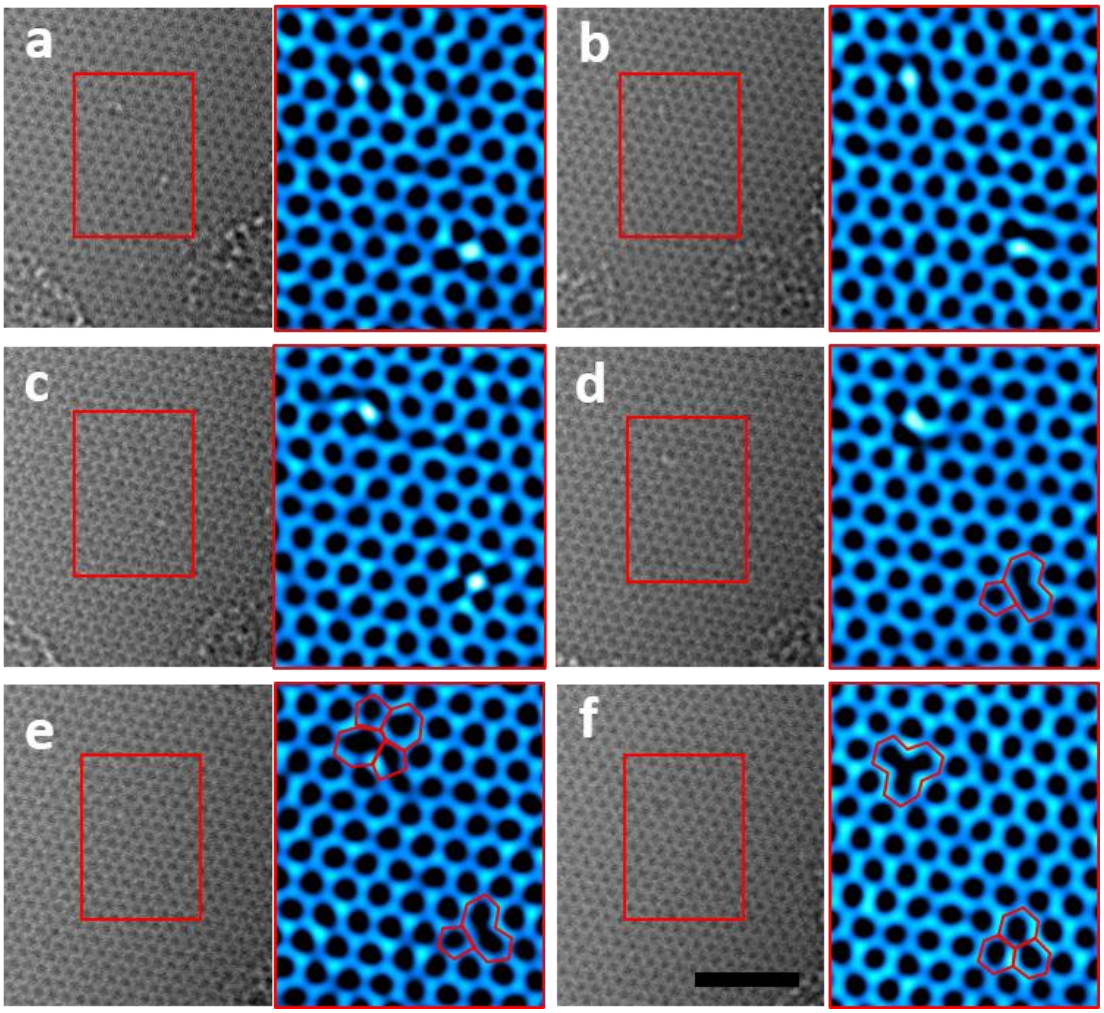

Figure 25. Aberration-corrected TEM images of MVs in the monolayer graphene sheet: (a)–(c) two OH molecules on the bridging of C–C bonds in the graphene lattice, with magnified images of the areas in the red squares; (d) the lower position molecule is transformed into an r-MV; (e) the structure of upper position molecule is reconstructed to a (55-77) defect by SW transformation; (f) the upper position molecule is ultimately transformed to an MV, whereas the lower position molecule heals to the hexagonal graphene lattice. The scale bar is 2 nm.

I propose a pathway for the formation of an MV originating from OH molecules on the bridging of C–C bonds in a graphene sheet. Figure 26a shows the upper position of the molecule in Figure 25. The OH molecule can be moved onto a carbon atom in the graphene lattice with an energy barrier of 0.24 eV (Figure 26b). The hexagonal lattice containing the OH molecule can be transformed into a (55-77) defect by the Stone-Wales (SW) transformation of carbon dimers (dashed yellow box in Figure 26b). The rotational barrier for this process was found to be 6.78 eV in our DFT calculations.

Figure 26c and d show the dissociation of the OH molecule, and its energy barrier was found to be 3.26 eV. The energy barrier for breaking two C–C bonds (indicated by the two dashed yellow lines in Figure 26d) was found to be 5.73 eV. Meanwhile, the energy barrier for simultaneously desorbing C–O atoms onto the carbon atoms in a graphene lattice (indicated by the yellow "X" in the side view of Figure 26e) was found to be 6.76 eV. The structural change of the defect in Figure 26e to an MV becomes possible through the 90° rotation (SW transformation) of the dimer indicated by the dashed yellow box in Figure 26f. The energy barrier for this process was calculated to be 1.55 eV. The position adsorbing the OH molecule is reconstructed into the (55-77) defect by the SW transformation (Figure 26a–c). After simultaneously desorbing the C–O atoms (Figure 26e and f), the defect is once again reconstructed into an MV by the SW transformation (Figure 26g).

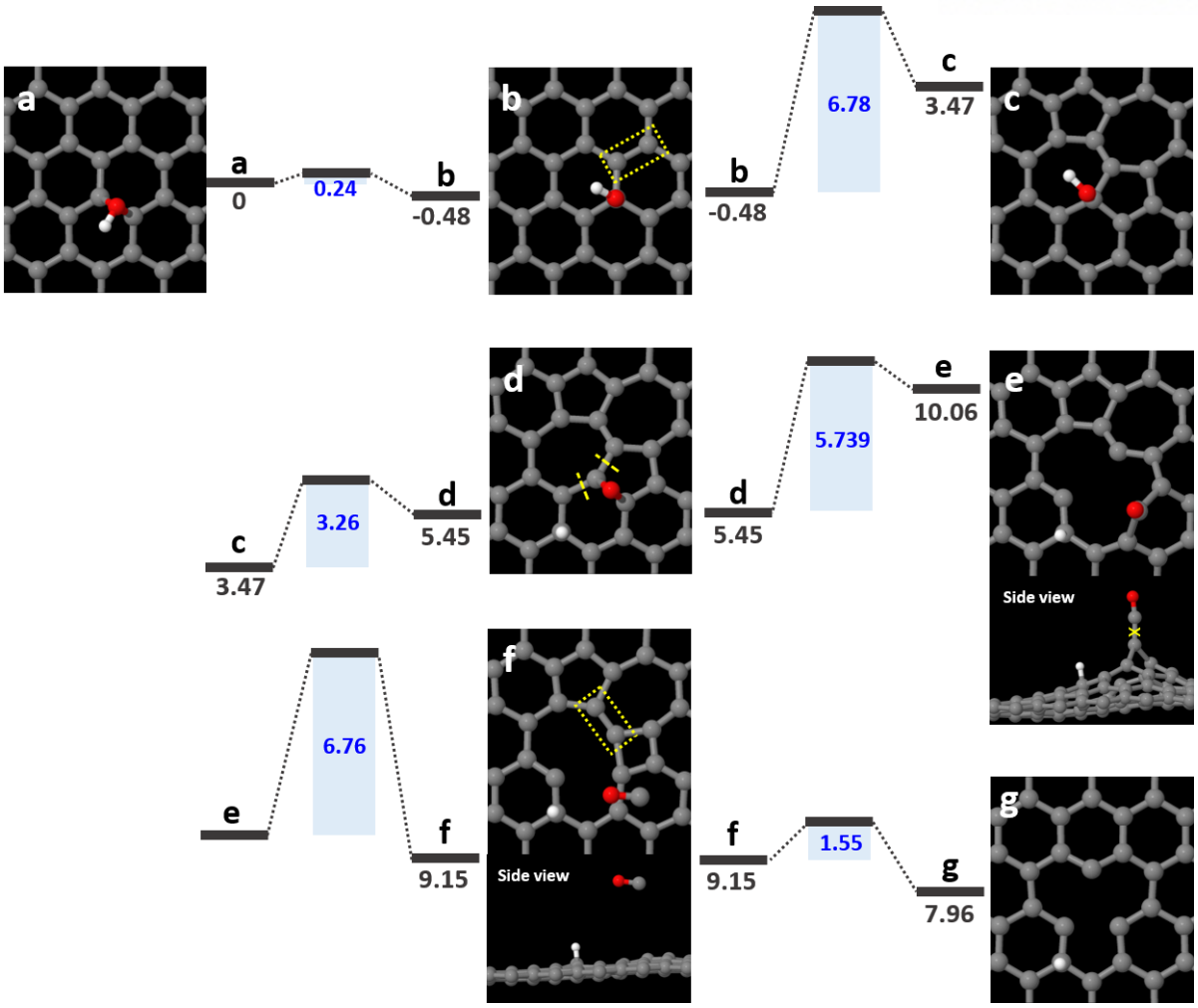

Figure 26. Atomic structures of the MV formation along with energy barriers and formation energies for this process: (a) OH molecule on bridging of C–C bonds in graphene lattice; (b)–(e) intermediate states of the MV formation process; (f) a formed MV. This process can be obtained by the SW transformation of carbon dimers (indicated by the dashed yellow boxes) and the desorption of C–O atoms from the graphene sheet.

Figure 27 shows the MV formation process without the hydrogen atom in Figure 25. The oxygen atom in the epoxy group can be moved onto a carbon atom in the graphene lattice with no energy barrier (Figure 27b). The hexagonal lattice containing the oxygen atom can be transformed into (55-77) defects by the SW transformation of the carbon dimers indicated by the dashed yellow box in Figure 27b. The rotational barrier for this process was found to be 5.20 eV in our DFT calculations. Figure 27c and d show the breaking of two C–C atoms (indicated by the two dashed yellow lines in Figure 26c), and the energy barrier was found to be 5.73 eV. The energy barrier associated with the simultaneous desorption of C–O atoms onto carbon atoms in a graphene lattice (indicated by the yellow "X" in the side view of Fig. S3e) was found to be 6.76 eV. The structural change of the (55-77) defect to an MV becomes possible by the 90° rotation (SW transformation) of the dimer indicated by the dashed yellow box in Fig. S3e. The energy barrier for this process was calculated to be 1.55 eV. The epoxy group was reconstructed into the (55-77) defect by the SW transformation (Figure 27a–c). After desorbing the C–O atoms, the defect was reconstructed into an MV by the SW transformation (Figure 27f). However, this whole process is unfavorable compared with the previous case, which contained a hydrogen atom, because of the absence of hydrogen, the hydroxyl structure cannot be stably maintained.[45, 47]

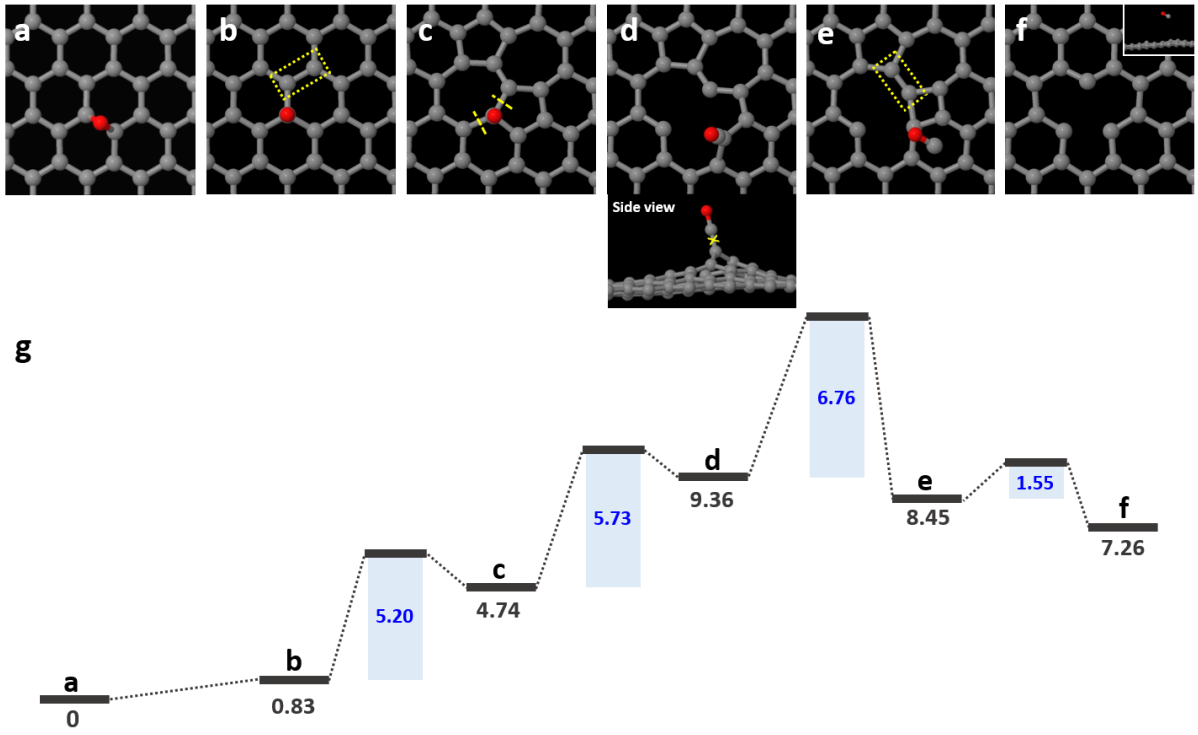

Figure 27. Atomic structures of the MV formation, along with energy barriers and formation energies for this process. (a) Epoxy group; (b)–(e) intermediate states of the MV formation process; (f) MV originating from the epoxy group; (g) energy barriers and formation energies. This process can be obtained by the SW transformation of carbon dimers (indicated by the dashed yellow boxes) and the desorption of C–O atoms from the graphene sheet.

Second type is divacancy (DV). We analyzed a DV induced by OH molecules. Generally, divacancy is formed when two neighboring carbon atoms missed, the lowest energy state of which when this occurs in the same atomic layer. But, it is possible to forming directly divacancy by OH molecule on a MV in graphene lattice. And, based on our experimental results such as Figure 21-27, hydrogen atoms should be considered.

Figure 28 show formation of DV in monolayer graphene sheet. Figure 28a shows a TEM image, which agrees with the simulated image in Figure 29a. Figure 28b and c show a DV, which is very distinctive and clearly different from the MV. We propose a pathway for the formation of DV originated from OH molecule on MV in graphene sheet: An example of the formation is shown in Figure 29. Starting from an initial MV with an OH molecule (Figure 29a), the OH molecule initially splits into a hydrogen atom and an oxygen atom with (Figure 29b) and this energy barrier is found to 2.20 eV. Hydrogen atom is moved on a carbon atom positioned right zigzag direction along the yellow arrow in Figure 29b and this energy barrier is found to 1.73eV. By moving a carbon atom along the yellow arrow in Figure c with 2.95 eV of this energy barrier, the MV is subsequently migrated further (Figure 29d). After breaking bonding between C-O atoms and carbon atom positioned right zigzag direction (Figure 29e), the MV that in turn reconfigure into a divacancy (Figure 29e) and this energy barrier is found to 3.51 eV. When the C-O atoms finally are desorbed at the same time (Figure 29f), the DV clearly is shown. This desorption barrier is found to 7.05 eV. This DV is able to easily reconstruct with neighboring carbon atoms due to the Jahn-Teller distortion.

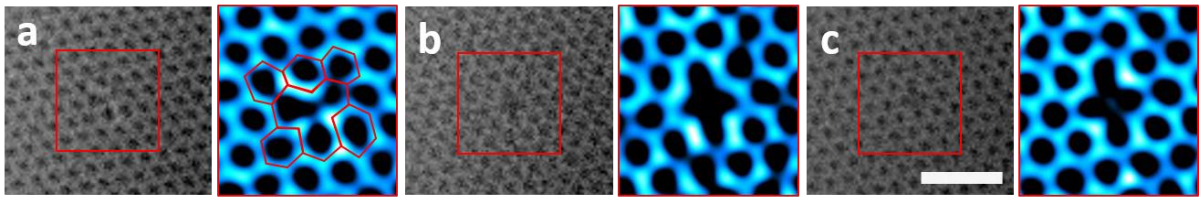

Figure 28. Aberration-corrected TEM images of a DV in the monolayer graphene sheet: (a) The adsorption of an OH molecule on an MV indicates an intermediate state of this process, with magnified images of the areas in the red squares; (b) and (c) show the formation of a DV. The scale bar is 1 nm.

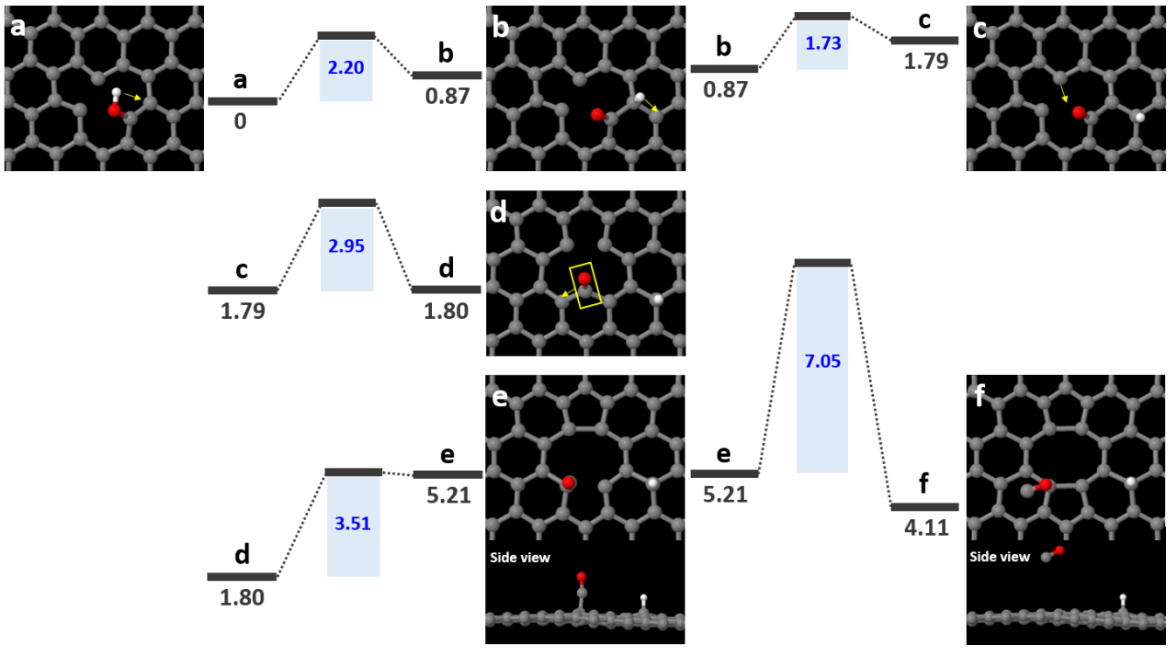

Figure 29. Atomic structures of the DV formation, along with energy barriers and formation energies for this process: (a) the OH molecule on an MV in the graphene lattice; (b)–(d) intermediate states of the DV formation process; (e) and (f) formed (reconstructed) DV; (g) energy barriers and formation energies.

The last type of defect is the new point defect (Figure 30). This type is very similar to a nitrogen-mediated MV [168] or a saddle point[1] for motion of the MV. The defect originates from an OH molecule on the bridging of C–C bonds, such as an epoxide group with one co-adsorbed hydrogen atom, which has an intermediate state (Figure 30a and b). As shown in Figure 30c and d, a new MV such as a pair of 13-5 rings is observed. This pair of 13-5 rings is quite stable for a few seconds. Indeed, the same structure, consisting of only a single carbon atom, is very unstable because it is one of the migration paths on which an MV can move to a neighboring atomic site. However, in the case involving hydrogen atoms, this can be stable under electron beam irradiation. The hydrogen atoms involved in the new point defect make the new MV stable. It follows that the participating atoms should also stabilize a higher-order numbered vacancy and pentavacancy such as the pair of 13-5 rings.

Figure 31 show how this process enables new MV to form and stabilize into the structure observed in Figure 30. Figure 8a-i present a pathway, where desorption of C-O atoms and addition of a second hydrogen atom are accompanied to form the observed structure. An OH molecule is moved on top of carbon atom positioned along the yellow arrow in Figure 8a and b with energy barrier of 0.25 eV. The OH molecule is dissociated with a hydrogen atom and an oxygen atom (Figure 31c) and then the hydrogen atom binds to a carbon atom positioned along the yellow arrow in Figure 8c (Figure 8d). These energy barriers are found to 2.57 eV and 2.12 eV. The energy barrier of breaking two C-C bonds indicated by two dashed yellow lines in Figure 8d is found to be 5.20 eV and the energy barrier of a desorbing C-O atoms at once indicated by yellow box in Figure be is found to be 6.03 eV. After desorbing the C-O atoms, r-MV is formed by Jahn-Teller distortion with 0.01 eV of energy barrier (Figure 31f). And, the hydrogen atom is moved onto carbon atom along yellow arrow in Figure 8f (Figure 31h). The MV, which indicates a r-MV in Figure 31i, is migrated by moving a carbon atom along yellow arrow in Figure 31i (Figure 31j) and this energy barrier is found to 0.08 eV. By adding second hydrogen atom in Figure 31k, a r-MV maintains MV structure, however, this energy barrier is increased to 1.73 eV. Following breaking a C-C bond indicated by dashed yellow line in Figure 31k, the final structure is formed, and this resembles to nitrogen-mediated monovacancies48 or a saddle point1 for motion of the MV.

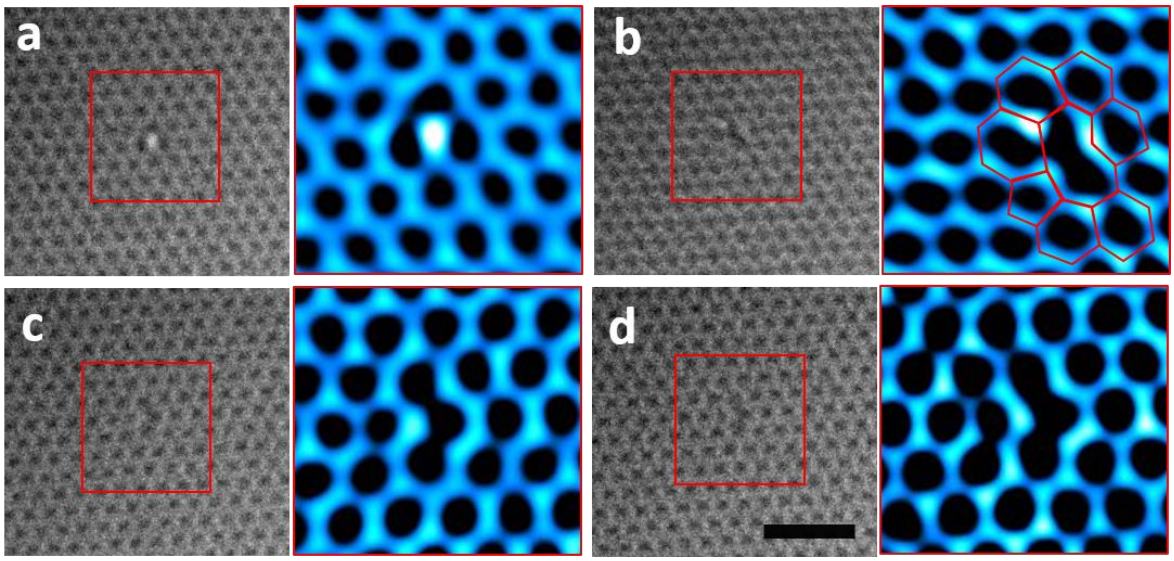

Figure 30. Aberration-corrected TEM images of a new MV in the monolayer graphene sheet: (a) OH molecule on the bridging of C–C bonds in the graphene lattice, with magnified images of the areas in the red squares; (b) intermediate state of this process; (c) and (d) new MV in the same position. (d) The red outline shows 5-13 ring defect. The scale bar is 1 nm.

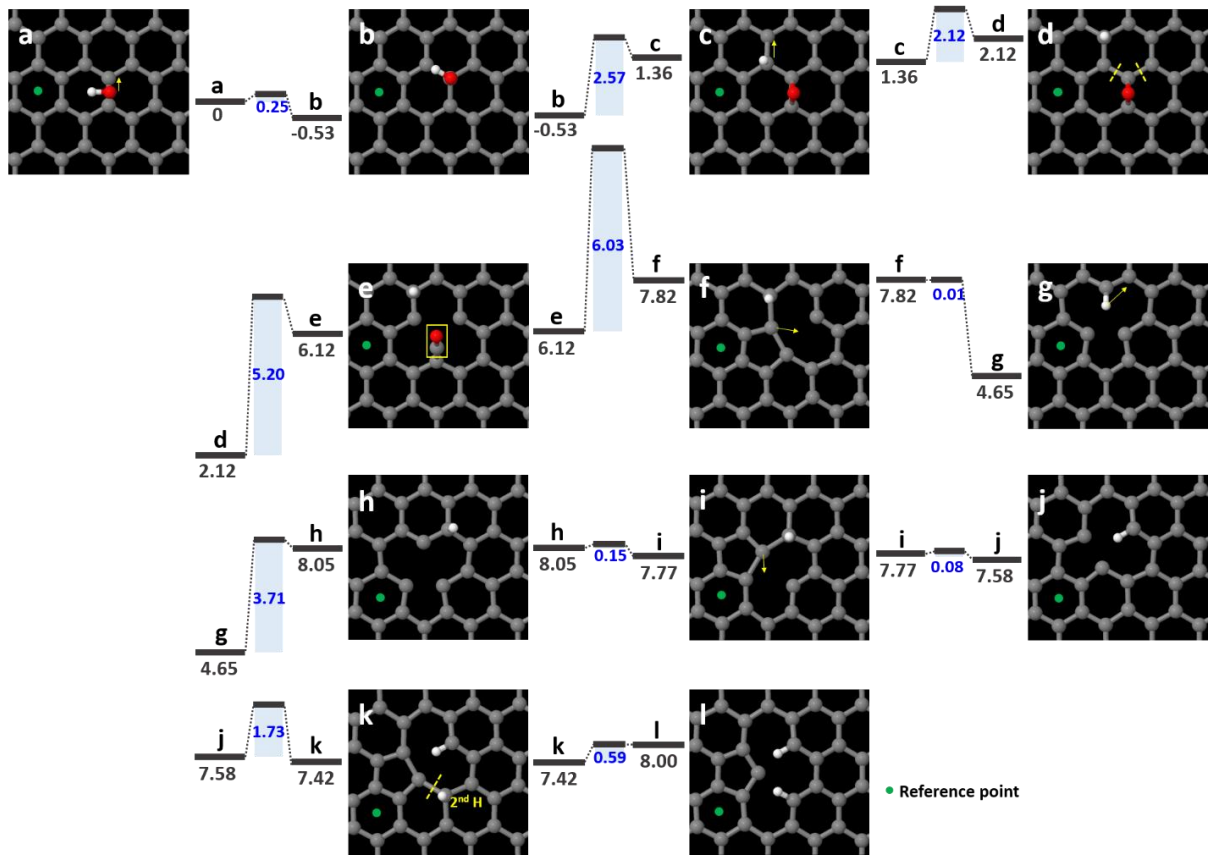

Figure 31. Atomic structures of a new MV formation, along with energy barriers and formation energies for this process: (a) OH molecule on the bridging of C–C bonds in the graphene lattice; (b)–(k) intermediate states of the new MV formation process; (m) energy barriers and formation energies.

I emphasize that in all of the above observations, the point defects were the results of the combination of an oxidation process and the electron beam irradiation on the surface adsorbing the oxygen and hydrogen atoms. Furthermore, these defects were stable, at least for the typical time required to record an image sequence, i.e., several seconds. The same types of defects were found in other research under electron beam and ion irradiation, but those in our investigation had a different formation mechanism. In any case, our atomic resolution imaging and DFT calculation results confirmed the substantial effect of oxygen and hydrogen atoms on the formation of point defects. We first propose a real-time process, in which oxygen atoms were adsorbed directly onto carbon atoms, and MVs were indeed formed in the graphene sheets. Among them, the presence of hydrogen atoms not only lowered the energy barriers required for the formation of MVs but also stabilized the new MV structure. This may have directly or indirectly indicated that hydrogen atoms were present in the TEM images.

5.2. Hexagonal Boron Nitride

5.2.1. Atomic-scale dynamics of triangular hole growth in monolayer hBN under electron beam irradiation

To elucidate the mechanism of hole growth in hBN monolayers, the dynamics of triangular holes induced by electron beam irradiation were analyzed using ARTEM. A large area monolayer of hBN at atomic resolution is shown in Figure 32 and 33. Figure 10c shows intensity profiles of atoms in a raw image of Figure 32a taken by an aberration-corrected TEM with a monochromator and simulation image at the imaging condition in Figure 32b. The B and N atoms can be distinguished as the N atoms display a 3.5% higher intensity than the B atoms with a ±2% deviation in real image. Since previous theoretical and experimental studies reported that triangular holes in hBN formed by electron beam irradiation have N terminated edges,[69, 104] the alternation of intensity measured from the edge atoms has a good agreement with the positions of the B and N atom as shown in Figure 32d. To prove the intensity of real image, simulation was performed at the imaging condition using MacTempasX. Figure 32c shows the agreement between experimental and simulational intensity profiles. This result indicates that the distinction of B and N atoms is possible from one aberration-corrected TEM image. Indeed, such optimized imaging conditions were used to acquire the results described below.

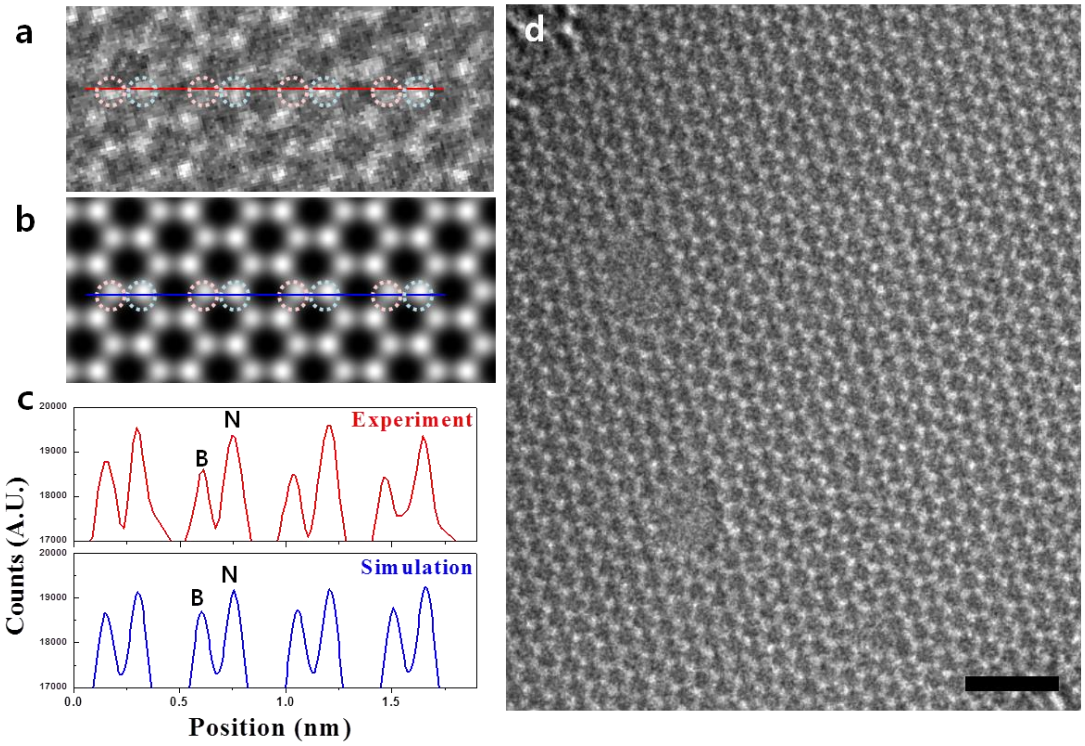

Figure 32. (a) Raw image taken by an ARTEM and (b) simulation image at the imaging condition. (c) Intensity profiles from the trace in (a) and (b). (d) A TEM image showing series of triangular holes in hBN. The scale bar is 1 nm.

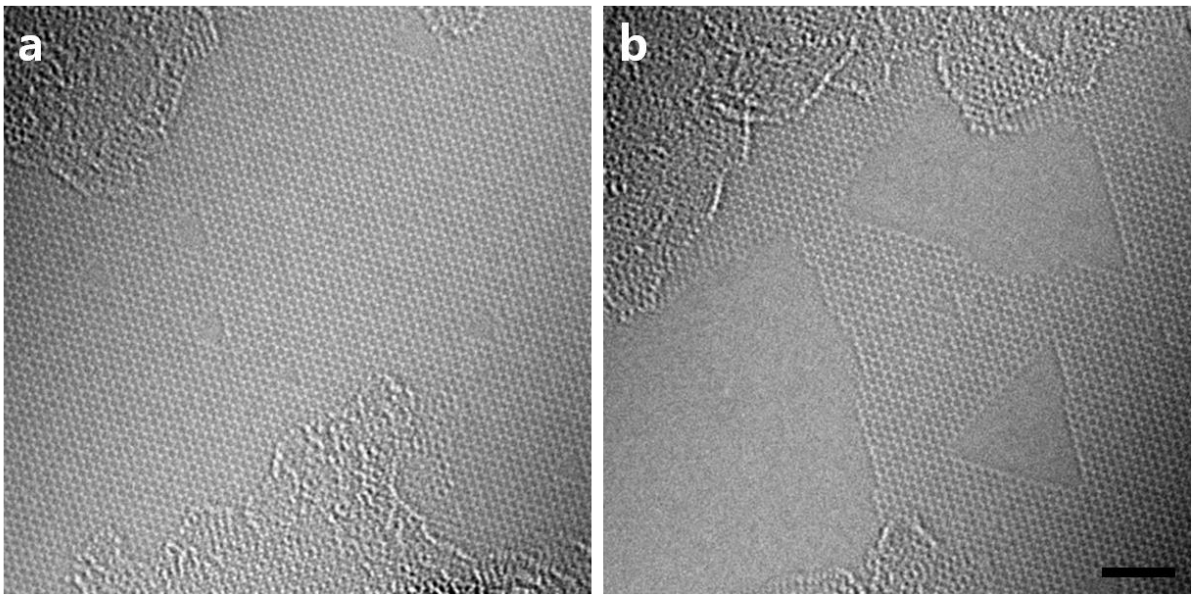

Figure 33. Formation and growth of large triangular holes in monolayer hBN by electron beam irradiation. The TEM images show (a) the initial defects and (b) an enlarged area of the same region. The scale bar is 2 nm.

The hBN hole growth process was subsequently investigated as shown in Figure 34. A vacancy labeled V_B, which refers to the site of a missing B atom, is shown in Figure 34a. Through continuous electron beam irradiation, B and N atoms were removed from sites adjacent to V_B in a manner that maintained an overall triangular shape, although some trapezoidal intermediates were observed. For example, while the removal of a pair of B and N atoms adjacent to the V_B (i.e., $V_{B\text{-}BN}$) resulted in the formation of a trapezoidal site, a triangular hole reformed upon the subsequent loss of an additional B atom (e.g., $V_{B\text{-}BN\text{-}B}$), as shown in Figure 34c. This process continued as the hole grew and involved the temporary introduction of an atom within the growing hole.

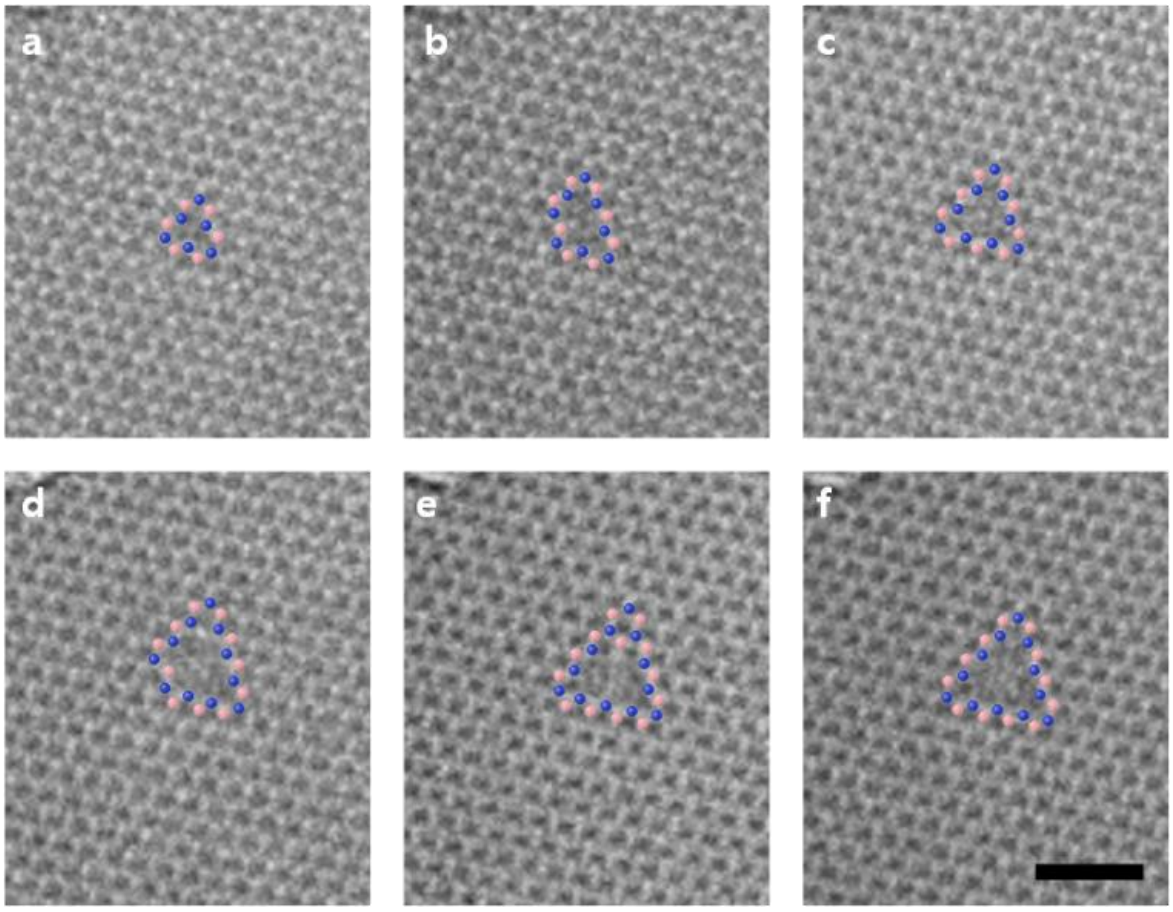

Figure 34. The sequential hole growth process from a vacancy in monolayer hBN at atomic resolution: The process starts (a) with the development of a B vacancy (VB) and grows as shown in (b) to (f). The blue and red dots reflect the N and B atoms, respectively. The scale bar is 1 nm.

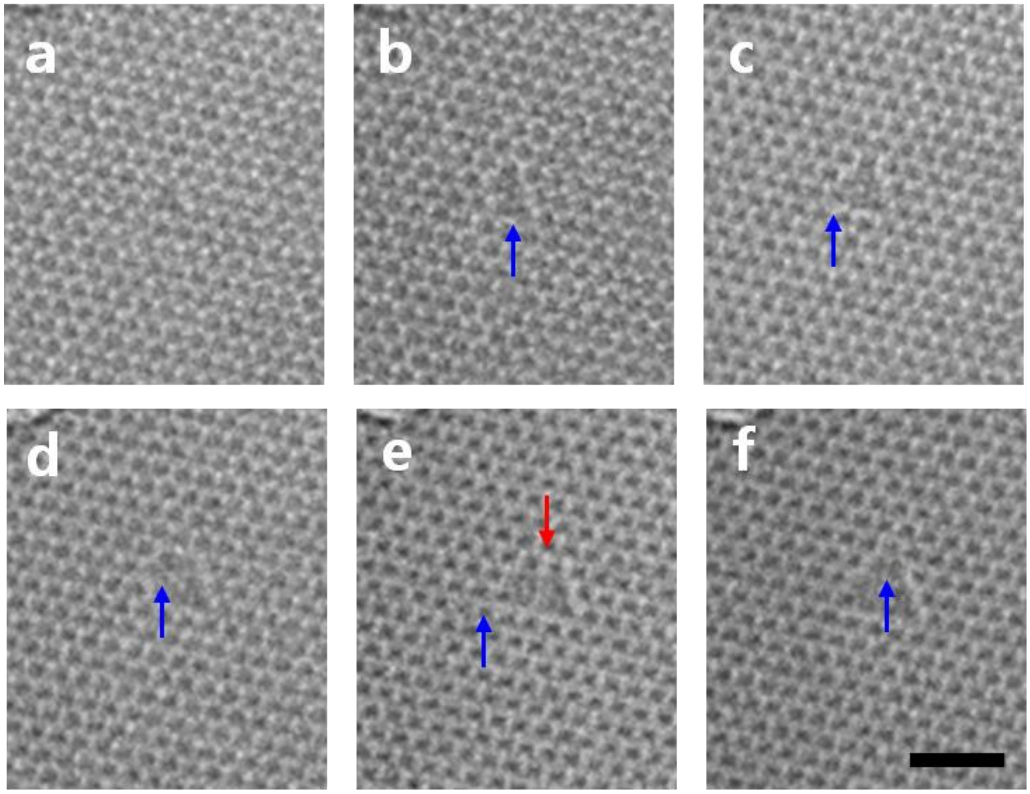

Figure 35. Raw atomic scale images of the growth of a triangular hole found in monolayer hBN. Blue arrows indicate the removal of atoms while the red arrow points to an area where atoms have been added. The scale bar is 1 nm.

Efforts were then directed towards assessing whether the holes maintained their triangular shape after prolonged periods of electron beam irradiation. As summarized in Figure 36, the growth of a triangular hole appeared to be initiated by the removal of B and N atoms near the centers of the hole edges. This experimental observation was supported by energy calculations, which indicated that triangular holes featuring edges with missing B and/or N atoms are more stable than those with atoms missing near a vertex (see Figure 37). Regardless, under prolonged electron beam irradiation, the B and N atoms next to the vacancies were subsequently ejected in a manner that ultimately restored the overall triangular shape of the hole. As shown in Figure 38, the triangular shape of the holes was maintained even after two holes merged together. Additionally, exposure of an edge region to electron beam irradiation resulted in the formation of triangular holes as shown in Figure 39. Once electron beam irradiates within or at edge of a hBN sheet, a N terminated triangular hole is unconditionally formed and its shape is maintained during the hole growth process.

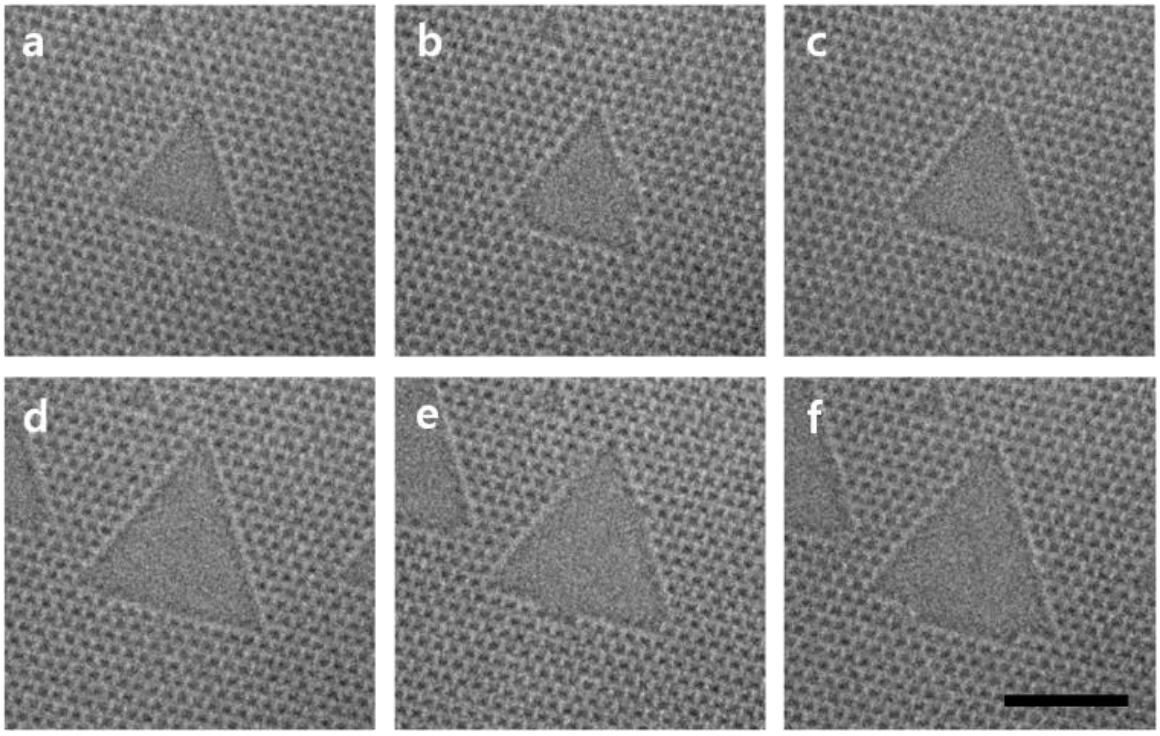

Figure 36. Sequential atomic resolution images of monolayer hBN showing how the shape and orientation of the holes are maintained upon further growth. The scale bar is 2 nm.

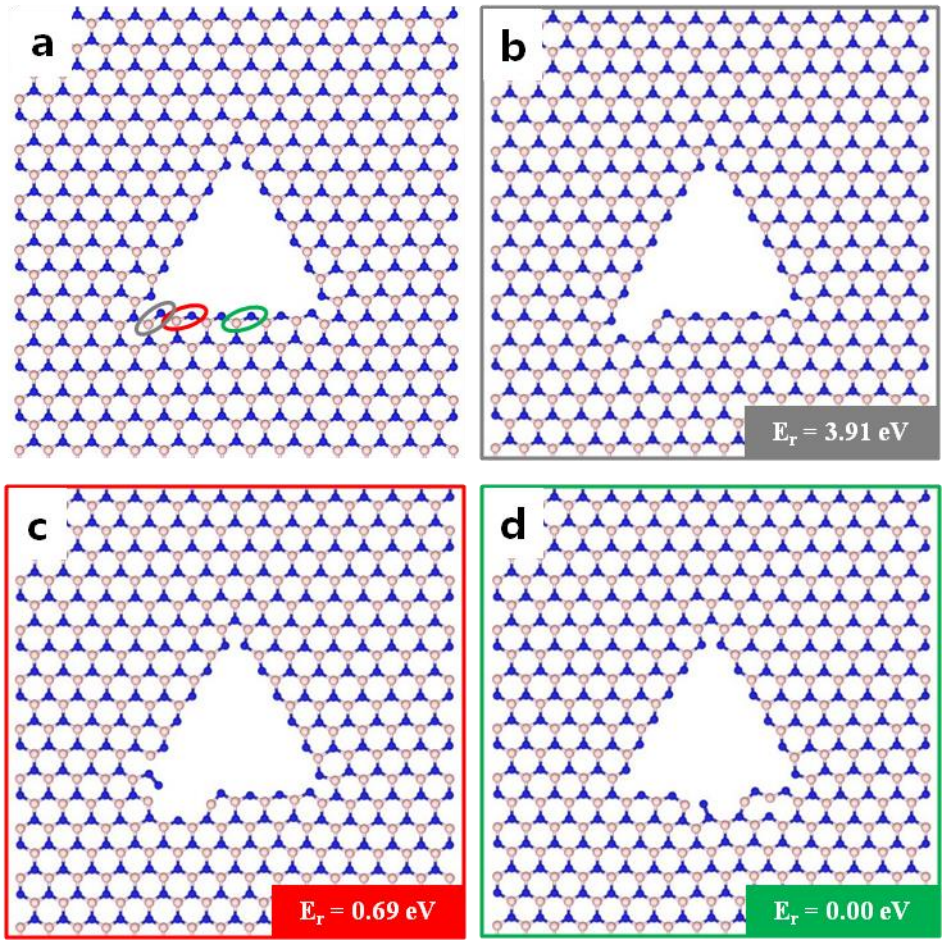

Figure 37. (a) Models for paired B–N atoms missing at an edge of a triangular hole defect in a monolayer hBN sheet with their relative energies: (b) at a corner; (c) near the corner; and (d) near the middle region of a defect edge. Paired B–N atoms missing near the middle of an edge appear to be more stable than those missing at a corner or near a corner.

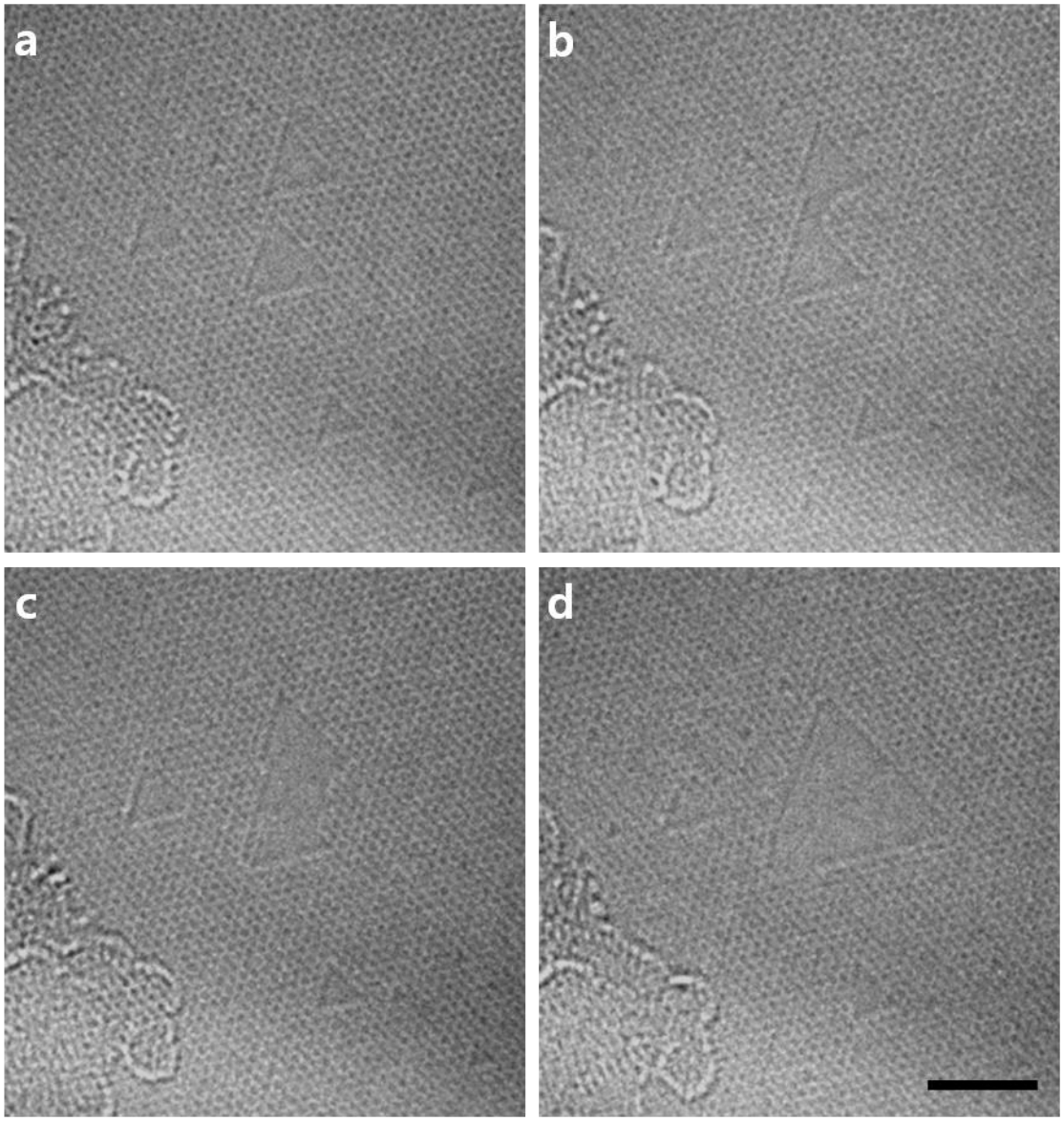

Figure 38. A series of sequential atomic resolution images of monolayer hBN showing how the merging of two holes ultimately maintains a triangular shape. The scale bar is 2 nm.

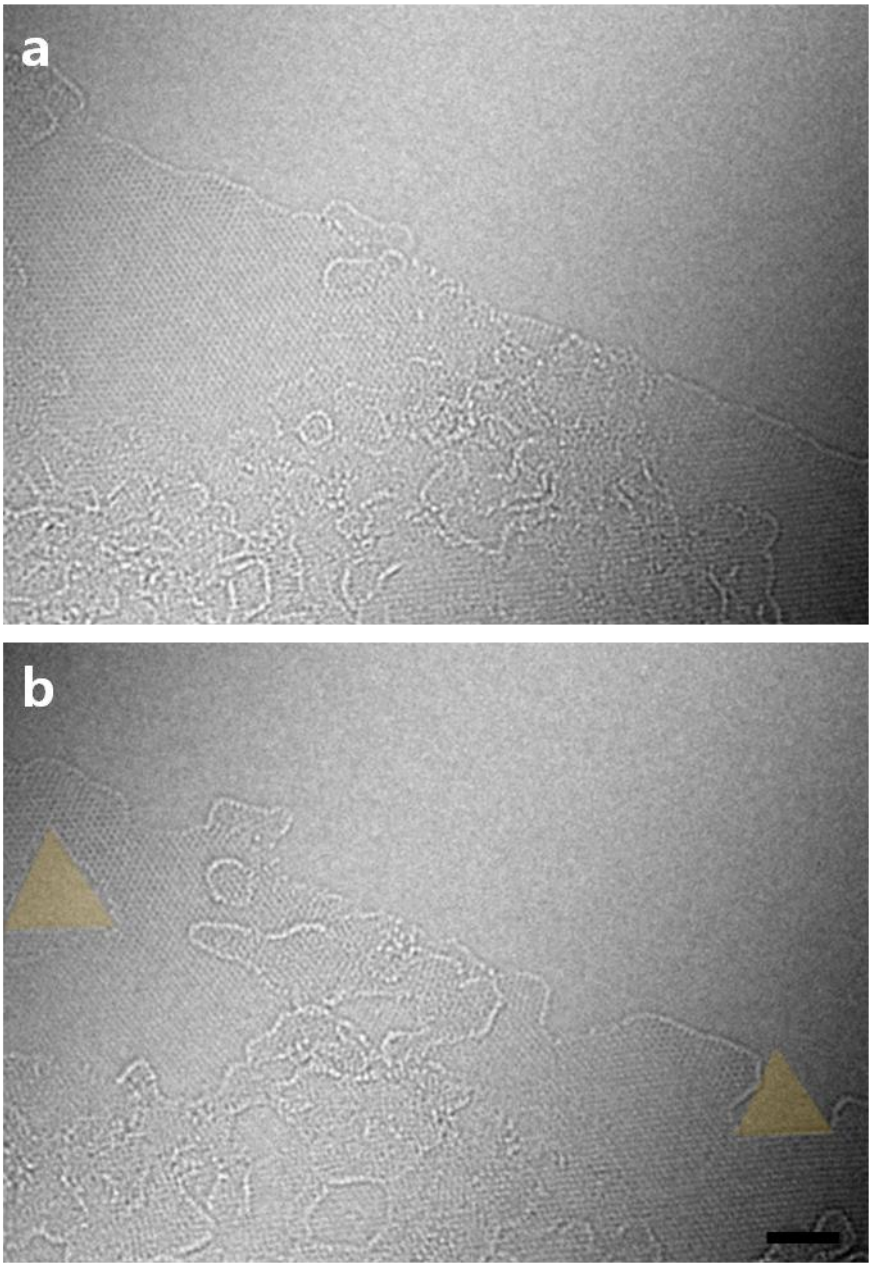

Figure 39. Triangular hole formation on a random edge found in a monolayer of hBN. The images represent (a) an edge followed by (b) the formation of structures with N terminated edges after electron beam irradiation. The scale bar is 2 nm.

During these studies, it was noted that B and N atoms were often ejected as bundles as opposed to individual atoms, at least under the experimental conditions used. For example, as shown in Figure 40a and b, bundles of B and N atoms were removed between successive imaging time intervals (~0.5 sec). Since atom movement is faster than 0.5 sec, DFT calculations and MD simulations were performed to gain additional insight into this process. A summary of the calculated bond lengths between various atoms in and near a triangular hole in hBN is shown in Figure 41.

Note that the calculated B–N bond lengths measured perpendicular to the hole edge were longer than those found along the hole edge (c.f., positions indicated by 6, 7 and 8 vs. positions indicated by 3, 4 and 5). Moreover, the difference in the calculated B–N bond lengths was found to be consistent regardless of the hole size. Hence, when a B and/or N atom is ejected, the B–N bonds perpendicular to the edge become weakened and thus are more likely to be broken upon further electron beam irradiation. The results derived from the DFT calculations were supported by MD simulations. As shown in Figure 41b, the breaking of a B–N bond perpendicular to a hole edge generated a chain of B and N atoms as indicated by the yellow dotted box. The chain then became detached and was subsequently knocked off as a bundle of atoms, as indicated by the green dotted box.

Direct evidence of single chain formation, as supported by DFT calculations and MD simulations, was observed by ARTEM in Figure 41c-f. Electron beam irradiation of the triangular hole (Figure 41c) resulted in the formation of a single chain comprised of B and N atoms (Figure 41d). The chain detachment process appeared to originate from the breaking of a B–N bond perpendicular to a hole edge. The chain was found to fluctuate in position (Figure 41e) before being finally knocked off (Figure 4f). Based on these observations, B and N atoms do not appear to be ejected individually; rather, B–N bonds perpendicular to a triangular hole edge may break first, resulting in the formation of a single chain of atoms that is ultimately removed. Compared to the B and N atoms found within the lattice of hBN, single chains containing the two heteroatoms are relatively unstable and, under the experimental conditions used here, are readily removed.

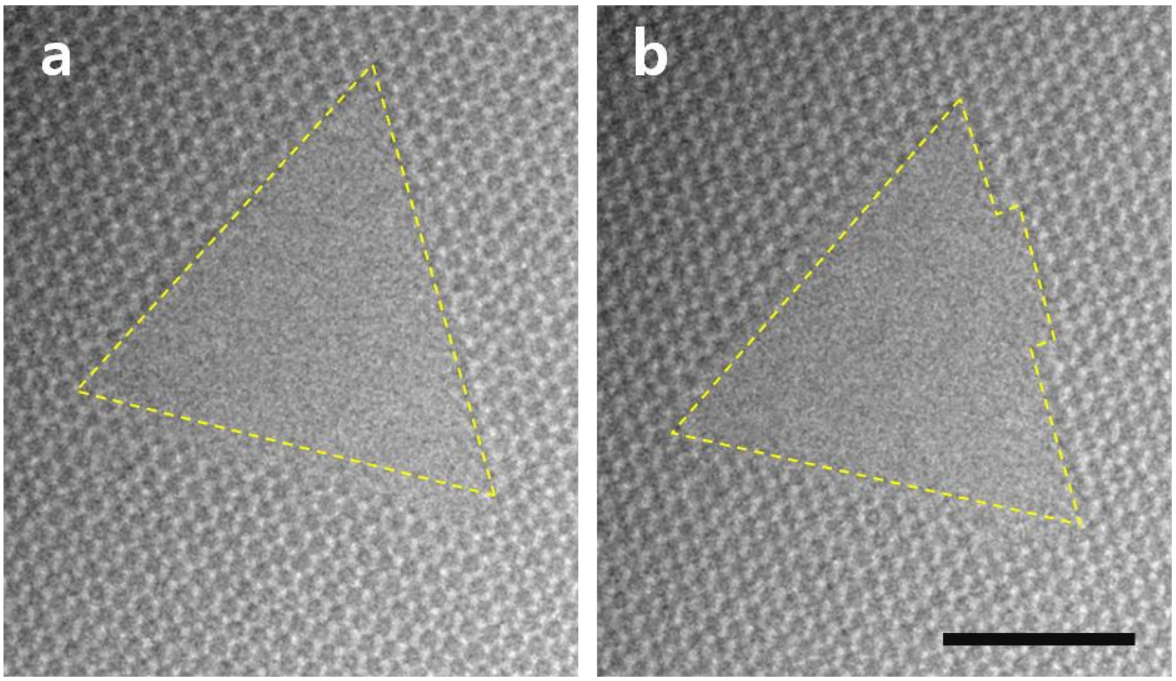

Figure 40. Growth of a triangular hole. Comparing the TEM images shown in (a) and (b) reveals that bundles of B and N atoms are removed at a defect edge within the acquisition time of one frame (0.5 sec). The scale bar is 2 nm.

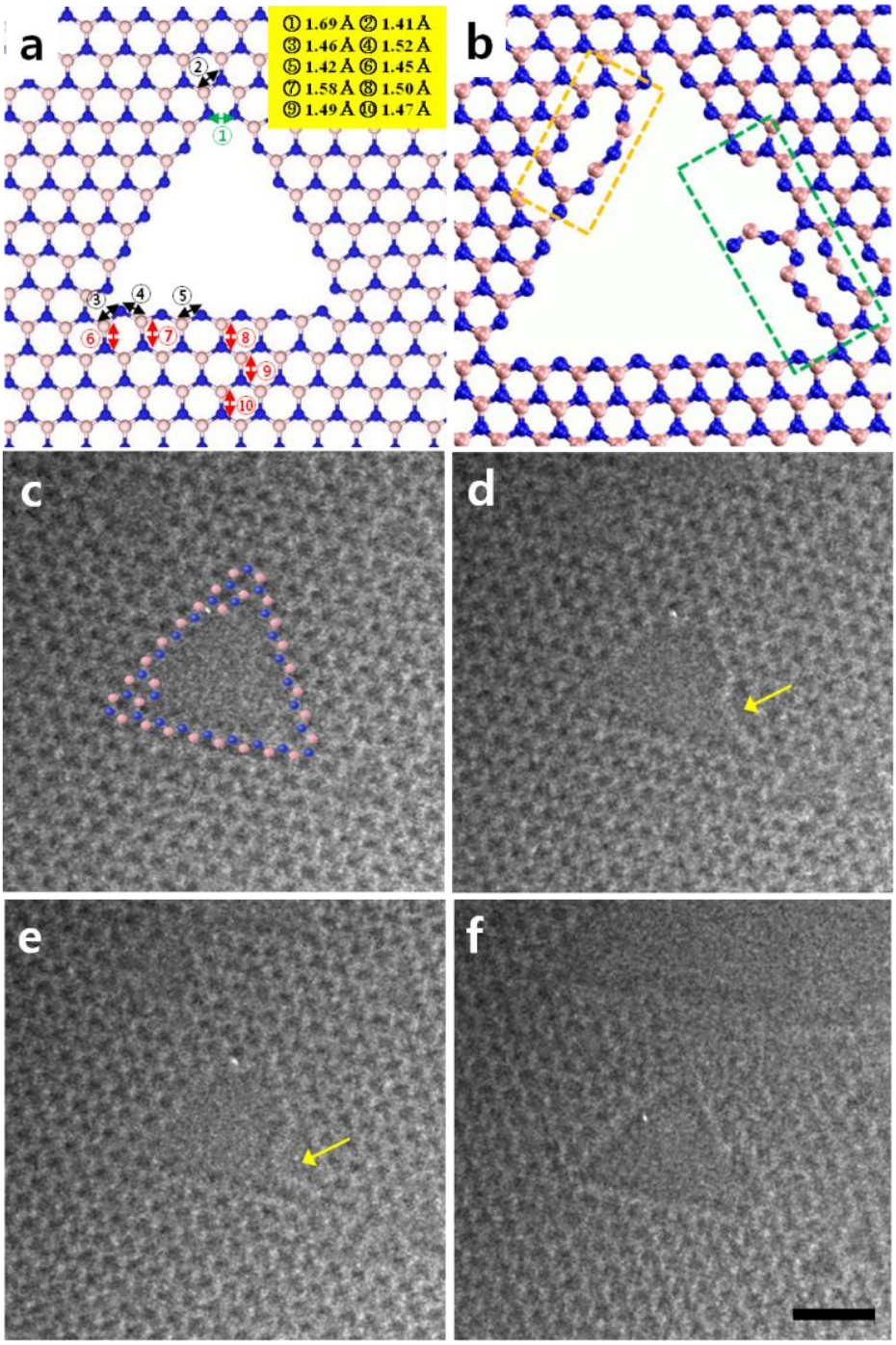

Figure 41. A summary of DFT calculations and MD simulations of hole growth processes in monolayers of hBN. The blue dots represent N atoms whereas the red dots represent B atoms. (a) Calculated bond lengths between various atoms in a triangular hole. (b) The B–N bonds perpendicular to the hole edge are broken first and often bundles of atoms are then knocked off. (c) - (f) A series of TEM images taken over time. The images show the formation of a single chain followed by its fluctuation in position and ultimate removal. The scale bar is 1 nm.

To gain additional insight into the properties of single chains comprised of B and N atoms, efforts were directed toward determining whether single chains were formed during the merging of multiple holes. A series of consecutive TEM images that captured the merging of two holes is shown in Figure 42. In general, such processes are too fast to be captured by TEM, as atoms are often ejected and/or are repositioned faster than the time elapsed between images; however, adsorbates can pin the hole and thus facilitate the capture of an intermediate state. As shown in Figure 42d, the merging of two holes resulted in a temporal bright contrast line, which may be due to the local fluctuation of the corresponding hBN edges and/or an accelerated ejection rate. Subsequent spreading of the fluctuating region resulted in the formation of single chains of B and N atoms inside the hole (Figure 42f) followed by the development of two triangular holes (Figure 42g). Loops and stretched chains containing a series of alternating B and N atoms were also observed (Figure 42h-k). Collectively, these observations indicate that single chains comprised of B and N atoms may be formed when holes in hBN coalesce. Note that some of the brighter spots at the edge of the triangular holes may be due to Si atoms. Although the materials described herein were not subjected to further chemical analysis, there does not appear to be any metal residue during the synthesis or transfer processes.[141] Moreover, Si atoms are commonly observed in materials synthesized via CVD in quartz vessels.[169] We conclude that the Si atoms may move around freely on the surfaces of hBN, but do not contribute to any hole growth. This conclusion was based in part on a report indicating that pure Si is unlikely to exhibit drilling or etching behavior in graphene.[170] Apart from silicon or other metal atoms, oxygen containing species may contribute to hole formation mechanism because there are much oxygen and water vapor inside TEM even in UHV condition. Although chemical etching effect might be considered in understating damage mechanism of materials in TEM, only knock-on damage is addressed in this study.

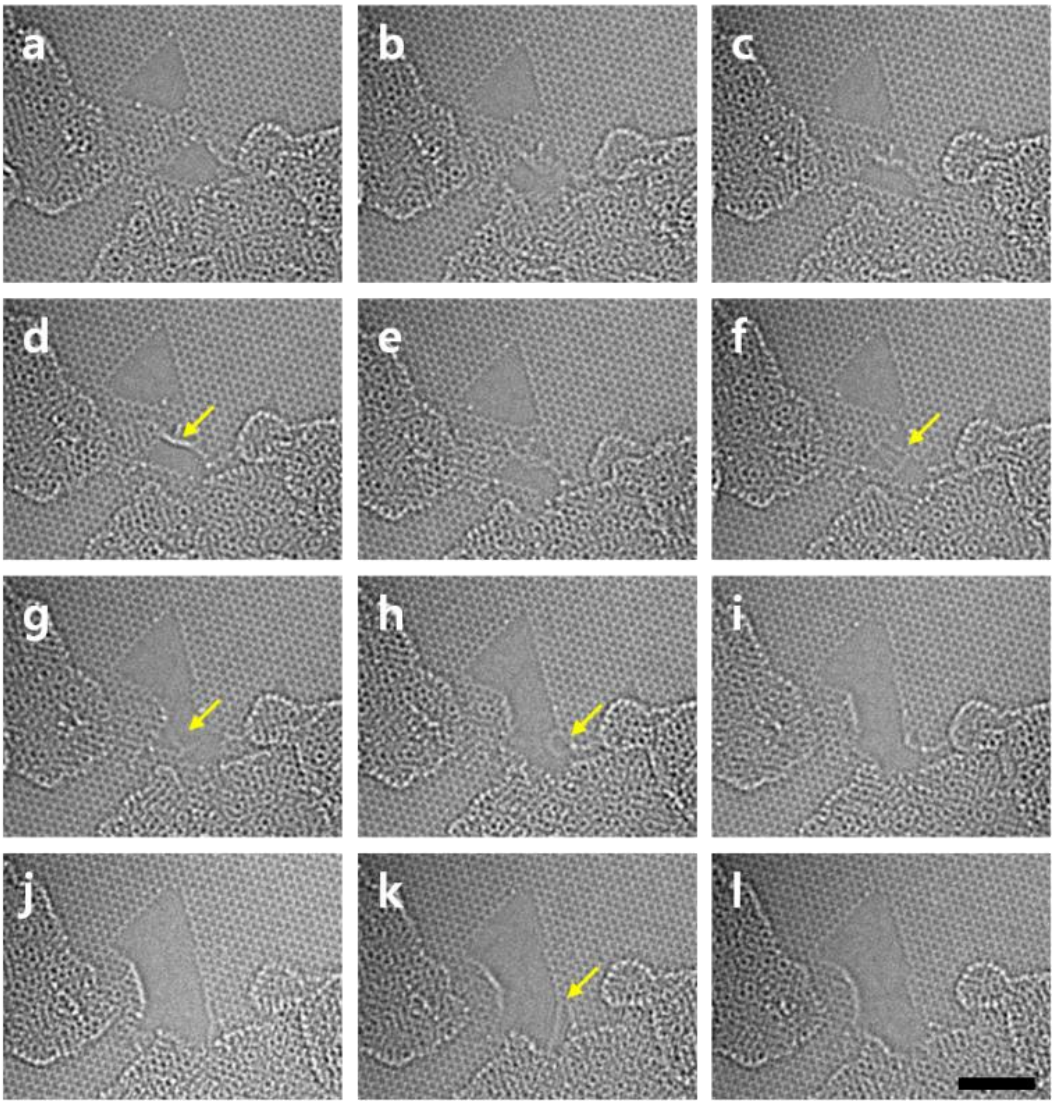

Figure 42. A series of TEM images showing how two triangular holes merge in a monolayer of hBN. The yellow arrows indicate single chains or loops containing B and N. The scale bar is 2 nm.

As indicated in Figure 43, the migration of atoms along the edges of the holes in hBN was also evaluated over time. Although the B and N atoms may be predicted to move faster than the sampling time required for sequential imaging, a series of meta-stable configurations at the hole edges was observed. For example, the blue arrow in Figure 43b points to a series of missing B and N atoms sites whereas subsequent migration changed the shape of the hole as indicated in Figure 43c. In an earlier study, it was reported that electron beam irradiation does not induce the migration of B and N atoms in hBN;[171] however, the data presented here clearly show that the migration as well as reconstruction of B and N atoms on monolayer hBN is possible. Although the adding atoms to the hole might be derived from adventitious carbon adsorbates, it is more likely that B and N atoms migrate because the number of adding atoms and missing atoms in hBN sheet are same and the distance between adding atoms and missing atoms is shorter than that between adding atoms and carbon adsorbates. As such, holes may not grow but may become filled, at least partially, by the migration of B and N atoms over time. Collectively, these observations differ from those obtained with graphene. In graphene, various hydrocarbon adsorbates adhere to the surface and carbon impurities are often abundant so that the addition of carbon atoms to holes and/or migration is relatively more likely to occur under electron beam irradiation. While the lack of B and N sources intrinsically limits the addition of such atoms to holes in hBN, the migration of such atoms does appear to occur, albeit infrequently.

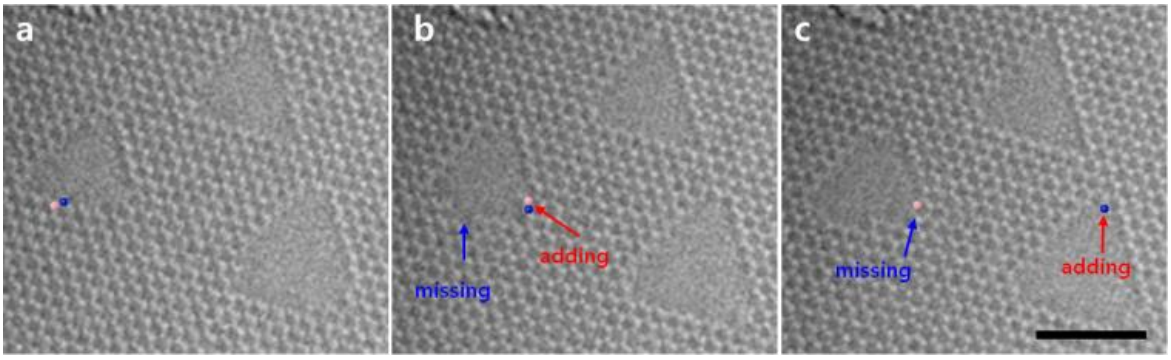

Figure 43. A series of TEM images of triangular holes produced by the prolonged irradiation of hBN. The blue dots represent N atoms whereas the red dots represent B atoms. The migration of the B and N atoms is observed over time. The scale bar is 2 nm.

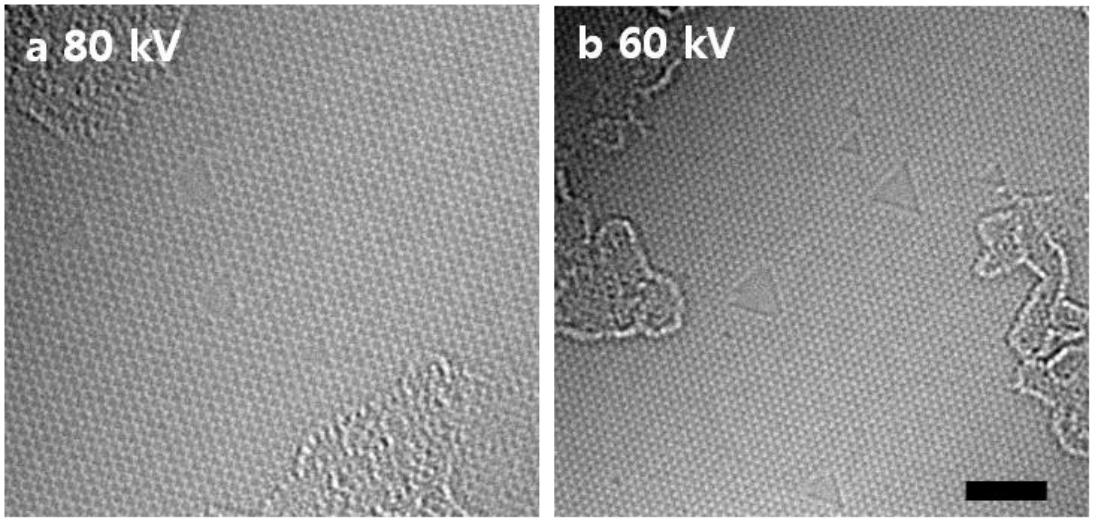

Figure 44. Triangular holes in hBN sheet after electron beam irradiation with different acceleration voltages. Although triangular holes are formed at 80 kV as well as 60 kV, my experiments were performed at 80 kV. The scale bar is 2 nm.

5.3. Molybdenum Disulfide

5.3.1. Line-defect mediated formation of hole and Mo clusters in monolayer MoS_2

To elucidate the formation mechanism of hole and Mo clusters in monolayer MoS_2 sheet, the experiment with electron beam irradiation onto the MoS_2 was conducted using ARTEM. A large area monolayer MoS_2 membranes grown by chemical vapor deposition was used for imaging at atomic resolution as shown in Figure 45. To investigate the formation of holes and Mo clusters in monolayer MoS2 sheet, the overall formation process of hole and Mo cluster induced by electron beam irradiation was analyzed at an over focused imaging condition, which shows the defects better than at an in-focus condition. The formation process of hole and Mo cluster was subsequently investigated as shown in figure 24 using the sequential imaging. Under electron beam irradiation, S vacancies are formed in MoS_2 sheet due to the lower displacement threshold of S compared to Mo.[105] With the accumulation of S vacancies, line defects appear instead of vacancy clusters in MoS_2 sheet due to diffusion of nearby S vacancies and continuous generation of new S vacancies adjacent to diffusion path of S vacancies. Considering the formation energy of line defects, when the accumulation of S vacancies is arranged in a line, the formation energy is decreasing.[79] Line defects indicated by yellow arrows are shown in Figure 46a. While continuous electron beam irradiation, line defects elongated to the arrow head directions (Figure 46b). The reason is that line defects induced by diffusion of S vacancies and knocking off S atoms appear along the directions of arranging S atoms such as [100], [010] and $[11\bar{0}]$ in MoS_2 sheet. These defects are propagated to a point through paths extending line defects (Figures 46c-f). During the process, the line defects interacted with each other to form nano-sized holes (Figures 46g and h). Based on the displacement threshold of Mo and S atoms, Mo atoms assembled at the edge of the hole and were transformed to Mo clusters as shown in Figure 46i.

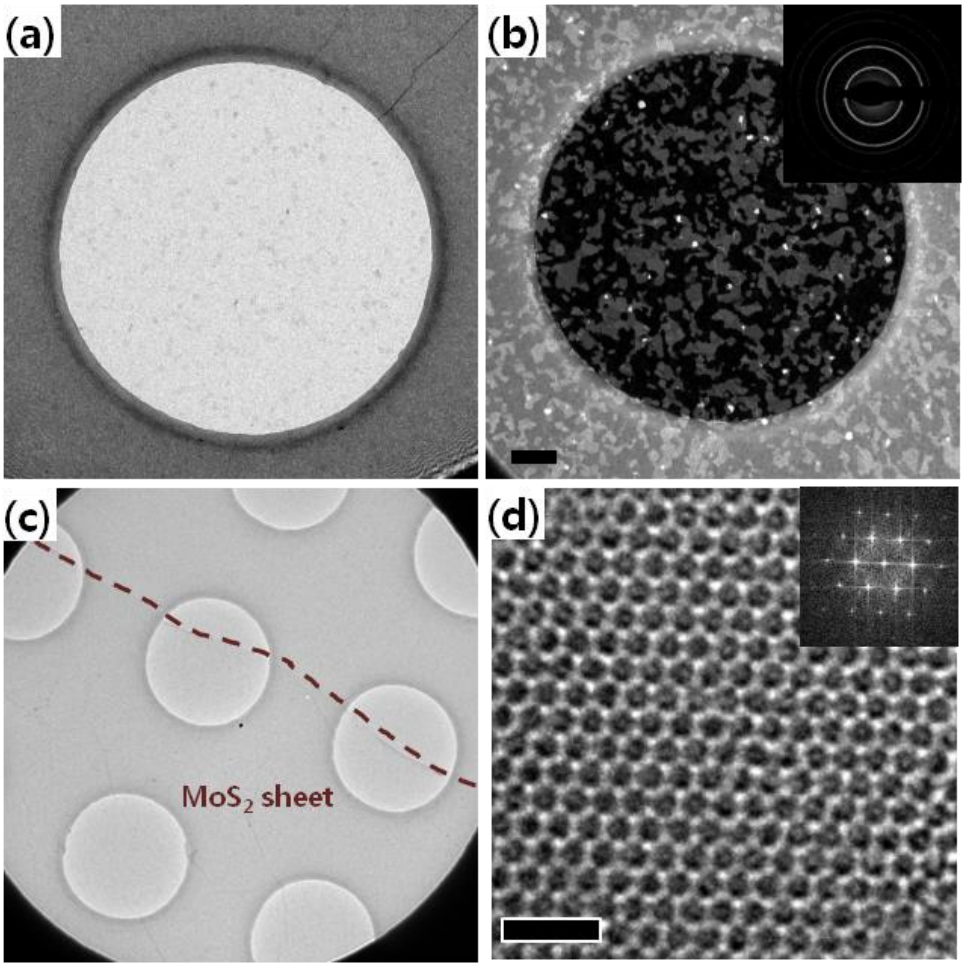

Figure 45. Monolayer MoS_2 sheets prepared on TEM grid. (a) Bright field image and (b) Dark field image with corresponding diffraction pattern of monolayer MoS_2 sheet. Scale bar is 0.2 ㎛. Objective aperture size is 1.28 1/nm. (c) Low magnification image of freestanding MoS_2 sheet. (d) ARTEM image of monolayer MoS_2. The corresponding digital diffractogram is shown in the inset. The scale bar is 1 nm.

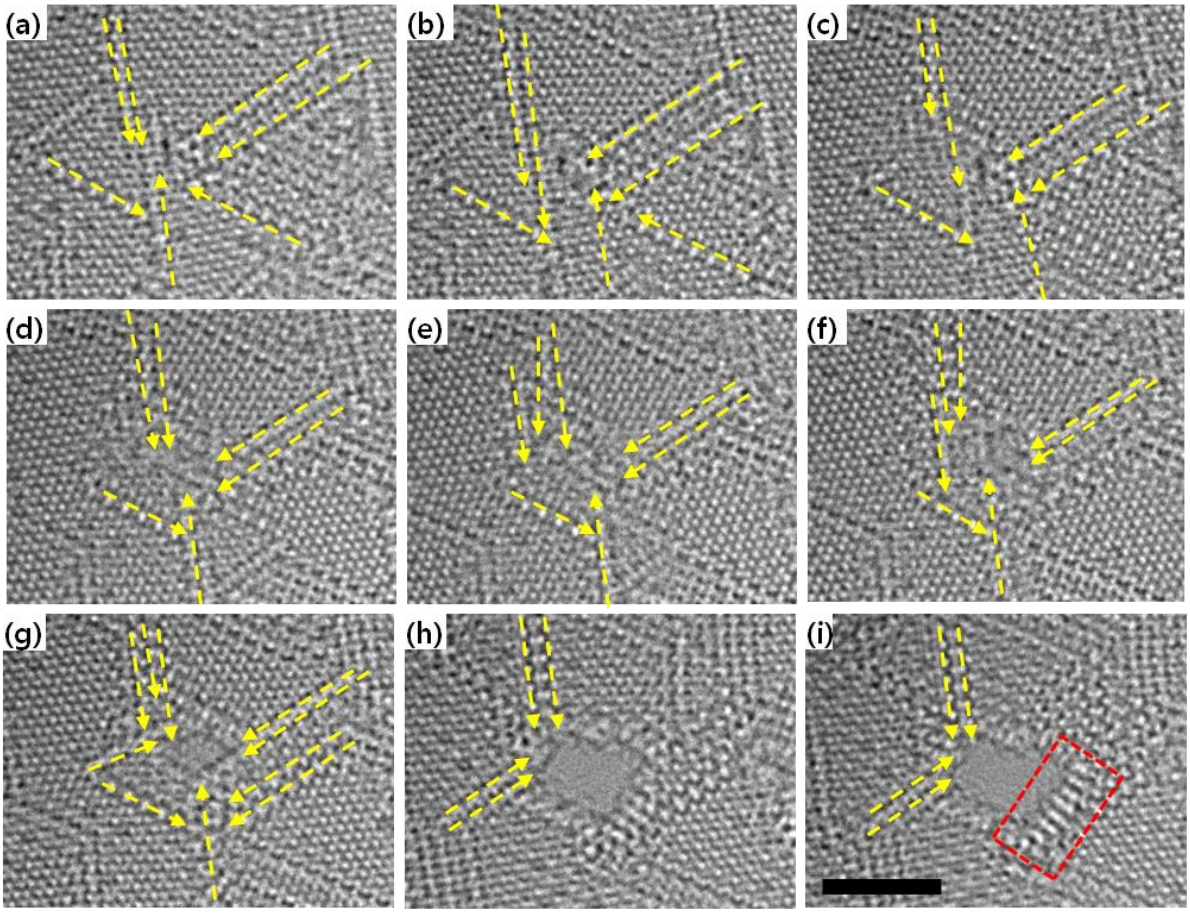

Figure 46. The process of forming a hole and Mo clusters in monolayer MoS_2. The process starts (a) with the forming line defects and these merge with each other as shown in (b) to (f). The yellow arrows indicate line defects. From (g) to (i), it is evident that a hole and Mo cluster are formed by electron beam irradiation. The red box indicates a Mo cluster. The scale bar is 2 nm.

Under electron beam irradiation, S vacancies are formed in MoS_2 sheet due to the lower displacement threshold of S compared to Mo [172]. With the increasing of S vacancies, line defects are observed instead of vacancy clusters in MoS_2 sheet [173]. Line defects encounter other line defects and then a hole is formed as shown in Figure 47a. While the hole gets larger with knocking off S atoms from the lattice, Mo atoms are aggregated at the edge of the hole. Aggregated Mo atoms are rearranged to form well-ordered Mo clusters as shown in Figure 47d-i.

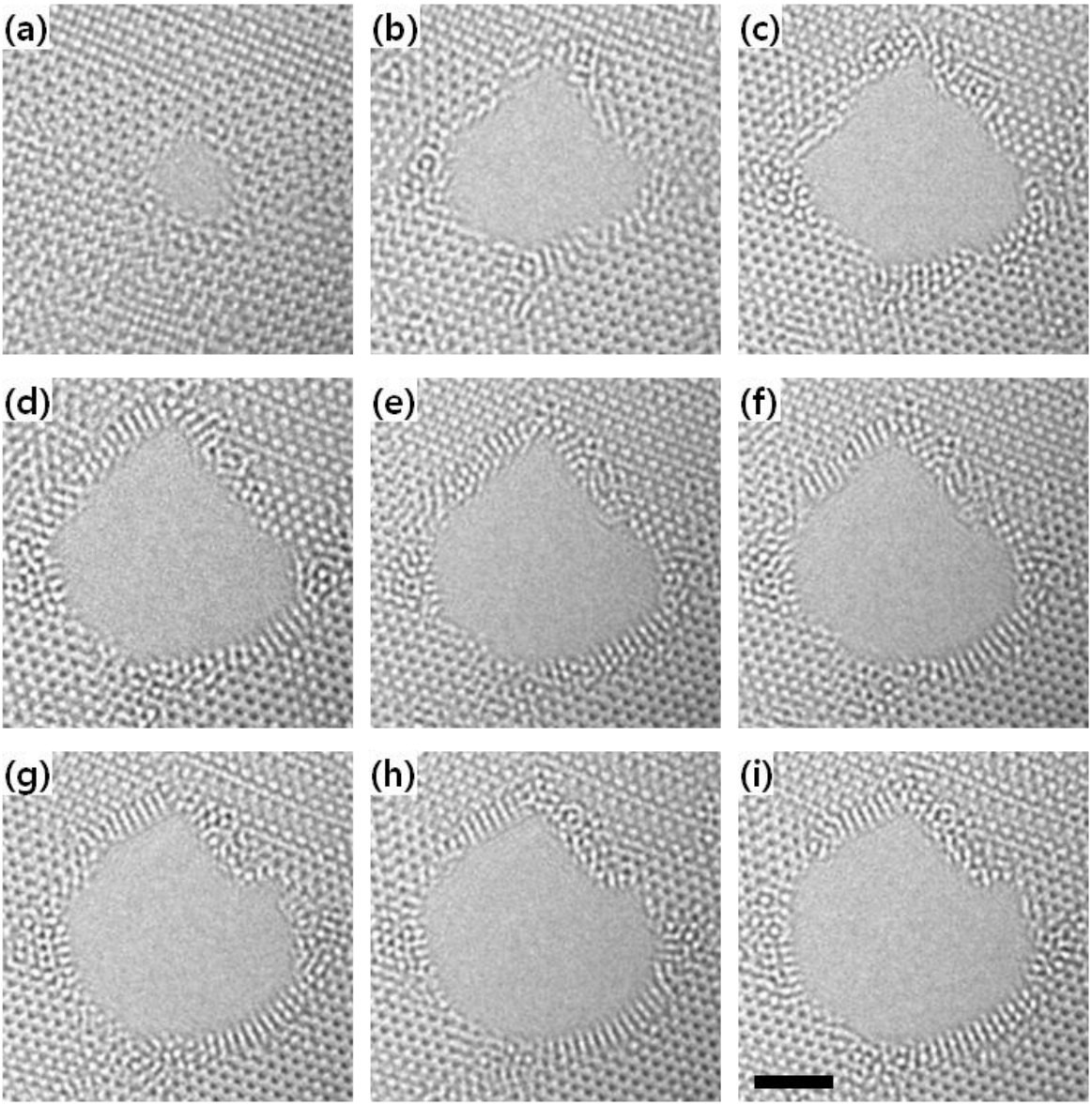

Figure 47. HREM images showing the sequential formation of a hole and Mo clusters in monolayer MoS_2 at atomic resolution. (a), (b) and (c) show rearrangement of Mo atoms and growth of a hole. From (d) to (i), surrounding Mo clusters are formed under electron beam irradiation. The scale bar is 2 nm.

To determine the crystal structure of the irradiation-induced Mo clusters, the atomic structure is investigated. As Mo cluster consists of at most two and three atom sites along the radial atomic columns around the hole as indicated in the ARTEM images along with intensity profiles in Figure 48, Mo atomic columns are distributed along the edge of the hole. When the hole is getting enlarged, the transformation from MoS_2 sheet to Mo clusters is achieved via realignment of Mo atoms as shown in Figure 48a and b. In the higher magnification images of Figure 48c-f, it is found that only Mo cluster with a distance about 0.22 nm between the two columns consisting of Mo atoms can match an atomic spacing of crystal structure of pure Mo [174]. But, compared to MoS_2 sheet, the distance between two columns is about 30 % shorter than lattice constant of MoS_2 sheet.

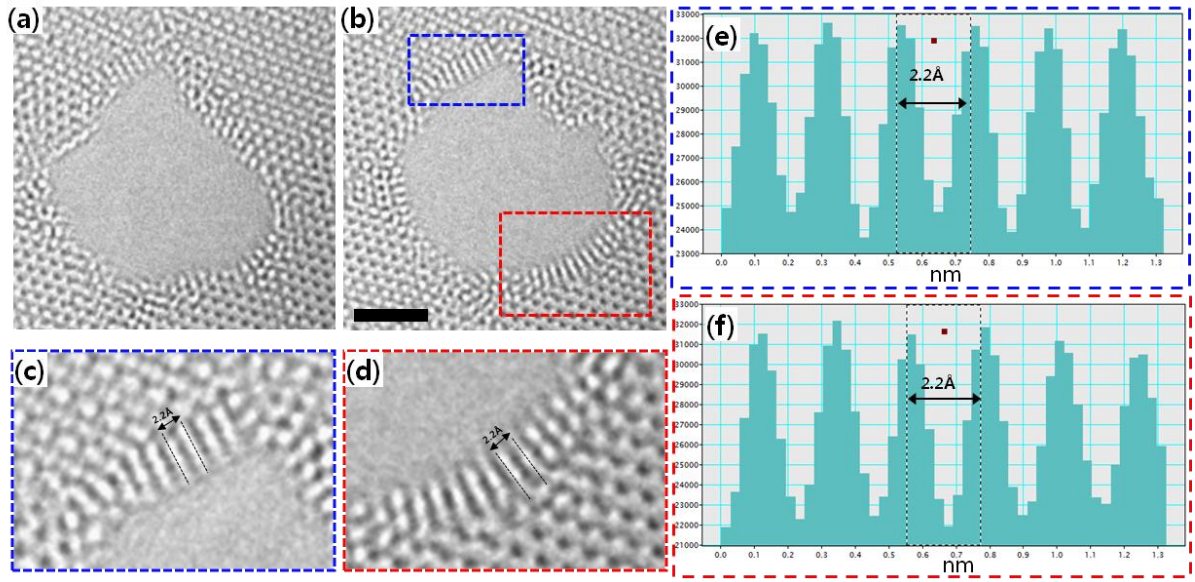

Figure 48. Atomic structure of Mo clusters formed under electron beam irradiation. (a) The initial image of Mo cluster formation. (b) The image of Mo clusters, where a structure can be seen clearly. (c) and (d) Enlarged dashed blue and red boxes shown in Fig 1b, respectively. These images indicate distance between Mo atom columns. (e) and (f) Intensity profiles corresponding to the distances between Mo atom columns in (c) and (d), respectively. The scale bar is 2 nm.

Line defects formed by electron beam irradiation tend to induce rearrangement of Mo atoms surrounding the hole in MoS_2 sheet, which result in local formation of straight atomic column structure (See the left upper part of Figure 49b). It is evident that about 6-atom by 3-atom big rectangular Mo sheet is induced by this process. However, the columns of Mo atoms attached on the edge of MoS_2 (See right lower part of Figure 49b) can have strain due to coherent bonding between Mo columns and MoS_2 lattice. Therefore, fanwise Mo column structure also can be formed as shown in the lower Mo cluster of Figure 49b.

Figure 49c shows intensity profiles of atoms in a raw image. The Mo clusters and MoS_2 sheet can be distinguished in the image as the Mo atoms in Mo clusters display 18 % higher intensity than Mo atoms in MoS_2 sheet with ± 3% deviation due to narrow distance between Mo atoms and crystallinity of Mo cluster in the image. To confirm the intensity variation observed in the experimental image, image simulation was performed at the imaging condition using MacTempasX (Figure 49d). Figure 49c and d show that the intensity profiles of experimental image and the corresponding simulation image are in good agreement. The results also indicate that the Mo cluster is a single layer of Mo atoms.

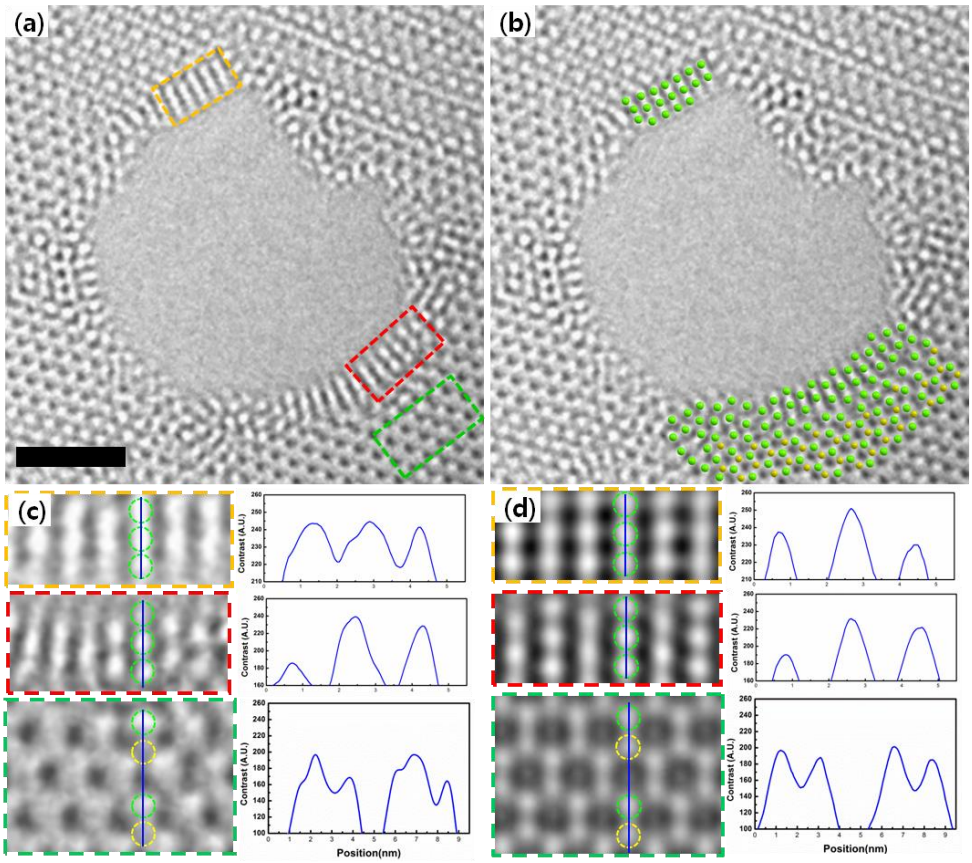

Figure 49. Atomic positions overlay on Mo clusters in (a) and (b). (c) Raw experimental images taken by an ARTEM and intensity profiles from the trace in the raw images. (d) Simulated image at the imaging condition and intensity profiles from simulated images. The green and yellow dots indicate Mo and S atoms, respectively. The scale bar is 2 nm.

The Mo cluster can be transformed into a body-centered cubic (bcc) structure, which is the crystal structure of bulk Mo, after MoS_2 sheet is separated from Mo cluster by prolonged electron beam irradiation. The sequential ARTEM images representing the phase transition of Mo cluster are shown in Figure 50 with the corresponding digital diffractograms. When the transformation does not happen fully, unordered Mo structure is observed, as shown in Figure 50a. However, through longer electron beam irradiation, this turned to a bcc Mo structure as shown in ARTEM images of Figure 50b-d along the [100] zone axis. Once the transformation has taken place as about 7-atom by 7-atom big bcc structure, this structure is retained even under longer exposure of electron beam irradiation.

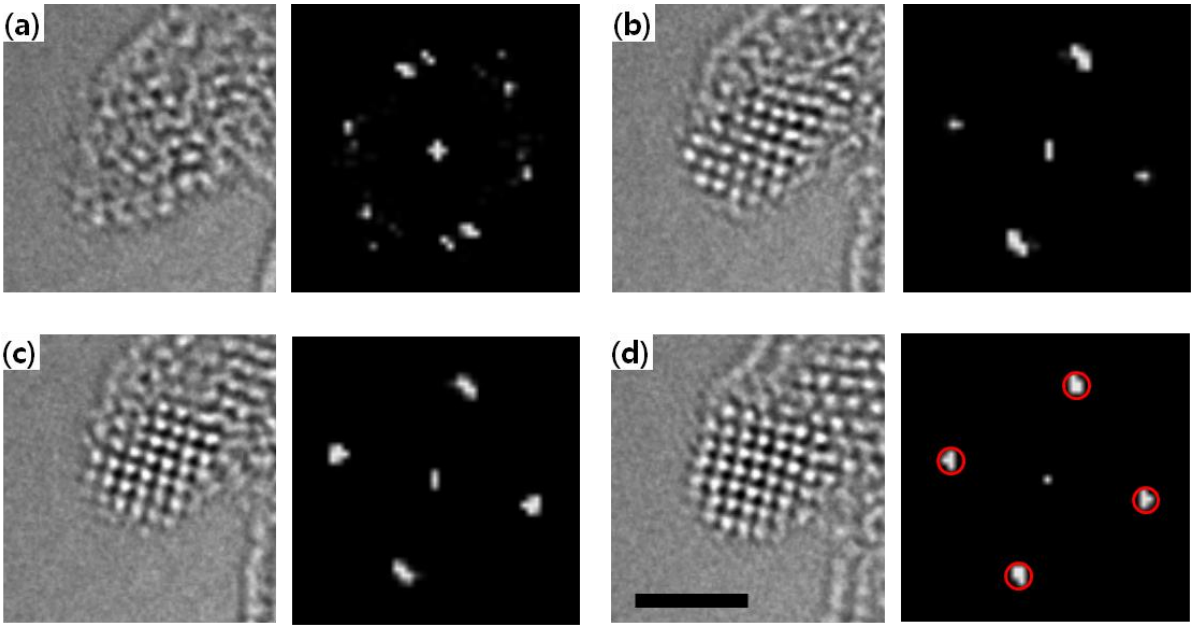

Figure 50. Phase transition of atomic structure of Mo cluster. (a) The ARTEM image of intermediate Mo structure. (b), (c) and (d) showing transition to body-centered cubic structure along the [100] zone axis. The corresponding diffractograms indicate the development of Mo structure. The scale bar is 2 nm.

However, these phenomena are surely happened only within a single grain of MoS_2 sheet because a line defect should be merged with another line defect to form a hole and Mo clusters. Grain boundaries act as sinks for line defects, absorbing all incoming line defects. Thus, subsequent formation of holes and Mo clusters does not occur at the grain boundary, as shown in Figure 51.

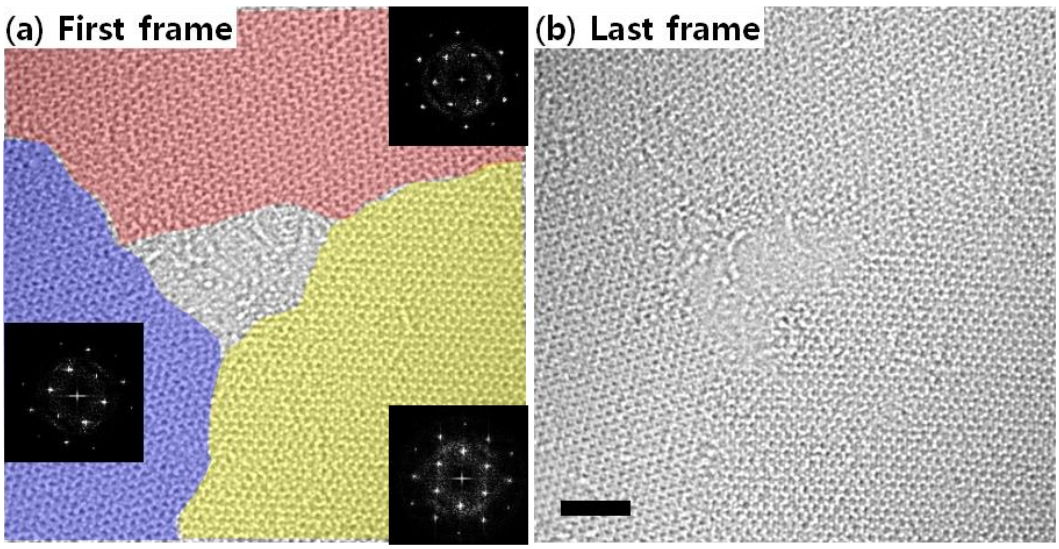

Figure 51. The grain boundaries at a triple junction in MoS_2 sheet. (a) and (b) show the first and last frames. The inset diffractograms indicate the different orientation of grains. A long electron irradiation did not generate Mo clusters. The scale bar is 2 nm.

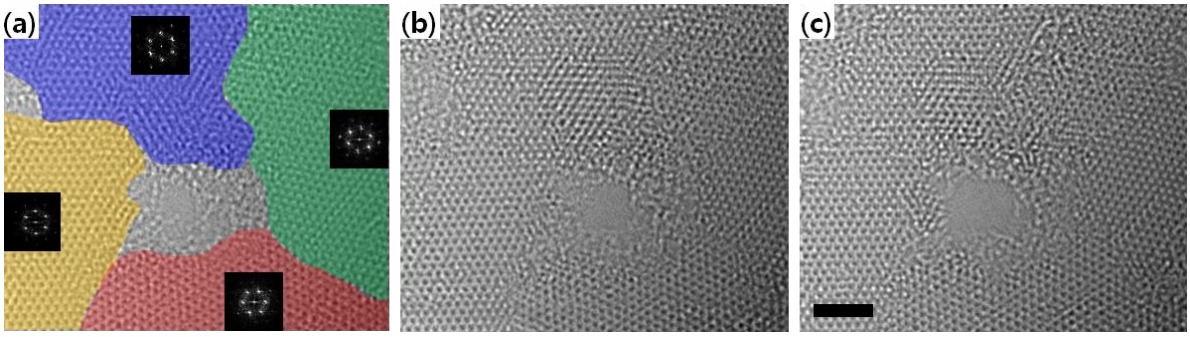

Figure 52. The hole in monolayer MoS_2 sheet at grain boundary. (a), (b) and (c) Same region shows the growth of hole under electron beam irradiation. When the hole grows at grain boundary, the Mo atomic layer structure is not formed. The digital diffractorgrams indicate the different crystallographic orientation of grains. The scale bar is 2 nm.

Chapter 6: Conclusion

In summary, I characterized UV/Ozone- and oxygen plasma-treated monolayer graphene sheets using ARTEM imaging and EELS. When UVO was used to treat the graphene sheets, oxygen atoms were attached to the surface and the surface was covered with contaminants; however, the graphene lattice was not distorted. By contrast, when oxygen plasma was used to treat the graphene sheets, not only was oxygen attached to the graphene surface, but topological defects were also introduced onto the graphene lattice. These topological defects effectively induced the partial surface oxidation of the graphene because the strain in the curvature of the topological defects resulted in increased chemical functionalities. Notably, my findings emphasize that facile dry oxidation treatments can efficiently modify the graphene surface and induce differences in the formation of topological defects in the graphene lattice. In addition, this study provides a method for the partial surface oxidation of graphene and enhances our understanding of the resulting topological defects and oxygen atoms on oxidized graphene surfaces at the atomic scale. (This research was published in *2D Materials* in 2017 and title is "Effects of dry oxidation treatments on monolayer graphene".)

And, I explained my observations showing the formation of various point defects involving OH molecules in a monolayer graphene sheet. These included images showing the atomic structures for MVs, DVs, and a pair of 13-5 rings, which had not been previously observed or proposed. We referred to an oxygen-containing functional group adsorbed onto a graphene surface, which enabled the formation of point defects under electron beam irradiation, and to hydrogen atoms, which could stabilize the pair of 13-5 rings. Unlike previous reports, our observations showed that the desorption process of the simultaneous bonding of C–O atoms onto a graphene surface actually had intermediate states in the formation of point defects. Furthermore, hydrogen atoms might be contained the configuration of the pair of 13-5 rings to stabilize the defect. These mediating atoms could readily re-bond with neighboring carbon atoms owing to a low net energy requirement; therefore, these atoms were often the site of defect reconfiguration, a finding reinforced by DFT calculations. The images and analysis directly demonstrated that the oxygen and hydrogen atoms bonded to carbon atoms on the graphene surface as functional groups induced vacancies with intermediate states and that they stabilized the pair of 13-5 rings. Therefore, oxygen and hydrogen atoms are very important in defect engineering and the optimization of graphene. (This research will be submitted.)

In the case of monolayer hBN sheets, I observed the growth of triangular holes using sequential ARTEM imaging. When a monolayer of hBN was subjected to electron beam irradiation, a vacancy formed initially and grew while maintaining a triangular shape. Such shapes were observed even when such holes merged. Through a series of TEM images that were supported by DFT calculations and MD simulations, the mechanism for the growth of these holes appeared to involve the ejection of B and N atoms near the centers of the hole edges and also the ejection of bundles of atoms. Such processes involve the breaking of B–N bonds perpendicular to the hole edges and result in the formation of single

chains containing B and N atoms. Multiple chains containing B and N were also observed when two holes merged together, while previous studies have focused primarily on the observation of a single chain of C atoms in holes in graphene. Moreover, the migration of B and N atoms in monolayers of hBN was observed using ARTEM, as indicated by edge reconstruction, although such phenomena occur less frequently when compared to analogous carbon-based materials (i.e., graphene). (This research was published in *Nanoscale* in 2015 and title is "Atomic-scale dynamics of triangular hole growth in monolayer hexagonal boron nitride under electron irradiation".)

Lastly, the holes and Mo clusters in MoS_2 monolayers generated by electron beam irradiation were observed using sequential ARTEM imaging. When monolayer MoS_2 sheet was subjected to electron beam irradiation, S vacancies are formed initially due to lower displacement threshold of S atoms than Mo atoms and line defects appear due to diffusion of nearby S vacancies and continuous generation of new S vacancies. Through a series of ARTEM images, the formation of a hole appears to be involved with merging of several line defects. Such processes include phase transformation from MoS_2 to bcc Mo. After MoS_2 sheet is completely torn, the Mo cluster separated from MoS_2 sheet is transformed to the bcc structure of pure Mo. These phenomena occur only within a grain of MoS_2, since line defects are absorbed by grain boundaries. Our results indicate that the formation of holes and nano metal clusters of Mo in MoS_2 monolayers can be created by line defects under electron beam irradiation. It implies that one type of defect can introduce another type of defect in 2D TMDs with an external excitation stimulus. (This research was published in *2D Materials* in 2016 and title is "Line-defect mediated formation of hole and Mo clusters in monolayer molybdenum disulfide".)

References

1. Hsiao, M.-C.; Liao, S.-H.; Yen, M.-Y.; Liu, P.-I.; Pu, N.-W.; Wang, C.-A.; Ma, C.-C. M., Preparation of covalently functionalized graphene using residual oxygen-containing functional groups. *ACS Appl. Mater. Interfaces* **2010,** *2* (11), 3092-3099.

2. Šljivančanin, Ž.; Milošević, A. S.; Popović, Z. S.; Vukajlović, F. R., Binding of atomic oxygen on graphene from small epoxy clusters to a fully oxidized surface. *Carbon* **2013,** *54*, 482-488.

3. Liu, H.; Kang, B.; Lee, J. Y., Hidden Role of a Hydroxyl Group in Mediating the Oxygen Line Defect on a Graphene Surface. *J. Phys. Chem. C* **2013,** *117* (34), 17832-17838.

4. Sun, T.; Fabris, S.; Baroni, S., Surface precursors and reaction mechanisms for the thermal reduction of graphene basal surfaces oxidized by atomic oxygen. *J. Phys. Chem. C* **2011,** *115* (11), 4730-4737.

5. Yamada, Y.; Murota, K.; Fujita, R.; Kim, J.; Watanabe, A.; Nakamura, M.; Sato, S.; Hata, K.; Ercius, P.; Ciston, J., Subnanometer vacancy defects introduced on graphene by oxygen gas. *J. Am. Chem. Soc.* **2014,** *136* (6), 2232-2235.

6. Hossain, M. Z.; Johns, J. E.; Bevan, K. H.; Karmel, H. J.; Liang, Y. T.; Yoshimoto, S.; Mukai, K.; Koitaya, T.; Yoshinobu, J.; Kawai, M., Chemically homogeneous and thermally reversible oxidation of epitaxial graphene. *Nat. Chem.* **2012,** *4* (4), 305-309.

7. Tang, Y.; Dai, X.; Yang, Z.; Pan, L.; Chen, W.; Ma, D.; Lu, Z., Formation and catalytic activity of Pt supported on oxidized graphene for the CO oxidation reaction. *Phys. Chem. Chem. Phys.* **2014,** *16* (17), 7887-7895.

8. Topsakal, M.; Ciraci, S., Domain formation on oxidized graphene. *Phys. Rev. B* **2012,** *86* (20), 205402.

9. Xiang, H.; Wei, S.-H.; Gong, X., Structural motifs in oxidized graphene: A genetic algorithm study based on density functional theory. *Phys. Rev. B* **2010,** *82* (3), 035416.

10. Yan, J.-A.; Xian, L.; Chou, M., Structural and electronic properties of oxidized graphene. *Phys. Rev. Lett.* **2009,** *103* (8), 086802.

11. Aria, A. I.; Gani, A. W.; Gharib, M., Effect of dry oxidation on the energy gap and chemical composition of CVD graphene on nickel. *Appl. Surf. Sci.* **2014,** *293*, 1-11.

12. Han, T.-H.; Kwon, S.-J.; Seo, H.-K.; Lee, T.-W., Controlled surface oxidation of multi-layered graphene anode to increase hole injection efficiency in organic electronic devices. *2D Mater.* **2016,** *3* (1), 014003.

13. Wang, W.; Ruiz, I.; Lee, I.; Zaera, F.; Ozkan, M.; Ozkan, C. S., Improved functionality of graphene and carbon nanotube hybrid foam architecture by UV-ozone treatment. *Nanoscale* **2015,** *7* (16), 7045-7050.

14. Shenoy, G. J.; Parobek, D.; Salim, M.; Li, Z.; Tian, C.; Liu, H., Substrate dependent photochemical oxidation of monolayer graphene. *RSC Adv.* **2016,** *6* (10), 8489-8494.

15. Xiao, N.; Dong, X.; Song, L.; Liu, D.; Tay, Y.; Wu, S.; Li, L.-J.; Zhao, Y.; Yu, T.; Zhang, H., Enhanced thermopower of graphene films with oxygen plasma treatment. *ACS Nano* **2011,** *5* (4), 2749-2755.

16. McEvoy, N.; Nolan, H.; Kumar, N. A.; Hallam, T.; Duesberg, G. S., Functionalisation of graphene surfaces with downstream plasma treatments. *Carbon* **2013,** *54*, 283-290.

17. Nourbakhsh, A.; Cantoro, M.; Klekachev, A. V.; Pourtois, G.; Vosch, T.; Hofkens, J.; van der Veen, M. H.; Heyns, M. M.; De Gendt, S.; Sels, B. F., Single layer vs bilayer graphene: a comparative study of the effects of oxygen plasma treatment on their electronic and optical properties. *J. Phys. Chem. C* **2011,** *115* (33), 16619-16624.

18. Rani, J.; Lim, J.; Oh, J.; Kim, J.-W.; Shin, H. S.; Kim, J. H.; Lee, S.; Jun, S. C., Epoxy to carbonyl group conversion in graphene oxide thin films: effect on structural and luminescent characteristics. *J. Phys. Chem. C* **2012,** *116* (35), 19010-19017.

19. Shin, Y. J.; Wang, Y.; Huang, H.; Kalon, G.; Wee, A. T. S.; Shen, Z.; Bhatia, C. S.; Yang, H., Surface-energy engineering of graphene. *Langmuir* **2010,** *26* (6), 3798-3802.

20. Kim, D. C.; Jeon, D.-Y.; Chung, H.-J.; Woo, Y.; Shin, J. K.; Seo, S., The structural and electrical evolution of graphene by oxygen plasma-induced disorder. *Nanotechnology* **2009,** *20* (37), 375703.

21. Nourbakhsh, A.; Cantoro, M.; Vosch, T.; Pourtois, G.; Clemente, F.; van der Veen, M. H.; Hofkens, J.; Heyns, M. M.; De Gendt, S.; Sels, B. F., Bandgap opening in oxygen plasma-treated graphene. *Nanotechnology* **2010,** *21* (43), 435203.

22. Pacilé, D.; Meyer, J.; Rodríguez, A. F.; Papagno, M.; Gomez-Navarro, C.; Sundaram, R.; Burghard, M.; Kern, K.; Carbone, C.; Kaiser, U., Electronic properties and atomic structure of graphene oxide membranes. *Carbon* **2011,** *49* (3), 966-972.

23. Zhan, D.; Ni, Z.; Chen, W.; Sun, L.; Luo, Z.; Lai, L.; Yu, T.; Wee, A. T. S.; Shen, Z., Electronic structure of graphite oxide and thermally reduced graphite oxide. *Carbon* **2011,** *49* (4), 1362-1366.

24. Jeong, H.-K.; Noh, H.-J.; Kim, J.-Y.; Jin, M.; Park, C.; Lee, Y., X-ray absorption spectroscopy of graphite oxide. *EPL* **2008,** *82* (6), 67004.

25. Zhou, J.; Wang, J.; Sun, C.; Maley, J.; Sammynaiken, R.; Sham, T.; Pong, W., Nano-scale chemical imaging of a single sheet of reduced graphene oxide. *J. Mater. Chem.* **2011,** *21* (38), 14622-14630.

26. Tararan, A.; Zobelli, A.; Benito, A. M.; Maser, W. K.; Stéphan, O., Revisiting graphene oxide chemistry via spatially-resolved electron energy loss spectroscopy. *Chem. Mater.* **2016,** *28* (11), 3741-3748.

27. Hamon, A.-L.; Verbeeck, J.; Schryvers, D.; Benedikt, J.; vd Sanden, R. M., ELNES study of carbon K-edge spectra of plasma deposited carbon films. *J. Mater. Chem.* **2004,** *14* (13), 2030-2035.

28. Francis, J.; Hitchcock, A., Inner-shell spectroscopy of p-benzoquinone, hydroquinone, and phenol: distinguishing quinoid and benzenoid structures. *J. Phys. Chem. A* **1992,** *96* (16), 6598-6610.

29. Stambula, S.; Gauquelin, N.; Bugnet, M.; Gorantla, S.; Turner, S.; Sun, S.; Liu, J.; Zhang, G.; Sun, X.; Botton, G. A., Chemical structure of nitrogen-doped graphene with single platinum atoms and atomic clusters as a platform for the PEMFC electrode. *J. Phys. Chem. C* **2014,** *118* (8), 3890-3900.

30. Mkhoyan, K. A.; Contryman, A. W.; Silcox, J.; Stewart, D. A.; Eda, G.; Mattevi, C.; Miller, S.; Chhowalla, M., Atomic and electronic structure of graphene-oxide. *Nano Lett.* **2009,** *9* (3), 1058-1063.

31. Grunes, L.; Leapman, R.; Wilker, C.; Hoffmann, R.; Kunz, A., Oxygen K near-edge fine structure: An electron-energy-loss investigation with comparisons to new theory for selected 3 d Transition-metal oxides. *Phys. Rev. B* **1982,** *25* (12), 7157.

32. El-Barbary, A.; Telling, R.; Ewels, C.; Heggie, M.; Briddon, P., Structure and energetics of the vacancy in graphite. *Phys. Rev. B* **2003,** *68* (14), 144107.

33. Robertson, A. W.; Allen, C. S.; Wu, Y. A.; He, K.; Olivier, J.; Neethling, J.; Kirkland, A. I.; Warner, J. H., Spatial control of defect creation in graphene at the nanoscale. *Nat. Commun.* **2012,** *3*, ncomms2141.

34. Banhart, F., Irradiation effects in carbon nanostructures. *Rep. Prog. Phys.* **1999,** *62* (8), 1181.

35. Hashimoto, A.; Suenaga, K.; Gloter, A.; Urita, K.; Iijima, S., Direct evidence for atomic defects in graphene layers. *Nature* **2004,** *430* (7002), 870-873.

36. Lee, G.-D.; Wang, C.; Yoon, E.; Hwang, N.-M.; Kim, D.-Y.; Ho, K., Diffusion, coalescence, and reconstruction of vacancy defects in graphene layers. *Phys. Rev. Lett.* **2005,** *95* (20), 205501.

37. Yazyev, O. V.; Helm, L., Defect-induced magnetism in graphene. *Phys. Rev. B* **2007,** *75* (12), 125408.

38. Kaloni, T. P.; Cheng, Y.; Faccio, R.; Schwingenschlögl, U., Oxidation of monovacancies in graphene by oxygen molecules. *J. Mater. Chem.* **2011,** *21* (45), 18284-18288.

39. Robertson, A. W.; Montanari, B.; He, K.; Allen, C. S.; Wu, Y. A.; Harrison, N. M.; Kirkland, A. I.; Warner, J. H., Structural reconstruction of the graphene monovacancy. *ACS Nano* **2013,** *7* (5), 4495-4502.

40. Denis, P. A.; Iribarne, F., Comparative study of defect reactivity in graphene. *J. Phys. Chem. C* **2013,** *117* (37), 19048-19055.

41. Banhart, F.; Kotakoski, J.; Krasheninnikov, A. V., Structural defects in graphene. *ACS Nano* **2010,** *5* (1), 26-41.

42. Kim, Y.; Ihm, J.; Yoon, E.; Lee, G.-D., Dynamics and stability of divacancy defects in graphene. *Phys. Rev. B* **2011,** *84* (7), 075445.

43. Kotakoski, J.; Krasheninnikov, A.; Kaiser, U.; Meyer, J., From point defects in graphene to two-dimensional amorphous carbon. *Phys. Rev. Lett.* **2011,** *106* (10), 105505.

44. Pereira, V. M.; Guinea, F.; Dos Santos, J. L.; Peres, N.; Neto, A. C., Disorder induced localized states in graphene. *Phys. Rev. Lett.* **2006,** *96* (3), 036801.

45. Thrower, P.; Mayer, R., Point defects and self-diffusion in graphite. *Phys. Status Solidi* **1978,** *47* (1), 11-37.

46. Hjort, M.; Stafström, S., Modeling vacancies in graphite via the Hückel method. *Phys. Rev. B* **2000,** *61* (20), 14089.

47. Lim, D.-H.; Negreira, A. S.; Wilcox, J., DFT studies on the interaction of defective graphene-supported Fe and Al nanoparticles. *J. Phys. Chem. C* **2011,** *115* (18), 8961-8970.

48. Ahlam, A. First principles characterisation of defects in irradiated graphitic materials. University

of Sussex, 2005.

49. Kaxiras, E.; Pandey, K., Energetics of defects and diffusion mechanisms in graphite. *Phys. Rev. Lett.* **1988,** *61* (23), 2693.

50. Sammalkorpi, M.; Krasheninnikov, A.; Kuronen, A.; Nordlund, K.; Kaski, K., Mechanical properties of carbon nanotubes with vacancies and related defects. *Phys. Rev. B* **2004,** *70* (24), 245416.

51. Lehtinen, P.; Foster, A. S.; Ma, Y.; Krasheninnikov, A.; Nieminen, R. M., Irradiation-induced magnetism in graphite: a density functional study. *Phys. Rev. Lett.* **2004,** *93* (18), 187202.

52. Chen, J.-H.; Li, L.; Cullen, W. G.; Williams, E. D.; Fuhrer, M. S., Tunable Kondo effect in graphene with defects. *Nat. Phys.* **2011,** *7* (7), 535-538.

53. Zhang, L.; Xu, Q.; Niu, J.; Xia, Z., Role of lattice defects in catalytic activities of graphene clusters for fuel cells. *Phys. Chem. Chem. Phys.* **2015,** *17* (26), 16733-16743.

54. Marsh, H.; O'HAIR, E.; Reed, R.; Wynne-Jones, W., Reaction of Atomic Oxygen with Carbon. *Nature* **1963,** *198* (4886), 1195-1196.

55. Marsh, H.; O'hair, T.; Wynne-Jones, W., Oxidation of carbons and graphites by atomic oxygen kinetic studies. *J. Chem. Soc. Faraday Trans.* **1965,** *61*, 274-284.

56. Marsh, H.; O'Hair, T.; Reed, R., Oxidation of carbons and graphites by atomic oxygen an electron microscope study of surface changes. *J. Chem. Soc. Faraday Trans.* **1965,** *61*, 285-293.

57. Rosner, D.; Allendorf, H., High temperature oxidation of carbon by atomic oxygen. *Carbon* **1965,** *3* (2), 153-156.

58. Otterbein, M.; Bonnetain, L., Reaction du carbone avec l'oxygene atomique. *Carbon* **1969,** *7* (5), 539-554.

59. Marsh, H.; O'Hair, T.; Wynne-Jones, L., The carbon-atomic oxygen reaction—surface-oxide formation on paracrystalline carbon and graphite. *Carbon* **1969,** *7* (5), 555-558.

60. Wong, C.; Yang, R. T.; Halpern, B. L., The mode of attack of oxygen atoms on the basal plane of graphite. *J. Chem. Phys.* **1983,** *78* (6), 3325-3328.

61. Pattabiraman, P.; Rodriguez, N.; Jang, B.; Baker, R., A study of the interaction of atomic oxygen with various carbonaceous materials. *Carbon* **1990,** *28* (6), 867-878.

62. Bourelle, E.; Konno, H.; Inagaki, M., Structural defects created on natural graphite surface by slight treatment of oxygen plasma:–STM observations–. *Carbon* **1999,** *37* (12), 2041-2048.

63. Paredes, J.; Martinez-Alonso, A.; Tascon, J., Multiscale imaging and tip-scratch studies reveal insight into the plasma oxidation of graphite. *Langmuir* **2007,** *23* (17), 8932-8943.

64. Girit, Ç. Ö.; Meyer, J. C.; Erni, R.; Rossell, M. D.; Kisielowski, C.; Yang, L.; Park, C.-H.; Crommie, M.; Cohen, M. L.; Louie, S. G., Graphene at the edge: stability and dynamics. *Science* **2009,** *323* (5922), 1705-1708.

65. Ishii, T.; Sato, T.; Sekikawa, Y.; Iwata, M., Growth of whiskers of hexagonal boron nitride. *J. Cryst. Growth* **1981,** *52*, 285-289.

66. Paine, R. T.; Narula, C. K., Synthetic routes to boron nitride. *Chem. Rev.* **1990,** *90* (1), 73-91.

67. Alem, N.; Erni, R.; Kisielowski, C.; Rossell, M. D.; Gannett, W.; Zettl, A., Atomically thin hexagonal boron nitride probed by ultrahigh-resolution transmission electron microscopy. *Phys. Rev. B* **2009,** *80* (15), 155425.

68. Alem, N.; Ramasse, Q. M.; Seabourne, C. R.; Yazyev, O. V.; Erickson, K.; Sarahan, M. C.; Kisielowski, C.; Scott, A. J.; Louie, S. G.; Zettl, A., Subangstrom edge relaxations probed by electron microscopy in hexagonal boron nitride. *Phys. Rev. Lett.* **2012,** *109* (20), 205502.

69. Yin, L.-C.; Cheng, H.-M.; Saito, R., Triangle defect states of hexagonal boron nitride atomic layer: Density functional theory calculations. *Phys. Rev. B* **2010,** *81* (15), 153407.

70. Novoselov, K.; Jiang, D.; Schedin, F.; Booth, T.; Khotkevich, V.; Morozov, S.; Geim, A., Two-dimensional atomic crystals. *Proc. Natl. Acad. Sci. U.S.A.* **2005,** *102* (30), 10451-10453.

71. Wang, Q. H.; Kalantar-Zadeh, K.; Kis, A.; Coleman, J. N.; Strano, M. S., Electronics and optoelectronics of two-dimensional transition metal dichalcogenides. *Nat. Nanotechnol.* **2012,** *7* (11), 699-712.

72. Liu, K.-K.; Zhang, W.; Lee, Y.-H.; Lin, Y.-C.; Chang, M.-T.; Su, C.-Y.; Chang, C.-S.; Li, H.; Shi, Y.; Zhang, H., Growth of large-area and highly crystalline MoS_2 thin layers on insulating substrates. *Nano Lett.* **2012,** *12* (3), 1538-1544.

73. Lin, Y.-C.; Zhang, W.; Huang, J.-K.; Liu, K.-K.; Lee, Y.-H.; Liang, C.-T.; Chu, C.-W.; Li, L.-J., Wafer-scale MoS_2 thin layers prepared by MoO_3 sulfurization. *Nanoscale* **2012,** *4* (20), 6637-6641.

74. Lee, Y.; Lee, J.; Bark, H.; Oh, I.-K.; Ryu, G. H.; Lee, Z.; Kim, H.; Cho, J. H.; Ahn, J.-H.; Lee, C., Synthesis of wafer-scale uniform molybdenum disulfide films with control over the layer number using a gas phase sulfur precursor. *Nanoscale* **2014,** *6* (5), 2821-2826.

75. Jin, Z.; Shin, S.; Kwon, D. H.; Han, S.-J.; Min, Y.-S., Novel chemical route for atomic layer deposition of MoS_2 thin film on SiO_2/Si substrate. *Nanoscale* **2014,** *6* (23), 14453-14458.

76. Heising, J.; Kanatzidis, M. G., Exfoliated and restacked MoS2 and WS2: Ionic or neutral species? Encapsulation and ordering of hard electropositive cations. *J. Am. Chem. Soc.* **1999,** *121* (50), 11720-11732.

77. Kim, Y.; Huang, J. L.; Lieber, C. M., Characterization of nanometer scale wear and oxidation of transition metal dichalcogenide lubricants by atomic force microscopy. *Appl. Phys. Lett.* **1991,** *59* (26), 3404-3406.

78. Geim, A. K.; Novoselov, K. S., The rise of graphene. *Nat. Mater.* **2007,** *6* (3), 183-191.

79. Komsa, H.-P.; Kurasch, S.; Lehtinen, O.; Kaiser, U.; Krasheninnikov, A. V., From point to extended defects in two-dimensional MoS_2: evolution of atomic structure under electron irradiation. *Phys. Rev. B* **2013,** *88* (3), 035301.

80. Liu, X.; Xu, T.; Wu, X.; Zhang, Z.; Yu, J.; Qiu, H.; Hong, J.-H.; Jin, C.-H.; Li, J.-X.; Wang, X.-R., Top–down fabrication of sub-nanometre semiconducting nanoribbons derived from molybdenum disulfide sheets. *Nat. Commun.* **2013,** *4*, 1776.

81. Zan, R.; Ramasse, Q. M.; Jalil, R.; Georgiou, T.; Bangert, U.; Novoselov, K. S., Control of radiation damage in MoS_2 by graphene encapsulation. *ACS Nano* **2013,** *7* (11), 10167-10174.

82. Billinge, S. J.; Levin, I., The problem with determining atomic structure at the nanoscale. *Science* **2007,** *316* (5824), 561-565.

83. Urban, K. W., Studying atomic structures by aberration-corrected transmission electron microscopy. *Science* **2008,** *321* (5888), 506-510.

84. Smith, D. J., The realization of atomic resolution with the electron microscope. *Rep. Prog. Phys.* **1997,** *60* (12), 1513.

85. Haider, M.; Uhlemann, S.; Schwan, E.; Rose, H.; Kabius, B.; Urban, K., Electron microscopy image enhanced. *Nature* **1998,** *392*, 768-769.

86. Dellby, N.; Krivanek, L.; Nellist, D.; Batson, E.; Lupini, R., Progress in aberration-corrected scanning transmission electron microscopy. *J. Electron Microsc.* **2001,** *50* (3), 177-185.

87. Varela, M.; Lupini, A. R.; Benthem, K. v.; Borisevich, A. Y.; Chisholm, M. F.; Shibata, N.; Abe, E.; Pennycook, S. J., Materials characterization in the aberration-corrected scanning transmission electron microscope. *Annu. Rev. Mater. Res.* **2005,** *35*, 539-569.

88. Lentzen, M., Progress in aberration-corrected high-resolution transmission electron microscopy using hardware aberration correction. *Microsc. Microanal.* **2006,** *12* (3), 191-205.

89. Smith, D. J., Development of aberration-corrected electron microscopy. *Microsc. Microanal.* **2008,** *14* (1), 2-15.

90. Uhlemann, S.; Haider, M., Residual wave aberrations in the first spherical aberration corrected transmission electron microscope. *Ultramicroscopy* **1998,** *72* (3), 109-119.

91. Krivanek, O.; Dellby, N.; Lupini, A., Towards sub-Å electron beams. *Ultramicroscopy* **1999,** *78* (1), 1-11.

92. Rose, H., Outline of a spherically corrected semiplanatic medium voltage transmission electron microscope. *Optik* **1990,** *85*, 19-24.

93. Haider, M.; Müller, H.; Uhlemann, S.; Zach, J.; Loebau, U.; Hoeschen, R., Prerequisites for a C c/C s-corrected ultrahigh-resolution TEM. *Ultramicroscopy* **2008,** *108* (3), 167-178.

94. Warner, J. H.; Margine, E. R.; Mukai, M.; Robertson, A. W.; Giustino, F.; Kirkland, A. I., Dislocation-driven deformations in graphene. *Science* **2012,** *337* (6091), 209-212.

95. Suenaga, K.; Koshino, M., Atom-by-atom spectroscopy at graphene edge. *Nature* **2010,** *468* (7327), 1088-1090.

96. Otten, M. T.; Coene, W. M., High-resolution imaging on a field emission TEM. *Ultramicroscopy* **1993,** *48* (1-2), 77-91.

97. Buseck, P.; Cowley, J.; Eyring, L., *High-Resolution Transmission Electron Microscopy: And Associated Techniques*. Oxford University Press: 1989.

98. Keast, V.; Scott, A.; Brydson, R.; Williams, D.; Bruley, J., Electron energy-loss near-edge structure–a tool for the investigation of electronic structure on the nanometre scale. *J. Microsc.* **2001,** *203* (2), 135-175.

99. Wallace, P. R., The band theory of graphite. *Phys. Rev.* **1947,** *71* (9), 622.

100. McClure, J., Diamagnetism of graphite. *Phys. Rev.* **1956,** *104* (3), 666.

101. Slonczewski, J.; Weiss, P., Band structure of graphite. *Phys. Rev.* **1958,** *109* (2), 272.

102. Partoens, B.; Peeters, F., From graphene to graphite: Electronic structure around the K point. *Phys. Rev. B* **2006,** *74* (7), 075404.

103. Smith, B. W.; Luzzi, D. E., Electron irradiation effects in single wall carbon nanotubes. *J. Appl. Phys.* **2001,** *90* (7), 3509-3515.

104. Kotakoski, J.; Jin, C.; Lehtinen, O.; Suenaga, K.; Krasheninnikov, A., Electron knock-on damage in hexagonal boron nitride monolayers. *Phys. Rev. B* **2010,** *82* (11), 113404.

105. Komsa, H.-P.; Kotakoski, J.; Kurasch, S.; Lehtinen, O.; Kaiser, U.; Krasheninnikov, A. V., Two-dimensional transition metal dichalcogenides under electron irradiation: defect production and doping. *Phys. Rev. Lett.* **2012,** *109* (3), 035503.

106. Park, H. J.; Ryu, G. H.; Lee, Z., Hole defects on two-dimensional materials formed by electron beam irradiation: toward nanopore devices. *Appl. Microsc.* **2015,** *45* (3), 107-114.

107. Gross, L.; Mohn, F.; Liljeroth, P.; Repp, J.; Giessibl, F. J.; Meyer, G., Measuring the charge state of an adatom with noncontact atomic force microscopy. *Science* **2009,** *324* (5933), 1428-1431.

108. Repp, J.; Meyer, G.; Paavilainen, S.; Olsson, F. E.; Persson, M., Imaging bond formation between a gold atom and pentacene on an insulating surface. *Science* **2006,** *312* (5777), 1196-1199.

109. Gross, L.; Mohn, F.; Moll, N.; Liljeroth, P.; Meyer, G., The chemical structure of a molecule resolved by atomic force microscopy. *Science* **2009,** *325* (5944), 1110-1114.

110. Muller, D.; Kourkoutis, L. F.; Murfitt, M.; Song, J.; Hwang, H.; Silcox, J.; Dellby, N.; Krivanek, O., Atomic-scale chemical imaging of composition and bonding by aberration-corrected microscopy. *Science* **2008,** *319* (5866), 1073-1076.

111. Novoselov, K. S.; Geim, A. K.; Morozov, S. V.; Jiang, D.; Zhang, Y.; Dubonos, S. V.; Grigorieva, I. V.; Firsov, A. A., Electric field effect in atomically thin carbon films. *Science* **2004,** *306* (5696), 666-669.

112. Zhang, Y.; Tan, Y.-W.; Stormer, H. L.; Kim, P., Experimental observation of the quantum Hall effect and Berry's phase in graphene. *Nature* **2005,** *438* (7065), 201-204.

113. Stone, A. J.; Wales, D. J., Theoretical studies of icosahedral C 60 and some related species. *Chem. Phys. Lett.* **1986,** *128* (5), 501-503.

114. Meyer, J. C.; Kisielowski, C.; Erni, R.; Rossell, M. D.; Crommie, M.; Zettl, A., Direct imaging of lattice atoms and topological defects in graphene membranes. *Nano Lett.* **2008,** *8* (11), 3582-3586.

115. Gass, M. H.; Bangert, U.; Bleloch, A. L.; Wang, P.; Nair, R. R.; Geim, A., Free-standing graphene at atomic resolution. *Nat. Nanotechnol.* **2008,** *3* (11), 676-681.

116. Ugeda, M. M.; Brihuega, I.; Guinea, F.; Gómez-Rodríguez, J. M., Missing atom as a source of carbon magnetism. *Phys. Rev. Lett.* **2010,** *104* (9), 096804.

117. Alem, N.; Yazyev, O. V.; Kisielowski, C.; Denes, P.; Dahmen, U.; Hartel, P.; Haider, M.; Bischoff, M.; Jiang, B.; Louie, S. G., Probing the out-of-plane distortion of single point defects in atomically thin hexagonal boron nitride at the picometer scale. *Phys. Rev. Lett.* **2011,** *106* (12), 126102.

118. Gibb, A. L.; Alem, N.; Chen, J.-H.; Erickson, K. J.; Ciston, J.; Gautam, A.; Linck, M.; Zettl, A., Atomic resolution imaging of grain boundary defects in monolayer chemical vapor deposition-grown hexagonal boron nitride. *J. Am. Chem. Soc.* **2013,** *135* (18), 6758-6761.

119. Najmaei, S.; Liu, Z.; Zhou, W.; Zou, X.; Shi, G.; Lei, S.; Yakobson, B. I.; Idrobo, J.-C.; Ajayan, P. M.; Lou, J., Vapour phase growth and grain boundary structure of molybdenum disulphide atomic layers. *Nat. Mater.* **2013,** *12* (8), 754-759.

120. Zhou, W.; Zou, X.; Najmaei, S.; Liu, Z.; Shi, Y.; Kong, J.; Lou, J.; Ajayan, P. M.; Yakobson, B. I.; Idrobo, J.-C., Intrinsic structural defects in monolayer molybdenum disulfide. *Nano Lett.* **2013,** *13* (6), 2615-2622.

121. Lin, Y.-C.; Dumcenco, D. O.; Huang, Y.-S.; Suenaga, K., Atomic mechanism of the semiconducting-to-metallic phase transition in single-layered MoS_2. *Nat. Nanotechnol.* **2014,** *9* (5), 391-396.

122. Dreyer, D. R.; Park, S.; Bielawski, C. W.; Ruoff, R. S., The chemistry of graphene oxide. *Chem. Soc. Rev.* **2010,** *39* (1), 228-240.

123. Stankovich, S.; Dikin, D. A.; Piner, R. D.; Kohlhaas, K. A.; Kleinhammes, A.; Jia, Y.; Wu, Y.; Nguyen, S. T.; Ruoff, R. S., Synthesis of graphene-based nanosheets via chemical reduction of exfoliated graphite oxide. *Carbon* **2007,** *45* (7), 1558-1565.

124. McAllister, M. J.; Li, J.-L.; Adamson, D. H.; Schniepp, H. C.; Abdala, A. A.; Liu, J.; Herrera-Alonso, M.; Milius, D. L.; Car, R.; Prud'homme, R. K., Single sheet functionalized graphene by oxidation and thermal expansion of graphite. *Chem. Mater.* **2007,** *19* (18), 4396-4404.

125. Dikin, D. A.; Stankovich, S.; Zimney, E. J.; Piner, R. D.; Dommett, G. H.; Evmenenko, G.; Nguyen, S. T.; Ruoff, R. S., Preparation and characterization of graphene oxide paper. *Nature* **2007,** *448* (7152), 457-460.

126. Marcano, D. C.; Kosynkin, D. V.; Berlin, J. M.; Sinitskii, A.; Sun, Z.; Slesarev, A.; Alemany, L. B.; Lu, W.; Tour, J. M., Improved synthesis of graphene oxide. *ACS Nano* **2010,** 4(8), 4806-4814.

127. Ryu, G. H.; Lee, J.; Kang, D.; Jo, H.; Shin, H.; Lee, Z., Effects of dry oxidation treatments on monolayer graphene. *2D Mater.* **2017,** 4(2) 021011.

128. Bagri, A.; Grantab, R.; Medhekar, N.; Shenoy, V., Stability and formation mechanisms of carbonyl-and hydroxyl-decorated holes in graphene oxide. *J. Phys. Chem. C* **2010,** *114* (28), 12053-12061.

129. Jin, C.; Lin, F.; Suenaga, K.; Iijima, S., Fabrication of a freestanding boron nitride single layer and its defect assignments. *Phys. Rev. Lett.* **2009,** *102* (19), 195505.

130. Meyer, J. C.; Chuvilin, A.; Algara-Siller, G.; Biskupek, J.; Kaiser, U., Selective sputtering and atomic resolution imaging of atomically thin boron nitride membranes. *Nano Lett.* **2009,** *9* (7), 2683-2689.

131. Derycke, V.; Soukiassian, P.; Mayne, A.; Dujardin, G.; Gautier, J., Carbon atomic chain formation on the β-SiC (100) surface by controlled sp→ sp 3 transformation. *Phys. Rev. Lett.* **1998,** *81* (26), 5868.

132. Heath, J.; Zhang, Q.; O'Brien, S.; Curl, R.; Kroto, H.; Smalley, R., The formation of long carbon chain molecules during laser vaporization of graphite. *J. Am. Chem. Soc.* **1987,** *109* (2), 359-363.

133. Lagow, R. J.; Kampa, J. J.; Wei, H.-C.; Battle, S. L.; Genge, J. W.; Laude, D. A.; Harper, C. J.; Bau, R.; Stevens, R. C.; Haw, J. F., Synthesis of linear acetylenic carbon: the" sp" carbon allotrope. *Science* **1995,** *267* (5196), 362-368.

134. Troiani, H.; Miki-Yoshida, M.; Camacho-Bragado, G.; Marques, M.; Rubio, A.; Ascencio, J.; Jose-Yacaman, M., Direct observation of the mechanical properties of single-walled carbon nanotubes and their junctions at the atomic level. *Nano Lett.* **2003,** *3* (6), 751-755.

135. Yuzvinsky, T.; Mickelson, W.; Aloni, S.; Begtrup, G.; Kis, A.; Zettl, A., Shrinking a carbon nanotube. *Nano Lett.* **2006,** *6* (12), 2718-2722.

136. Zhao, X.; Ando, Y.; Liu, Y.; Jinno, M.; Suzuki, T., Carbon nanowire made of a long linear carbon chain inserted inside a multiwalled carbon nanotube. *Phys. Rev. Lett.* **2003,** *90* (18), 187401.

137. Cretu, O.; Komsa, H.-P.; Lehtinen, O.; Algara-Siller, G.; Kaiser, U.; Suenaga, K.; Krasheninnikov, A. V., Experimental observation of boron nitride chains. *ACS Nano* **2014,** *8* (12), 11950-11957.

138. Ryu, G. H.; Park, H. J.; Ryou, J.; Park, J.; Lee, J.; Kim, G.; Shin, H. S.; Bielawski, C. W.; Ruoff, R. S.; Hong, S., Atomic-scale dynamics of triangular hole growth in monolayer hexagonal boron nitride under electron irradiation. *Nanoscale* **2015,** *7* (24), 10600-10605.

139. Meyer, J. C.; Eder, F.; Kurasch, S.; Skakalova, V.; Kotakoski, J.; Park, H. J.; Roth, S.; Chuvilin, A.; Eyhusen, S.; Benner, G., Accurate measurement of electron beam induced displacement cross sections for single-layer graphene. *Phys. Rev. Lett.* **2012,** *108* (19), 196102.

140. Regan, W.; Alem, N.; Alemán, B.; Geng, B.; Girit, Ç.; Maserati, L.; Wang, F.; Crommie, M.; Zettl, A., A direct transfer of layer-area graphene. *Appl. Phys. Lett.* **2010,** *96* (11), 113102.

141. Kim, G.; Jang, A. R.; Jeong, H. Y.; Lee, Z.; Kang, D. J.; Shin, H. S., Growth of High-Crystalline, Single-Layer Hexagonal Boron Nitride on Recyclable Platinum Foil. *Nano Lett.* **2013,** *13* (4), 1834-1839.

142. Zobelli, A.; Gloter, A.; Ewels, C.; Seifert, G.; Colliex, C., Electron knock-on cross section of carbon and boron nitride nanotubes. *Phys. Rev. B* **2007,** *75* (24), 245402.

143. Kresse, G.; Furthmüller, J., Efficiency of ab-initio total energy calculations for metals and semiconductors using a plane-wave basis set. *Comput. Mater. Sci.* **1996,** *6* (1), 15-50.

144. Kresse, G.; Furthmüller, J., Efficient iterative schemes for ab initio total-energy calculations using a plane-wave basis set. *Phys. Rev. B* **1996,** *54* (16), 11169.

145. Blöchl, P. E., Projector augmented-wave method. *Phys. Rev. B* **1994,** *50* (24), 17953.

146. Kresse, G.; Joubert, D., From ultrasoft pseudopotentials to the projector augmented-wave method. *Phys. Rev. B* **1999,** *59* (3), 1758.

147. Grimme, S., Semiempirical GGA-type density functional constructed with a long-range dispersion correction. *J. Comput. Chem.* **2006,** *27* (15), 1787-1799.

148. Kohn, W.; Sham, L. J., Self-consistent equations including exchange and correlation effects. *Phys. Rev.* **1965,** *140* (4A), A1133.

149. Perdew, J. P.; Burke, K.; Ernzerhof, M., Generalized gradient approximation made simple. *Phys. Rev. Lett.* **1996,** *77* (18), 3865.

150. Plimpton, S., Fast parallel algorithms for short-range molecular dynamics. *J. Comput. Phys.* **1995,** *117* (1), 1-19.

151. van Duin, A. C.; Damsté, J. S. S., Computational chemical investigation into isorenieratene cyclisation. *Org. Geochem.* **2003,** *34* (4), 515-526.

152. Van Duin, A. C.; Dasgupta, S.; Lorant, F.; Goddard, W. A., ReaxFF: a reactive force field for hydrocarbons. *J. Phys. Chem. A* **2001,** *105* (41), 9396-9409.

153. Lee, Y.; Lee, J.; Bark, H.; Oh, I. K.; Ryu, G. H.; Lee, Z.; Kim, H.; Cho, J. H.; Ahn, J. H.; Lee, C., Synthesis of wafer-scale uniform molybdenum disulfide films with control over the layer number using a gas phase sulfur precursor. *Nanoscale* **2014,** *6* (5), 2821-2826.

154. Parks, P.; Turnbull, R. J., Effect of transonic flow in the ablation cloud on the lifetime of a solid hydrogen pellet in a plasma. *Phys. Fluids* **1978,** *21* (10), 1735-1741.

155. Mehmood, F.; Pachter, R.; Lu, W.; Boeckl, J. J., Adsorption and diffusion of oxygen on single-layer graphene with topological defects. *J. Phys. Chem. C* **2013,** *117* (20), 10366-10374.

156. Zhou, J.; Wang, J.; Sun, C.; Maley, J.; Sammynaiken, R.; Sham, T.; Pong, W., Nano-scale chemical imaging of a single sheet of reduced graphene oxide. *J. Mater. Chem.* **2011,** *21* (38), 14622-14630.

157. Ganguly, A.; Sharma, S.; Papakonstantinou, P.; Hamilton, J., Probing the thermal deoxygenation of graphene oxide using high-resolution in situ X-ray-based spectroscopies. *J. Phys. Chem.C* **2011,** *115* (34), 17009-17019.

158. Lee, V.; Dennis, R. V.; Schultz, B. J.; Jaye, C.; Fischer, D. A.; Banerjee, S., Soft x-ray absorption spectroscopy studies of the electronic structure recovery of graphene oxide upon chemical defunctionalization. *J. Phys. Chem.C* **2012,** *116* (38), 20591-20599.

159. Chuang, C.-H.; Wang, Y.-F.; Shao, Y.-C.; Yeh, Y.-C.; Wang, D.-Y.; Chen, C.-W.; Chiou, J.; Ray, S. C.; Pong, W.; Zhang, L., The effect of thermal reduction on the photoluminescence and electronic structures of graphene oxides. *Sci. Rep.* **2014,** *4*, 4525.

160. Lee, D.; Seo, J.; Zhu, X.; Lee, J.; Shin, H.-J.; Cole, J. M.; Shin, T.; Lee, J.; Lee, H.; Su, H., Quantum confinement-induced tunable exciton states in graphene oxide. *Sci. Rep.* **2013,** *3*.

161. Becerril, H. A.; Mao, J.; Liu, Z.; Stoltenberg, R. M.; Bao, Z.; Chen, Y., Evaluation of solution-processed reduced graphene oxide films as transparent conductors. *ACS Nano* **2008,** *2* (3), 463-470.

162. Jeong, H.-K.; Lee, Y. P.; Lahaye, R. J.; Park, M.-H.; An, K. H.; Kim, I. J.; Yang, C.-W.; Park, C. Y.; Ruoff, R. S.; Lee, Y. H., Evidence of graphitic AB stacking order of graphite oxides. *J. Am. Chem. Soc.* **2008,** *130* (4), 1362-1366.

163. Francis, J.; Hitchcock, A., Inner-shell spectroscopy of p-benzoquinone, hydroquinone, and phenol: distinguishing quinoid and benzenoid structures. *J. Phys. Chem.* **1992,** *96* (16), 6598-6610.

164. Näslund, L.-Å.; Lüning, J.; Ufuktepe, Y.; Ogasawara, H.; Wernet, P.; Bergmann, U.; Pettersson, L.; Nilsson, A., X-ray absorption spectroscopy measurements of liquid water. *J. Phys. Chem.B* **2005,** *109* (28), 13835-13839.

165. Ghaderi, N.; Peressi, M., First-principle study of hydroxyl functional groups on pristine, defected graphene, and graphene epoxide. *J. Phys. Chem. C* **2010,** *114* (49), 21625-21630.

166. Yan, H.; Xu, B.; Shi, S.; Ouyang, C., First-principles study of the oxygen adsorption and dissociation on graphene and nitrogen doped graphene for Li-air batteries. *J. Appl. Phys.* **2012,** *112* (10), 104316.

167. Ersan, F.; Aktürk, E.; Ciraci, S., Interaction of Adatoms and Molecules with Single-Layer Arsenene Phases. *J. Phys. Chem. C* **2016,** *120* (26), 14345-14355.

168. Hughes, Z. E.; Walsh, T. R., Computational chemistry for graphene-based energy applications: progress and challenges. *Nanoscale* **2015,** *7* (16), 6883-6908.

169. Zhou, W.; Prange, M.; Oxley, M.; Pantelides, S.; Pennycook, S.; Nanda, J.; Narula, C.; Idrobo, J., Atomic Scale Study of Point Defects in Graphene using STEM. *Microsc. Microanal.* **2011,** *17* (S2), 1498-1499.

170. Ramasse, Q. M.; Zan, R.; Bangert, U.; Boukhvalov, D. W.; Son, Y.-W.; Novoselov, K. S., Direct Experimental Evidence of Metal-Mediated Etching of Suspended Graphene. *ACS Nano* **2012,** *6* (5), 4063-4071.

171. Zobelli, A.; Ewels, C. P.; Gloter, A.; Seifert, G.; Stephan, O.; Csillag, S.; Colliex, C., Defective Structure of BN Nanotubes: From Single Vacancies to Dislocation Lines. *Nano Lett.* **2006,** *6* (9), 1955-1960.

172. Komsa, H. P.; Kotakoski, J.; Kurasch, S.; Lehtinen, O.; Kaiser, U.; Krasheninnikov, A. V., Two-Dimensional Transition Metal Dichalcogenides under Electron Irradiation: Defect Production and Doping. *Phys. Rev. Lett.* **2012,** *109* (3), 035503.

173. Komsa, H. P.; Kurasch, S.; Lehtinen, O.; Kaiser, U.; Krasheninnikov, A. V., From point to extended defects in two-dimensional MoS2: Evolution of atomic structure under electron irradiation. *Phys. Rev. B* **2013,** *88* (3), 035301.

174. Zhou, J.; Xu, N. S.; Deng, S. Z.; Chen, J.; She, J. C.; Wang, Z. L., Large-area nanowire arrays of molybdenum and molybdenum oxides: synthesis and field emission properties. *Adv. Mater.* **2003,** *15* (21), 1835-1840.

175. Willians, D. B.; Carter, C. B.; Transmisstion Electron Microscopy. Springer. Second Edition**.**

CURRICULUM VITAE

GYEONGHEE RYU

Email: ryukhee@gmail.com

Birthday: September 5th, 1989

Mobile: +82-10-7683-3279

Address: Bidg.102-511, 50 UNIST-gil, Ulsan 44919, Republic of Korea

EDUCATION

2012 ~ 2018 **Combined M.S. & Ph.D. Course in Materials Science and Engineering**

(Expected award date of Ph.D.: February 2018)

UNIST (Ulsan National Institute of Science and Technology), Ulsan, Republic of Korea

Advisor: Prof. Zonghoon Lee (zhlee@unist.ac.kr, http://ASEMlab.org/)

(Dissertation title: Investigation of Atomic-Scale Defects in Two-Dimensional Materials)

2008 ~ 2012 **B.S. in Metallurgical and Materials Engineering, February 2012**

Gyeongsang National University, Jinju, Republic of Korea

RESEARCH EXPEREIENCES

2012 ~ 2014 **Graduate Research Assistant**

Materials Science Department, UNIST, Ulsan, Republic of Korea

PUBLICATIONS

1. **G.H. Ryu**, J. Lee, D. Kang, H.J. Jo, H.S. Shin and Z. Lee*, "Effects of dry oxidation treatments on monolayer graphene", *2D Materials*, 4(2), 024011, 2017.
2. T.Y. Ko, A. Jeong, W. Kim, J.H. Lee, Y. Kim, J.E. Lee, **G.H. Ryu**, K. Park, D.

Kim, Z. Lee, M.H. Lee, C. Lee and S. Ryu*, "On-stack two-dimensional conversion of MoS_2 into MoO_3", *2D Materials*, 4(1), 014003, 2017.

3. K. Gupta, T. Liu, R. Kavian, H.G. Chae, **G.H. Ryu**, Z. Lee, S.W. Lee and S. Kumara*, "High surface area carbon from polyacrylonitrile for high performance electrochemical capacitive energy storage", *Journal of Materials Chemistry A*, 4, 18294-18299, 2016.

4. J.G. Song, S.J. Kim, W.J. Woo, Y. Kim, I.K. Oh, **G.H. Ryu**, Z. Lee, J.H. Lim, J. Park* and H. Kim*, "Effect of Al_2O_3 deposition on performance of top-gated monolayer MoS_2 based field effect transistor", *ACS Applied Materials & Interfaces*, 8 (41), 28130–28135, 2016.

5. Y. Kim, H. Bark, **G.H. Ryu**, Z. Lee and C. Lee*, "Wafer scale monolayer MoS_2 grown by chemical vapor deposition using a reaction of MoO_3 and H_2S", *Journal of Physics: Condensed Matter*, 28, 184002 (6pp), 2016.

6. J.W. Lee, K. Kim, S. Han, **G.H. Ryu**, Z. Lee and H. Cheong*, "Raman signatures of polytypism in molybdenum disulfide", *ACS Nano*, 10 (2), pp 1948-1953, 2016.

7. J.G. Song, **G.H. Ryu**, S.H. Hwang, S. Sim, C.W. Lee, T. Choi, H. Jung, Y. Kim, Z. Lee, J.M. Myoung, C. Dussarrat, C. Lansalot-Matras, J. Park, H. Choi and H. Kim*, "Controllable synthesis of molybdenum tungsten disulfide alloy for vertically composition-controlled multilayer", *Nature Communications*, 6, 7817, 2015.

8. K. Park, Y. Kim, J.G. Song, S.J. Kim, C.W. Lee, **G.H. Ryu**, Z. Lee, J. Park and H. Kim*, "Uniform, large-area self-limiting layer synthesis of tungsten diselenide", *2D Materials*, 3(1), 014004, 2016.

9. **G.H. Ryu**, J. Lee, N.Y. Kim, Y.D. Lee, Y. Kim, M.J. Kim, C. Lee and Z. Lee*, "Line-defect mediated formation of hole and Mo clusters in monolayer molybdenum disulfide", *2D Materials*, 3(1), 014002, 2016.

10. R.Y. Tay, H.J. Park, **G.H. Ryu**, D. Tan, S.H. Tsang, H. Li, W. Liu, E.H.T. Teo*, Z. Lee, Y. Lifshitz and R.S. Ruoff, "Synthesis of aligned symmetrical multifaceted monolayer hexagonal boron nitride single crystals on resolidified copper", *Nanoscale*, 8, 2434–2444, 2016.

11. Y. Kim, J.G. Song, Y.J. Park, **G.H. Ryu**, S.H. Hwang, P.J. Jeon, C.W. Lee, W.J. Woo, T. Choi, H. Jung, J.M. Myoung, S. Im, Z. Lee, J.H. Ahn, J. Park and H. Kim, "Self-limiting layer synthesis of transition metal dichalcogenides", *Scientific Reports*, 2015, 2045-2322.

12. G. Kim, H. Lim, K.Y. Ma, A.R. Jang, **G.H. Ryu**, M. Jung, H.J. Shin, Z. Lee and H.S. Shin*, "Catalytic conversion of hexagonal boron nitride to graphene for in-

plane heterostructures", *Nano Letters*, 15 (7), pp 4769-4775, 2015.

13. **G.H. Ryu**, H.J. Park, J. Ryou, J. Park, J. Lee, G. Kim, H.S. Shin, C.W. Bielawski, R.S. Ruoff, S. Hong and Z. Lee*, "Atomic-scale dynamics of triangular hole growth in monolayer hexagonal boron nitride under electron irradiation", *Nanoscale*, 7, 10600-10605, 2015.
- Feature on a front cover of 2015

14. Y. Choi, **G.H. Ryu**, S.H. Min, B.R. Lee, M.H. Song, Z. Lee and B.S. Kim*, "Interface controlled synthesis of heterodimeric silver-carbon nanoparticles derived from polysaccharides", *ACS Nano*, 8 (11), pp 11377-11385, 2014.

15. Y.N. Jo, M.S. Park, E.Y. Lee, J. Lee, J.G. Kim, K.J. Hong, S.I. Lee, H.Y. Jeong, **G.H. Ryu**, Z. Lee and Y.J. Kim*, "Increasing reversible capacity of soft carbon anode by phosphoric acid treatment", *Electrochimica Acta*, 146 (10), 630-637, 2014.

16. J. Lee, J. Baek, **G.H. Ryu**, M.J. Lee, S. Oh, S.K. Hong, B.H. Kim, S.H. Lee, B.J. Cho, Z. Lee* and S. Jeon*, "High-angle tilt boundary graphene domain recrystallized from mobile hot-wire-assisted chemical vapor deposition system", *Nano Letters*, 14 (8), pp 4352-4359, 2014.

17. Y. Lee, J. Lee, H. Bark, I.K. Oh, **G.H. Ryu**, Z. Lee, H. Kim, J.H. Cho, J.H. Ahn and C. Lee*, "Synthesis of wafer-scale uniform molybdenum disulfide films with control over the layer number using a gas phase sulfur precursor", *Nanoscale*, 6, 2821-2826, 2014.

18. J.H. Chu, J. Kwak, S.D. Kim, M.J. Lee, J.J. Kim, S.D. Park, J.K. Choi, **G.H. Ryu**, K. Park, S.Y. Kim, J.H. Kim, Z. Lee, Y.W. Kim and S.Y. Kwon*, "Monolithic graphene oxide sheets with controllable composition", *Nature Communications*, 5, 3383, 2014.

19. J. Ryu, Y. Kim, D. Won, N. Kim, J.S. Park, E.K. Lee, D. Cho, S.P. Cho, S.J. Kim, **G.H. Ryu**, H.A.S. Shin, Z. Lee, B.H. Hong and S. Cho*, "Fast synthesis of high-performance graphene films by hydrogen-free rapid thermal chemical vapor deposition", *ACS Nano*, 8 (1), pp 950-956, 2014.

20. **G.H. Ryu**, H.J. Park, N.Y. Kim and Z. Lee*, "Atomic resolution imaging of rotated bilayer graphene sheets using a low kV aberration-corrected TEM", *Applied Microscopy*, 42 (4), pp 218-22, 2012.
- Selected as the journal cover of December 2012
- Selected as the best paper published in 2012 in the Korean Society of Microscopy Journals

MANUSCRIPS IN PREPARATION (OR SUBMISSION)

1. Oxygen and hydrogen atom-driven formation of point defects in monolayer graphene
2. Free-standing 2D silicon dioxide sheet

PATENTS

Korea Patent

1. Z. Lee, K. Kim, H.K. Hong, **G.H Ryu**, Method for producing samples for transmission electron microscopy using tripod polishing and focused ion beam, Korea Patent, No.1020130096890, August 14, 2013 (PCT).
2. Z. Lee, **G.H Ryu**, Jig for transmission electron microscopy for loading samples on in-situ tip, Korea Patent, No.1020130136073, November 11, 2013 (PCT).

RESEARCH INTEREST

- Atomic-scale study using advanced Transmission Electron Microscopy (TEM)
- Defect control of 2D crystals on aberration corrected TEM
- Investigation of defect formation mechanism in 2D Crystals
- Carbon based nanostructure materials: structure-property relationships (oxidized graphene)

TECHNICAL EXPERIENCE

Synthesis of nanostructures

- Synthesis of high-quality single-layer & multi-layer graphene by chemical vapor deposition method

Atomic-resolution transmission electron microscopy

1. Atomic imaging of 2D materials using aberration corrected TEM (Double corrected FEI Titan Cubed 60-300 with a monochromator, JEOL 2100F with probe corrector)
2. Spectroscopic analysis of soft matters using Electron Energy Loss Spectroscopy (EELS)

Modification of materials using chemical and physical methods

1. Oxygen plasma treatments on 2D materials (physical and chemical methods)
2. UV/Ozone treatments on 2D materials (chemical method)

Other analytical equipment

1. Focused Ion Beam (FIB): TEM sample prep, site-specific analysis, deposition, ablation of materials

2. Scanning Electron Microscopy (SEM): analyzing surface of solid materials

CONFERENCE PRESENTATIONS

Conference Proceedings/Extended Abstracts

1. **G.H. Ryu**, H.J. Park and Z. Lee*. "Dynamics of triangular hole growth in monolayer hexagonal boron nitride under electron irradiation", Microscopy & Microanalysis 2015, Oregon, USA, pp.372, August 3-6, 2015.

Presentations

1. **G.H.Ryu**, S.Lee, G.Lee and Z.Lee*, "OH molecule involved formation of point defects in monolayer graphene sheet", The 3rd East-Asia Microscopy Conference, Busan Bexco, Korea, November 7-10, 2017 (oral presentation).

2. **G.H.Ryu** and Z.Lee*, "Investigation of atomic-scale defects in 2-dimensional materials", The 3rd East-Asia Microscopy Conference, Busan Bexco, Korea, November 7-10, 2017 (poster)

3. **G.H. Ryu**, G. Lee and Z. Lee*, "Effects of dry oxidation treatments on monolayer graphene", 48th Korean Society of Microscopy Annual Conference, Yeosu MVL Hotel, Korea, April 20-21, 2017 (poster).

4. **G.H. Ryu**, J. Lee, N.Y. Kim, Y. Lee and Z. Lee*, "Line-defect mediated of hole and Mo clusters in monolayer MoS_2 sheet", 8th International Conference on Recent Progress, Sungkyunkwan University, Korea, September 25-29, 2016 (poster).

5. **G.H. Ryu**, J. Lee, N.Y. Kim, Y. Lee and Z. Lee*, "Line-defect mediated formation of hole and Mo clusters in single layer molybdenum disulfide", 47th Korean Society of Microscopy Spring Conference, Gumico, Korea, June 2-3, 2016 (poster).

6. **G.H. Ryu**, J. Lee, N.Y. Kim, Y. Lee and Z. Lee*, "Line-defect mediated formation of hole and Mo clusters in monolayer molybdenum disulfide", the 3rd Korean Graphene Symposium, Buyeo, Korea, April 14-15, 2016 (poster).

7. **G.H. Ryu**, H.J. Park, and Z. Lee*. "Dynamics of triangular hole growth in monolayer hexagonal boron nitride under electron irradiation", Microscopy & Microanalysis 2015, Oregon, USA, pp.372, August 3-6, 2015 (oral presentation).

8. H.J. Park, **G.H. Ryu**, J. Lee, J. Ryou, J. Park, S. Hong and Z. Lee*, "Triangular defect growth mechanism of single layer h-BN using atomic resolution transmission electron microscopy", 46th Korean Society of Microscopy Spring Conference, Seoul National University, Korea, May 28-29, 2015 (oral presentation).

9. **G.H. Ryu**, H.J. Park, J. Lee, J. Ryou, J. Park, S. Hong and Z. Lee*, "Mechanism of triangular hole growth in monolayer hexagonal boron nitride through electron beam

irradiation", the 2nd Korean Graphene Symposium, Buyeo, Korea, March 26-27, 2015 (poster).

10. J. Song, Y. Kim, **G.H. Ryu**, Z. Lee, C. L, S. Hwang, J. Myoung, C.W. Lee, J. Park and H. Kim*, "Composition and layer modulated synthesis of molybdenum tungsten disulfide alloy nanosheets using super-cycle atomic layer deposition", the 2nd Korean Graphene Symposium, Buyeo, Korea, March 26-27, 2015 (poster).

11. Y. Kim, J. Song, **G.H. Ryu**, S. Hwang, C.W. Lee, T. Choi, W. Woo, H. Jung, K.Y. Ko, Z. Lee, J. Myoung, Y.J. Park, J. Ahn, J. Park and H. Kim*, "Synthesis of wafer-scale layer controlled molybdenum disulfide using atomic layer deposition", the 2nd Korean Graphene Symposium, Buyeo, Korea, March 26-27, 2015 (poster).

12. T.Y. Ko, A. Jeong, J. Lee, Y. Kim, J.E. Lee, **G.H. Ryu**, C. Lee, M.H. Lee, Z. Lee and S. Ryu*, "Plasma oxidation of single and few-layer MoS_2", the 2nd Korean Graphene Symposium, Buyeo, Korea, March 26-27, 2015 (poster).

13. **G.H. Ryu**, H.J. Park, N.Y. Kim, M.J. Lee and Z. Lee*, "Graphene research at atomic scale using aberration-corrected TEM", 2014 Collaborative Conference on Materials Research.

14. **G.H. Ryu**, J.H. Kim, S. Son, H.J. Park, K. Kim, M.J. Lee, N.Y. Kim, H. Hong and Z. Lee*, "Investigation of stacking structure and grain boundary of bilayer 2D materials using aberration-corrected TEM", 45th Korean Society of Microscopy Spring Conference, Chonbuk National University, Korea, May 22-23, 2014 (poster).

15. **G.H. Ryu**, H.J. Park, N.Y. Kim, J.H. Kim, K. Kim, M.J. Lee, S. Son, H. Hong and Z. Lee*, "Investigation of stacking structure and grain boundary of bilayer 2D materials using aberration corrected TEM", the 1st Korean Graphene Symposium, Buyeo, Korea, April 3-4, 2014 (poster).

16. G. Kim, A. Jang, **G.H. Ryu**, Z. Lee and H.S. Shin*, "Growth of lateral of graphene and h-BN on platinum", the 1st Korean Graphene Symposium, Buyeo, Korea, April 3-4, 2014 (poster).

17. **G.H. Ryu**, H.J. Park, N.Y. Kim, J.H. Kim, K. Kim, M.J. Lee and Z. Lee*, "Investigation of stacking structure and defects of bilayer graphene using aberration corrected TEM", The 1st international conference of surface engineering (ICSE2013), Haeundae grand hotel, Korea, November 18-21, 2013 (oral presentation).

ACTIVITIES/AWARDS

1. **Best poster award**, "Effects of dry oxidation treatments on monolayer graphene", 48th Korean Society of Microscopy Annual Conference, Yeosu MVL Hotel, Korea, April 20-21, 2017 (poster).

2. **Best poster award**, "Mechanism of triangular hole growth in monolayer hexagonal boron nitride through electron beam irradiation", the 2nd Korean Graphene Symposium, Buyeo, Korea, March 26-27, 2015 (poster).

3. **Best poster award**, "Investigation of stacking structure and grain boundary of bilayer 2D materials using aberration-corrected TEM", 45th Korean Society of Microscopy Spring Conference, Chonbuk National University, Korea, May 22-23, 2014 (poster).

4. **Best paper award**, "Atomic resolution imaging of rotated bilayer graphene sheets using a low kV aberration corrected transmission electron microscope", 44th Korean Society of Microscopy Spring Conference, Yonsei University, Korea, June 13-14, 2013.

COMPLETION OF EDUCATION

Period	Education	Educational institution
2012.12.03-2012.12.07	Gatan Asia EELS & EFTEM Analysis School in Osaka University, Japan	Gatan Inc.
	Training using EELS and EFTEM	
2013.07.16-2013.07.19	20th Transmission Electron Microscope workshop, Korea	Korean Society of Microscopy
	Microscope application and use education	
2014.02.24-2014.02.28	Titan Advanced Materials Sc. Course in Eindhoven, Netherlands	FEI company
	Training using aberration corrected Transmission Electron Microscope	

RESEARCH PROJECT PARTICIPATED

1. Soft carbon anode material development for high capacity rechargeable battery (2011.05.01 - 2014.02.28).

2. Growth and defect control in graphene and development of innovative graphene-based electronic devices, Nano Material Technology Development Program, the Ministry of Science, S. Korea (2012.09.01 - 2017.08.31).

3. Atomic scale electron microscopy study on multidimensional carbon materials and 2D crystals (under Prof. Zonghoon Lee), Student researcher, IBS-R019-D1.
   : Center for Multidimensional Carbon Materials (CMCM, director: Prof. Rodney S. Ruoff), Institute of Basic Science.

4. In situ study of induced defects in binary 2D materials at atomic scale, No. 2015R1A2A2A01006992, (2015.05.01 - 2018.05.31).